The Zwicky Transient Facility Census of the Local Universe. I. Systematic Search for Calcium-rich Gap Transients Reveals Three Related Spectroscopic Subclasses

Kishalay De[1] , Mansi M. Kasliwal[1] , Anastasios Tzanidakis[1] , U. Christoffer Fremling[1] , Scott Adams[1], Robert Aloisi[2] ,
Igor Andreoni[1] , Ashot Bagdasaryan[1], Eric C. Bellm[3] , Lars Bildsten[4,5], Christopher Cannella[1], David O. Cook[6] ,
Alexandre Delacroix[7], Andrew Drake[1], Dmitry Duev[1] , Alison Dugas[1,8] , Sara Frederick[9] , Avishay Gal-Yam[10] ,
Daniel Goldstein[1] , V. Zach Golkhou[3,11,21] , Matthew J. Graham[1] , David Hale[7], Matthew Hankins[1] , George Helou[6] ,
Anna Y. Q. Ho[1] , Ido Irani[12] , Jacob E. Jencson[13] , David L. Kaplan[2] , Stephen Kaye[7], S. R. Kulkarni[1] ,
Thomas Kupfer[5] , Russ R. Laher[6] , Robin Leadbeater[14], Ragnhild Lunnan[15] , Frank J. Masci[6] , Adam A. Miller[16,17] ,
James D. Neill[1] , Eran O. Ofek[10] , Daniel A. Perley[18] , Abigail Polin[19,20] , Thomas A. Prince[1] , Eliot Quataert[19] ,
Dan Reiley[7], Reed L. Riddle[7] , Ben Rusholme[6] , Yashvi Sharma[1] , David L. Shupe[6] , Jesper Sollerman[15] ,
Leonardo Tartaglia[15] , Richard Walters[7], Lin Yan[1] , and Yuhan Yao[1]

[1] Cahill Center for Astrophysics, California Institute of Technology, 1200 E. California Blvd., Pasadena, CA 91125, USA; kde@astro.caltech.edu
[2] Center for Gravitation, Cosmology, and Astrophysics, Department of Physics, University of Wisconsin–Milwaukee, P.O. Box 413, Milwaukee, WI 53201, USA
[3] DIRAC Institute, Department of Astronomy, University of Washington, 3910 15th Ave. NE, Seattle, WA 98195, USA
[4] Department of Physics, University of California, Santa Barbara, CA 93106, USA
[5] Kavli Institute for Theoretical Physics, University of California, Santa Barbara, CA 93106, USA
[6] IPAC, California Institute of Technology, 1200 E. California Blvd., Pasadena, CA 91125, USA
[7] Caltech Optical Observatories, California Institute of Technology, Pasadena, CA 91125, USA
[8] Institute for Astronomy, University of Hawai'i, 2680 Woodlawn Dr., Honolulu, HI 96822, USA
[9] Department of Astronomy, University of Maryland, College Park, MD 20742, USA
[10] Benoziyo Center for Astrophysics, The Weizmann Institute of Science, Rehovot 76100, Israel
[11] The eScience Institute, University of Washington, Seattle, WA 98195, USA
[12] Department of Particle Physics and Astrophysics, Weizmann Institute of Science, Rehovot 7610001, Israel
[13] Steward Observatory, University of Arizona, 933 N. Cherry Ave., Tucson, AZ 85721-0065, USA
[14] Three Hills Observatory, The Birches CA71JF, UK
[15] Department of Astronomy, The Oskar Klein Centre, Stockholm University, AlbaNova, SE-10691 Stockholm, Sweden
[16] Center for Interdisciplinary Exploration and Research in Astrophysics (CIERA) and Department of Physics and Astronomy, Northwestern University, 2145
Sheridan Rd., Evanston, IL 60208, USA
[17] The Adler Planetarium, Chicago, IL 60605, USA
[18] Astrophysics Research Institute, Liverpool John Moores University, IC2, Liverpool Science Park, 146 Brownlow Hill, Liverpool L3 5RF, UK
[19] Department of Astronomy, University of California, Berkeley, CA, 94720-3411, USA
[20] Lawrence Berkeley National Laboratory, Berkeley, CA 94720, USA

Abstract

Using the Zwicky Transient Facility alert stream, we are conducting a large spectroscopic campaign to construct a complete, volume-limited sample of transients brighter than 20 mag, and coincident within $100''$ of galaxies in the Census of the Local Universe catalog. We describe the experiment design and spectroscopic completeness from the first 16 months of operations, which have classified 754 supernovae. We present results from a systematic search for calcium-rich gap transients in the sample of 22 low-luminosity (peak absolute magnitude $M > -17$), hydrogen-poor events found in the experiment. We report the detection of eight new events, and constrain their volumetric rate to $\gtrsim 15\% \pm 5\%$ of the SN Ia rate. Combining this sample with 10 previously known events, we find a likely continuum of spectroscopic properties ranging from events with SN Ia–like features (Ca-Ia objects) to those with SN Ib/c–like features (Ca-Ib/c objects) at peak light. Within the Ca-Ib/c events, we find two populations distinguished by their red ($g - r \approx 1.5$ mag) or green ($g - r \approx 0.5$ mag) colors at the r-band peak, wherein redder events show strong line blanketing features and slower light curves (similar to Ca-Ia objects), weaker He lines, and lower [Ca II]/[O I] in the nebular phase. We find that all together the spectroscopic continuum, volumetric rates, and striking old environments are consistent with the explosive burning of He shells on low-mass white dwarfs. We suggest that Ca-Ia and red Ca-Ib/c objects arise from the double detonation of He shells, while green Ca-Ib/c objects are consistent with low-efficiency burning scenarios like detonations in low-density shells or deflagrations.

Unified Astronomy Thesaurus concepts: Supernovae (1668); Compact objects (288); White dwarf stars (1799)

Supporting material: data behind figures, machine-readable tables

1. Introduction

Calcium-rich gap transients represent an emerging population of faint and fast-evolving supernovae (SNe) identified by their conspicuous [Ca II] emission in nebular-phase spectra (Perets et al. 2010; Sullivan et al. 2011; Kasliwal et al. 2012; Valenti et al. 2014; Lunnan et al. 2017; De et al. 2018a). Their photometric evolution is characterized by timescales and peak luminosities shorter and fainter than those of typical core-collapse and thermonuclear SNe, while their photospheric-phase

---

[21] Moore-Sloan, WRF Innovation in Data Science, and DIRAC Fellow.

velocities are largely similar to those of normal SNe Ib/c ($\sim$8000 km s^{-1}; see Filippenko 1997; Gal-Yam 2017 for a review). Yet, their most striking feature remains their preference for remote locations in the far outskirts of galaxies in old quiescent environments, in stark contrast to normal stripped-envelope SNe, which are found close to star formation (Perets et al. 2010; Lunnan et al. 2017). Together with the non-detection of any parent stellar populations in late-time imaging of the locations of these objects, their remote locations suggest that these transients arise from very old progenitors that may have traveled far away from their parent stellar population or were possibly formed in these remote locations (Yuan et al. 2013; Lyman et al. 2014, 2016; Perets 2014; Lunnan et al. 2017).

Their host offset distribution has been shown to be more skewed toward larger offsets than that of SNe Ia and even short gamma-ray bursts (Lunnan et al. 2017), while their hosts are preferentially found in group and cluster environments (Mulchaey et al. 2014; Foley 2015; Lunnan et al. 2017). Shen et al. (2019) show that the radial offset distribution of the sample may be consistent with that of globular clusters, and potentially indicative of a progenitor population that has been kicked out of nearby globular clusters.

The progenitors of Ca-rich gap transients remain unknown to date, and are currently only constrained with circumstantial evidence. Specifically, their remote locations and old host environments point to old progenitors involving white dwarfs (WDs) in binary systems. Suggested channels include helium shell detonations on WDs (Bildsten et al. 2007; Shen et al. 2010; Waldman et al. 2011; Sim et al. 2012; Dessart & Hillier 2015; Meng & Han 2015), double detonations of He shells on the surface of WDs (Sim et al. 2012; Polin et al. 2019a, 2019b), mergers of WDs with neutron stars (Metzger 2012; Margalit & Metzger 2016; Bobrick et al. 2017; Toonen et al. 2018; Zenati et al. 2019), tidal disruptions of WDs by intermediate-mass black holes (Rosswog et al. 2008; MacLeod et al. 2014; Sell et al. 2015; MacLeod et al. 2016; Sell et al. 2018; Kawana et al. 2020), and even extreme core-collapse SNe from highly stripped massive stars (Tauris et al. 2015; Moriya et al. 2017); however their old environments make core-collapse SNe unlikely (Perets et al. 2011). If they arise from binary WD systems, Meng & Han (2015) show that the old environments and consequently long delay times constrain the progenitor binary to consist of low-mass CO ($\lesssim$0.6 $M_\odot$) and He ($\lesssim$0.25 $M_\odot$) WDs.

Constraining their progenitors and rates is important not only for our understanding of these potentially common types of transients, but also for shedding light on a likely common end point in binary stellar evolution involving WDs in binary systems, and their possible significant contribution to the enrichment of the intergalactic medium with Ca (Mulchaey et al. 2014; Mernier et al. 2016). Estimates of the volumetric rates of this population from previous transient experiments include an estimate of 7% ± 5% of the SN Ia rate from the Lick Observatory Supernova Search (LOSS; Perets et al. 2010; Li et al. 2011) and a lower limit of $\approx$3% of the SN Ia rate from the Palomar Transient Factory (PTF; Kasliwal et al. 2012). A later estimate based on post-facto simulations of the detection efficiency and survey cadence of the PTF suggests that their rates may be as high as $\approx$30% of the SN Ia rate (Frohmaier et al. 2018). However, the sample of known objects was found largely by follow-up of isolated events outside of systematic

SN classification efforts, leaving considerable uncertainty on the rates of the class.

The number of reported Ca-rich gap transients in the literature, as well as the diversity in their observed properties, has risen substantially in the last decade with large-scale optical transient surveys. As per the name of the class, the detection of strong [Ca II] emission in the nebular-phase spectra with a high [Ca II]/[O I] ratio[22] is the primary criterion used to relate objects to the class of Ca-rich transients (Valenti et al. 2014; Milisavljevic et al. 2017; De et al. 2018a). In addition, Kasliwal et al. (2012) defined this class of "gap" transients by their (i) faint peak luminosity, (ii) fast photometric evolution, (iii) photospheric-phase velocities similar to those of normal hydrogen-poor SNe ($\sim$8000 km s^{-1}), and (iv) early evolution to the nebular phase, notably without any constraints on the photospheric-phase spectra of the transient. These criteria are consistent with the prototype event of the class SN 2005E (Perets et al. 2010), which is also spectroscopically similar to SNe Ib near peak light.

There are seven other events in the class of Ca-rich gap transients that are spectroscopically similar to SNe Ib/c near peak light—SN 2007ke, SN 2010et, PTF 11bij (Kasliwal et al. 2012), SN 2012hn (Valenti et al. 2014), PTF 11kmb, PTF 12bho (Lunnan et al. 2017) and SN 2016hgs (De et al. 2018a). Other SNe Ic that show evidence of strong [Ca II] emission in the early nebular phase include iPTF 14gqr (De et al. 2018b), SN 2018kzr (McBrien et al. 2019) and SN 2019bkc (Chen et al. 2020; Prentice et al. 2020), although they are more luminous ($M_{\mathrm{peak}} \lesssim -17.5$) than the typical Ca-rich gap transient. However, spectroscopic similarity to SNe Ib/c does not appear to be a defining characteristic of the class. Notable exceptions include PTF 09dav (Sullivan et al. 2011; Kasliwal et al. 2012) and SN 2016hnk (Galbany et al. 2019; Jacobson-Galán et al. 2020), which exhibit similarities to subluminous SN 1991bg–like SNe Ia (Filippenko et al. 1992) near peak light.

Similarly, iPTF 15eqv (Milisavljevic et al. 2017) is a peculiar hydrogen-rich SN IIb that exhibits a high [Ca II]/[O I] ratio in nebular-phase spectra, which show that it is luminous at peak and consistent with a core-collapse SN in a star-forming environment. Another potential member of the class, SN 2005cz (Kawabata et al. 2010; Perets et al. 2011), exhibits a high [Ca II]/[O I] ratio in its nebular-phase spectrum; yet the lack of photometry around peak light precludes a confirmed association with this class of faint and fast-evolving transients, as is the case for several candidates presented in Filippenko et al. (2003).

The large heterogeneity in the peak luminosity and spectroscopic appearance of objects likely points to a diversity in explosions that produce high [Ca II]/[O I] in their nebular-phase spectra. Yet, the small number of total reported events ($\lesssim$10) has prevented a holistic analysis of the spectroscopic and photometric properties of this class. Most previous studies have focused on one or two events, each of which has been suggested to be a unique member of this emerging population which remains poorly understood. In particular, previous works have not characterized the nebular-phase behavior of a systematically selected sample of low-luminosity hydrogen-poor transients to be able to quantitatively place the photometric and spectroscopic properties of the class of Ca-rich gap

---

[22] Throughout this paper, we refer to the flux ratio of the forbidden [Ca II] $\lambda\lambda$7291, 7324 to [O I] λ6300, 6364 lines as [Ca II]/[O I].

transients in a broader context. Such an analysis with a large sample can yield vital clues to trends within the population and shed light on the underlying explosions. The aim of this paper is to systematically uncover and analyze this population of faint and fast-evolving hydrogen-poor events that exhibit high [Ca II]/[O I] in nebular-phase spectra.

While galaxy-targeted SN surveys are sensitive to transients occurring close to their host galaxies, the known preference of these transients for large host offsets necessitates a wide-field search approach that is sensitive to transients at large projected offsets from their host galaxies. Given the faint peak luminosity ($M_r \approx -16$) and relatively low volumetric rates ($\sim$10% of SN Ia rate) of these events, finding a large sample of events requires a sufficiently deep (depth $r \gtrsim 20$ mag to find events out to $\approx$150 Mpc) optical all-sky survey with a cadence of $\lesssim$4 days to detect these short-lived events. At the same time, due to the high rate of higher-redshift SNe Ia at this depth ($\sim$8500 yr^{-1} down to $r = 20$ mag limiting magnitude; Feindt et al. 2019), finding a systematic sample of these local universe events requires a targeted approach to classify transients in the local universe by cross-matching transients to known nearby galaxies. Such an approach is now possible with large catalogs of galaxies with known spectroscopic redshifts like the Census of the Local Universe (CLU; Cook et al. 2019) catalog and GLADE (Dálya et al. 2018).

This paper presents the first in a series of publications from the CLU experiment of the Zwicky Transient Facility (ZTF; Bellm et al. 2019a; Graham et al. 2019). This paper provides an overview of the sample selection and spectroscopic completeness of this volume-limited experiment. Here, we focus on the identification of Ca-rich gap transients, specifically on the class of faint and hydrogen-poor transients that exhibit Ca-rich spectra in the nebular phase. We briefly describe the design of the experiment and sample selection in Section 2. Section 3 presents an analysis of the photometric and spectroscopic properties of the combined sample of transients from ZTF and the literature, specifically noting the presence of two spectroscopic classes and a continuum of properties across these classes. Using the controlled selection criteria of the experiment, we present an analysis of the host environments of these transients in Section 4 while Section 5 presents a discussion on the estimated volumetric rates of these events. In Section 6, we combine all of the results to constrain the progenitors of this class and we summarize our conclusions in Section 7.

Calculations in this paper assume a WMAP9 flat ΛCDM cosmology with $H_0 = 69.3$ km s^{-1} Mpc^{-1} and $\Omega_M = 0.286$ (Hinshaw et al. 2013). We use the median redshift-independent distance estimates from the NASA Extragalactic Database (NED) for transients hosted in galaxies that have such measurements, and redshift-derived distance estimates otherwise. For the redshift-derived distance estimates in this local universe sample ($z < 0.05$), the typical uncertainty in the luminosity distance and projected offsets is $\lesssim$5% for peculiar velocities $\lesssim$ 300 km s^{-1}. Times reported are in Universal Time throughout this paper.

2. Observations

2.1. The CLU Experiment

The ZTF is a wide-field optical time-domain survey running out of the 48 inch Schmidt telescope (P48) at Palomar Observatory (Bellm et al. 2019a; Graham et al. 2019). With a field of view of 47 square degrees, the instrument achieves a median limiting magnitude of $r \approx 20.5$ mag in 30 s exposures of the sky and a survey speed of $\approx$3750 square degrees per hour (Dekany et al. 2016). The ZTF observing time is divided into a public component (40%), a collaboration component (40%), and a Caltech component (20%). Bellm et al. (2019b) provide an overview of the various ZTF surveys undertaken in the first year of operations, and the survey scheduling system designed to carry out operations to maximize volumetric survey speed.

The public component is a 3 day cadence $g + r$ survey of the entire northern sky ($\approx$34% of P48 time) together with a 1 day cadence $g + r$ survey of the Galactic plane ($\approx$6% of P48 time). The collaboration time is dedicated to high-cadence ($3g + 3r$ per night) observations of $\approx$2500 square degrees and a slower-cadence ($\approx$4 days) i-band survey. The Caltech time is dedicated to a one-night cadence $g + r$ survey of $\approx$3000 square degrees. Transients in the difference imaging pipeline (based on the ZOGY subtraction algorithm; Zackay et al. 2016) of ZTF (Masci et al. 2019) are reported and distributed in Avro alert packets[23] (Patterson et al. 2019), including photometry and metadata for the detected transient, as well as a 30 day history for previous detections and non-detections.

The ZTF CLU experiment has been designed to build up a spectroscopically classified sample of transients in the local universe (within 200 Mpc) by classifying all transients found coincident with galaxies in the CLU (Cook et al. 2019) catalog. The CLU catalog consists of $\sim$234,500 galaxies with previously known redshifts compiled from several previous spectroscopic surveys (called CLU-compiled; see Cook et al. 2019), along with additional nearby galaxies found in a wide, narrowband (Hα) survey covering 3π of the northern sky with the Palomar 48 inch telescope (Cook et al. 2019).

The initial filter for the experiment used the CLU-compiled catalog together with $\sim$1000 of the highest-significance ($>25\sigma$) candidates from the Hα survey. Starting from 2019 April, we initiated the use of the next data release, which included a larger sample ($\approx$38,000 candidates with significance $>3\sigma$) of high-confidence nearby galaxies from the CLU Hα survey (see Cook et al. 2019 for a description). Based on the transient sample found in this experiment, we found that $\approx$1% of the transients were hosted in the CLU Hα survey galaxies before the 2019 April update, while $\approx$10% of the transients were hosted in galaxies from the Hα catalog following the inclusion of the next data release.

The CLU experiment was initiated on 2018 June 1 and we restrict the sample of transients in this paper to events saved until 2019 September 30. The sample selection for the transients was implemented as a part of a custom filter implemented on the Global Relay of Observatories Watching Transient Happen (GROWTH) Marshal (Kasliwal et al. 2019), which is a web portal for vetting and coordinating follow-up of transients. The selection criteria for ZTF alerts to be saved in the CLU experiment were as follows:

1. Each alert packet was spatially cross-matched to the CLU catalog of galaxies. The size of the spatial cross-match was set to $3 \times D_{25}$, where D_{25} is the isophotal major axis containing 25% of the total light of the galaxy, as contained in the CLU catalog. If a D_{25} radius was not

---

available for the galaxy, a default cross-match radius of 280″ was used.[24] The cross-matching was performed on the dedicated time-domain astronomy server called `kowalski` at Caltech (Duev et al. 2019).

2. The alert candidate was produced as a positive candidate in the subtraction, i.e., the source flux increased from the reference image.

3. The alert candidate had a real–bogus score of >0.3 as classified by the ZTF machine-learning algorithm (Mahabal et al. 2019). This choice produced a false negative rate of $<3\%$ (Duev et al. 2019).

4. The alert candidate was at least 20″ away from a star brighter than 15.0 mag.

5. Alert candidates within 1″ of a known star in Pan-STARRS1 (PS1; Chambers et al. 2016) were rejected. The identification of stars was based on the machine learning–based star/galaxy classification score presented in Tachibana & Miller (2018), which was available for the three nearest sources in the ZTF alert packets. We used an `sgscore` threshold of 0.6, i.e., candidates within 1″ of a PS1 source with an `sgscore` > 0.6 were rejected.

6. The alert candidate was at least 2″ away from the nearest solar system object and was detected at least twice in the survey separated by 50 minutes. The former criterion removed known asteroids in the ZTF alert stream while the latter removed unknown solar system objects.

No further magnitude cut was applied to this transient stream. This filter produced typically ≈100 sources to be vetted by on-duty astronomers every day, which involved an inspection of the science, reference and difference image cutouts contained in the ZTF alert packets. Human vetting was required to remove alerts from remaining stellar sources that passed the filter, remove variability from known active galactic nuclei (AGNs), and identify remaining bogus sources before assigning appropriate spectroscopic follow-up. For 2018 and 2019, spectroscopic follow-up was exclusively limited to transients within 100″ of the nearest CLU galaxy to remove the large amount of contamination of SNe in background galaxies. In addition, transients coincident with known background galaxies (with known spectroscopic redshifts or photo-$z > 0.1$) were excluded from the sample in order to avoid a large number of false positives from background AGNs and SNe Ia.

As such, the experiment may have been incomplete, excluding transients occurring at very large projected offsets of $>100″$ from their parent galaxies, corresponding to a physical projected distance of 100 kpc at 200 Mpc, 50 kpc at 100 Mpc, and 25 kpc at 50 Mpc. In addition, sources coincident with known AGNs and having a long-term history of variability were not assigned for follow-up. On average, 10–15 SNe were saved for spectroscopic follow-up every week, which were coordinated via source pages on the GROWTH Marshal. Starting from 2019 November, sources from the public ZTF data stream were reported to the Transient Name Server (TNS[25]) as soon as they were saved by a human scanner (De et al. 2019a).

All transients saved after this vetting process were systematically assigned for spectroscopic follow-up. We prioritized follow-up of sources that were brighter than or were going to

peak at brighter than 20 mag (in either r_{ZTF} or g_{ZTF}; see Bellm et al. 2019a), which was selected to be the target limiting magnitude for the experiment. Given the typical ZTF limiting magnitude of 20.5 mag, we did not apply any magnitude cuts to the filter to be able to track the photometric evolution and assign follow-up for transients peaking around 20 mag. Spectroscopic classifications were performed using a multi-tiered approach—(i) sources brighter than 19 mag were assigned for spectroscopic follow-up on the robotic Spectral Energy Distribution Machine (SEDM; Blagorodnova et al. 2018), (ii) sources between 19 and 20 mag were assigned for spectroscopic follow-up on the Double Beam Spectrograph (DBSP; Oke & Gunn 1982) on the 200 inch Hale telescope (P200) at Palomar Observatory, and (iii) sources fainter than 20 mag were assigned for lower-priority follow-up on P200 + DBSP.

Sources assigned to the SEDM queue remained as follow-up targets for a duration of 7 days, after which they were re-assigned to SEDM if still brighter than 19 mag or to P200 otherwise. Spectroscopic follow-up on P200 was required for bright sources (<19 mag) coincident with the nuclei of nearby galaxies, where host galaxy contamination was difficult to remove in the SEDM spectra. In cases where P200 classifications were not possible due to poor weather or due to large host contamination in P200 data for faint targets, we also used the Low Resolution Imaging Spectrometer (LRIS; Oke et al. 1995) on the Keck I telescope for spectroscopic classifications.

The spectroscopic follow-up effort for bright sources ($m < 19$ mag) was coordinated with the Bright Transient Survey (BTS; Fremling et al. 2019) experiment, which aims to classify all transients brighter than 19 mag in the ZTF public alert stream. Community follow-up for bright transients overlapping with BTS also aided in the spectroscopic classification completeness of the sample. Classifications were done with the `SuperNova IDentification` (SNID; Blondin & Tonry 2007) code by automatic execution on spectra produced by the SEDM automated pipeline (Rigault et al. 2019) and by manual execution for all other instruments. For spectra contaminated by the underlying host light, we used `superfit` (Howell et al. 2005) to attempt host subtraction and derive a classification. The final classification was made by human inspection of the best-fit templates matched from SNID or `superfit`.

2.2. Spectroscopic Completeness

The aim of the tiered approach to spectroscopic classification was to obtain high spectroscopic completeness for transients that peaked brighter than 20 mag in galaxies within the local universe. This magnitude limit corresponds to a luminosity completeness of $M < -16.5$ mag for all galaxies in the 200 Mpc volume of the CLU catalog and $M < -15$ mag for galaxies within 100 Mpc. However, given the galaxy-targeted nature of the target selection, the experiment was not sensitive to transients that occurred in nearby galaxies with previously unknown spectroscopic redshifts. Based on results from the ZTF BTS, the completeness (in terms of galaxy count) of the compiled catalog was ≈80% at the lowest redshifts and decreased to ≈50% at the edge of the 200 Mpc volume (Fremling et al. 2019).

While an effort was made to have complete spectroscopic classifications to a depth of ≈20 mag, classifications were not always possible due to several reasons. These included the

---

[24] 280″ is 3× the median D_{25} value of all galaxies in the CLU catalog.
[25] https://wis-tns.weizmann.ac.il/

difficulty of following up transients found close to the Sun and of classifying transients on the nuclei of bright galaxies (where low-resolution SEDM spectra were dominated by host galaxy light) that faded before a scheduled run on the P200/Keck, and the loss of P200/Keck time in periods of bad weather. We thus evaluated the spectroscopic completeness of the experiment in the first year of operations.

We restricted this sample to transients that were saved between[26] 2018 June 1 and 2019 September 30, and to sources detected in any of the public or internal collaboration surveys (note that the public survey has the largest footprint on the sky). We defined our primary sample of sources such that they were detected at least twice, and peaked at a magnitude brighter than 20 mag in either the r_{ZTF} or the g_{ZTF} filter. We required at least two detections of the transient separated by 50 minutes during the survey, as implemented in the alert filter. Multiple detections in the same filter on a single night were averaged to estimate the transient flux on each night.

A total of 852 candidate SNe were saved during this time period, out of which 563 were also included in the BTS program. Of these 852 events, 754 were reliably classified, while 98 were unclassified either due to the lack of follow-up spectroscopy or due to ambiguous classifications from spectroscopic data. As such, the spectroscopic completeness of the complete acquired sample was 88.5% for all transients that had at least one detection brighter than 20 mag. The corresponding classification completeness for $m_{peak} < 19$ mag was 92.9%, that for $m_{peak} < 18$ mag was 98.0%, and that for $m_{peak} < 17$ mag was 98.6% for the entire experiment duration mentioned above. We show a cumulative plot of the number of sources saved and classified as a function of the peak magnitude in Figure 1.

2.3. Sample of Ca-rich Gap Transients

This work focuses on the sample of Ca-rich gap transients identified in this experiment in the aforementioned period of operations (i.e., from 2018 June 1 to 2019 September 30). Given the large number of SNe that were classified as a part of the experiment, it was not possible to perform a nebular-phase spectroscopic follow-up of all events. We thus identified candidate Ca-rich gap transients with simple selection criteria using photometry from the ZTF survey and peak light spectroscopic properties (from the classification effort), focusing on the population of hydrogen-poor low-luminosity events in the sample. Although the criteria were motivated by the known properties of the previous sample of events, we deliberately kept these minimal for candidate selection due to the uncertainties on the intrinsic properties of the class and the small number of previously reported events. The candidate selection criteria were as follows:

1. The transient should have a peak luminosity (in the g_{ZTF} or r_{ZTF} filter) fainter than $M = -17$ mag at the known redshift of the host galaxy (after correcting for Galactic extinction, but not for possible host galaxy extinction). We required at least two detections on the rise of the light curve in the same filter to be able to constrain the peak luminosity.
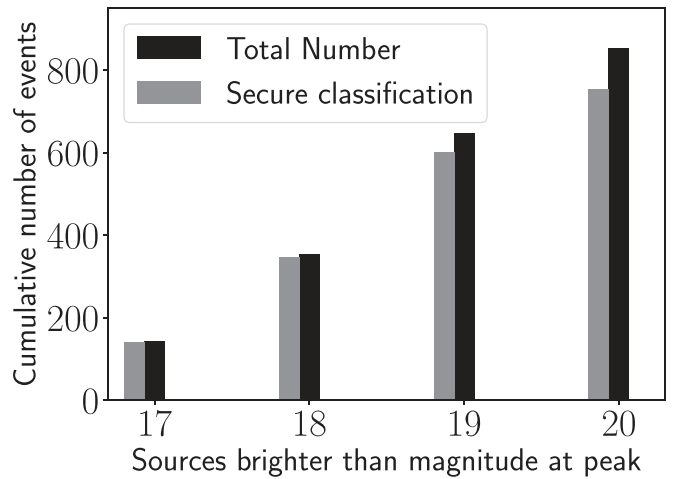
Figure 1. Cumulative number of events that were saved (in black) and classified (in gray) as a function of the peak magnitude in the CLU sample of events.

2. The spectroscopic properties of the source should be consistent with a hydrogen-poor SN near peak light. We did not include any events that exhibited broad hydrogen features in their spectra (i.e., Balmer lines that did not emanate from the underlying host galaxy). We obtained at least one epoch of late-time (at $\gtrsim 30$ days after peak light) spectroscopy with DBSP and LRIS on the Keck I telescope for events that passed (1) and this criterion.

3. We required that the sources exhibit an early transition to the nebular phase, which we confirmed by either the appearance of nebular emission lines and a fading continuum starting at $+30$ days from peak light or a complete transition to the nebular phase by ≈ 150 days after peak light.

4. As strong [Ca II] emission is the hallmark feature of this class, we required that the nebular-phase spectrum exhibit [Ca II]/[O I] > 2 (Milisavljevic et al. 2017; De et al. 2018a) at any phase where the spectrum exhibited nebular emission lines.

Comparing the selection criteria to those of Kasliwal et al. (2012), we note that we did not select candidates based on the fast photometric evolution or photospheric-phase velocities. This choice made us more sensitive to events with larger diversity in ejecta masses and velocities. After applying selection criteria (1) and (2) to the sample of events in the volume-limited experiment, we were left with 22 events, which were followed up with spectroscopy in the nebular phase. Seven of these 22 sources were found to qualify for the criterion [Ca II]/[O I] > 2 in the nebular phase, which defined the primary sample for this paper. In addition, we present observations of SN 2018gwo, a nearby SN Ic that was not detected in ZTF data before its peak (due to a maintenance break in 2018 October), but was recovered on its radioactive decline tail. Combining these observations with publicly available photometry and spectroscopy, we show that SN 2018gwo is a likely Ca-rich gap transient at a distance of 28 Mpc.

We applied the same selection criteria to the published literature sample of Ca-rich gap transients to include them as our comparison sample. The set of 10 literature events satisfying our cuts comprised SN 2005E, SN 2007ke, PTF 09dav, SN 2010et, PTF 11bij, SN 2012hn, PTF 11kmb, PTF 12bho, SN 2016hgs,

Table 1
Summary of the Properties of the Faint Hydrogen-poor Transients Selected for Nebular Phase Follow-up in This Work

Object	R.A. J2000	Decl. J2000	Spec. Type	Peak r Mag. (Abs. Mag.)	[Ca II]/[O I] Flux Value/Phase (days)	Redshift	Host Offset (″/kpc)
ZTF 18aayhylv/SN 2018ckd	$14^h06^m11^s\!.94$	$+09°20'39''\!.33$	Ca-Ib	-16.17	$>3.38/+58$	0.024	39.03/19.08
ZTF 18abmxelh/SN 2018lqo	$16^h28^m43^s\!.26$	$+41°07'58''\!.66$	Ca-Ib	-16.21	$>12.5/+49$	0.033	23.25/15.46
ZTF 18abttsrb/SN 2018lqu	$15^h54^m11^s\!.47$	$+13°30'50''\!.87$	Ca-Ib	-16.44	$>8.38/+31$	0.036	37.12/26.70
ZTF 18acbwazl/SN 2018gwo*	$12^h08^m38^s\!.82$	$+68°46'44''\!.42$	Ca-Ic	<-16.0	$5.16/+53$	0.008	54.20/8.56
ZTF 18acsodbf/SN 2018kjy	$06^h47^m17^s\!.96$	$+74°14'05''\!.90$	Ca-Ib	-15.63	$4.44/+111$	0.018	17.18/6.35
ZTF 19aaznwze/SN 2019hty	$12^h55^m33^s\!.03$	$+32°12'21''\!.70$	Ca-Ib	-16.38	$>3.27/+38$	0.023	18.74/8.73
ZTF 19abrdxbh/SN 2019ofm	$14^h50^m54^s\!.65$	$+27°34'57''\!.59$	Ca-Ia	-17.03	$>2.13/+175$	0.030	18.24/11.16
ZTF 19abwtqsk/SN 2019pxu	$05^h10^m12^s\!.60$	$-00°46'38''\!.63$	Ca-Ib	-16.56	$>8.30/+146$	0.028	30.93/17.56
ZTF 19aamfupk/SN 2019ccm	$04^h41^m05^s\!.36$	$+73°40'23''\!.10$	SN Ib	-16.40	$1.18/+207$	0.015	14.73/4.54
ZTF 19aanfsmc/SN 2019txl	$09^h32^m59^s\!.36$	$+27°30'07''\!.80$	SN Ib	-16.21	$0.87/+330$	0.034	11.68/7.96
ZTF 19aasqseq/SN 2019txt	$09^h59^m06^s\!.38$	$+17°49'09''\!.99$	SN Ib	-15.90	$1.34/+180$	0.026	19.94/10.69
ZTF 19abgqruu/SN 2019mjo	$00^h06^m59^s\!.83$	$+03°27'39''\!.70$	SN Ib-pec	-16.62	$NN/+180$	0.041	12.38/10.06
ZTF 18abdffeo/SN 2018dbg	$14^h17^m58^s\!.86$	$+26°24'44''\!.59$	SN Ib/c	-16.65	$NN/+22$	0.015	2.01/0.61
ZTF 19aarrdoz/SN 2019txr	$08^h42^m31^s\!.91$	$+56°17'42''\!.19$	SN Ib/c	-16.73	$<1/+270$	0.044	1.95/1.71
ZTF 18aboabxv/SN 2018fob	$15^h13^m07^s\!.23$	$+41°16'11''\!.07$	SN Ic	-16.93	$0.87/+212$	0.029	18.47/10.84
ZTF 19aadttht/SN 2019yz	$15^h41^m57^s\!.30$	$+00°42'39''\!.41$	SN Ic	-16.63	$0.59/+242$	0.006	34.17/4.54
ZTF 19aadwtoe/SN 2019abb	$07^h54^m17^s\!.26$	$+14°16'22''\!.42$	SN Ic	-16.56	$0.79/+357$	0.015	4.26/1.34
ZTF 19aailcgs/SN 2019ape	$10^h51^m42^s\!.55$	$+18°28'52''\!.62$	SN Ic	-16.62	$0.87/+180$	0.021	11.53/4.79
ZTF 19abhhdwf/SN 2019ouq	$17^h01^m41^s\!.94$	$+30°06'34''\!.43$	SN Ic	-16.68	$<1/+170$	0.036	8.71/6.27
ZTF 18acushie/SN 2018kqr	$08^h50^m03^s\!.60$	$+55°10'09''\!.54$	SN Ic-BL	-16.75	$NN/+16$	0.045	3.15/2.82
ZTF 19aavlfvn/SN 2019gau	$14^h38^m10^s\!.42$	$+10°08'04''\!.93$	SN Ia	-16.75	$—/+260$	0.028	1.30/0.73
ZTF 19aawhlcn/SN 2019gsc	$14^h37^m45^s\!.25$	$+52°43'36''\!.28$	SN Ia 02cx	-13.90	$NN/+60$	0.011	10.99/2.50
ZTF 19abalbim/SN 2019ttf	$18^h42^m15^s\!.87$	$+24°53'48''\!.99$	SN Ia 02cx	-13.99	$NN/+230$	0.011	11.07/2.52

Note. The column Spec. Type only refers to the spectroscopic appearance of the object near peak light. The Ca-rich objects are indicated with Ca in the Spec. Type column. For cases where the object did not turn nebular even at the latest phases of spectroscopic follow-up, we indicate the [Ca II]/[O I] flux ratio with NN and indicate the phase of the latest available spectrum. In the case of SN 2018gwo (indicated with *), the object did not pass the primary selection criteria but is a likely Ca-rich gap transient when we combined publicly available photometry and nebular-phase follow-up from our campaign. Details on the objects that did not pass the nebular-phase criterion are discussed in Appendix, highlighting why each object was excluded from the Ca-rich sample. For one event (SN 2019gau), we did not detect nebular emission features and hence denote the [Ca II]/[O I] ratio with –.

and SN 2016hnk. Table 1 summarizes the photometric and spectroscopic properties of all the transients identified for nebular phase follow-up. Here, we describe the initial detection to the final classification of each of the individual objects in the sample of Ca-rich gap transients presented in this paper. We present a discussion of the properties of the remaining objects that passed the light-curve criteria but did not pass the nebular-phase criterion in Appendix, specifically highlighting how we determined the Ca-rich classification for each event. Henceforth, we refer to all phases with respect to the time of the r-band peak (see Section 3.3.1).

2.3.1. SN 2018ckd/ZTF 18aayhylv

ZTF 18aayhylv (=SN 2018ckd) was first detected in the ZTF difference imaging pipeline on 2018 June 7.19 (Modified Julian Date (MJD) = 58,276.19) at J2000 coordinates $\alpha = 14{:}06{:}11.95$ and $\delta = 09{:}20{:}39.3$, at a magnitude of $r = 19.39 \pm 0.09$ mag. The transient passed the filter on the GROWTH Marshal on 2019 June 10 (second detection) and was saved for spectroscopic follow-up. The transient was detected by the Catalina Real-time Transient Survey (Drake et al. 2009) on 2019 June 12, was reported to the TNS on the same date (Crts 2018), and was assigned the International Astronomical Union (IAU) name AT 2018ckd. The transient was not detected in the ZTF alert production pipeline on 2018 June 1.31 to a 5σ limit of $r \approx 19.82$ mag. However, the transient was detected at $\approx 4\sigma$ significance with $r \approx 20.25$ mag with forced photometry (see Section 2.4) at the transient location in the ZTF difference images

(Masci et al. 2019). The last non-detection of the source in forced photometry was at 2018 May 29.31 down to a 5σ limit of $r \approx 19.65$ mag.

The transient was found in the outskirts of NGC 5463, an S0 galaxy at $z = 0.024$ (Figure 2), at a projected offset of $\approx 39''\!.0$ from the host center, corresponding to a physical separation of ≈ 19.1 kpc. We obtained a spectrum of ZTF 18aayhylv with DBSP on 2018 June 12, which exhibited P-Cygni features of He I and Ca II similar to SNe Ib. Subsequent photometry from ZTF and follow-up with P60 + SEDM confirmed a faint and fast-evolving (rise time $\lesssim 15$ days) light curve peaking at an absolute magnitude of $M \approx -16.0$ mag (Figure 3). A nebular-phase spectrum of the source at $\approx +60$ days from the r-band peak with LRIS on the Keck I telescope showed strong [Ca II] emission lines with weak [O I] emission, confirming an early transition to the nebular phase and the classification of this source as a Ca-rich gap transient.

2.3.2. SN 2018lqo/ZTF 18abmxelh

ZTF 18abmxelh (=SN 2018lqo) was first detected in the ZTF difference imaging pipeline on 2018 August 10.18 (MJD = 58,340.18) at J2000 coordinates $\alpha = 16{:}28{:}43.26$ and $\delta = 41{:}07{:}58.7$, at a magnitude of $r = 20.11 \pm 0.17$ mag. The transient passed the machine-learning thresholds on the GROWTH Marshal on 2019 August 16 and was saved for spectroscopic follow-up. We reported the transient to the TNS on 2019 October 28 (De 2019a), leading to its IAU name of AT 2018lqo. With forced photometry on the ZTF difference
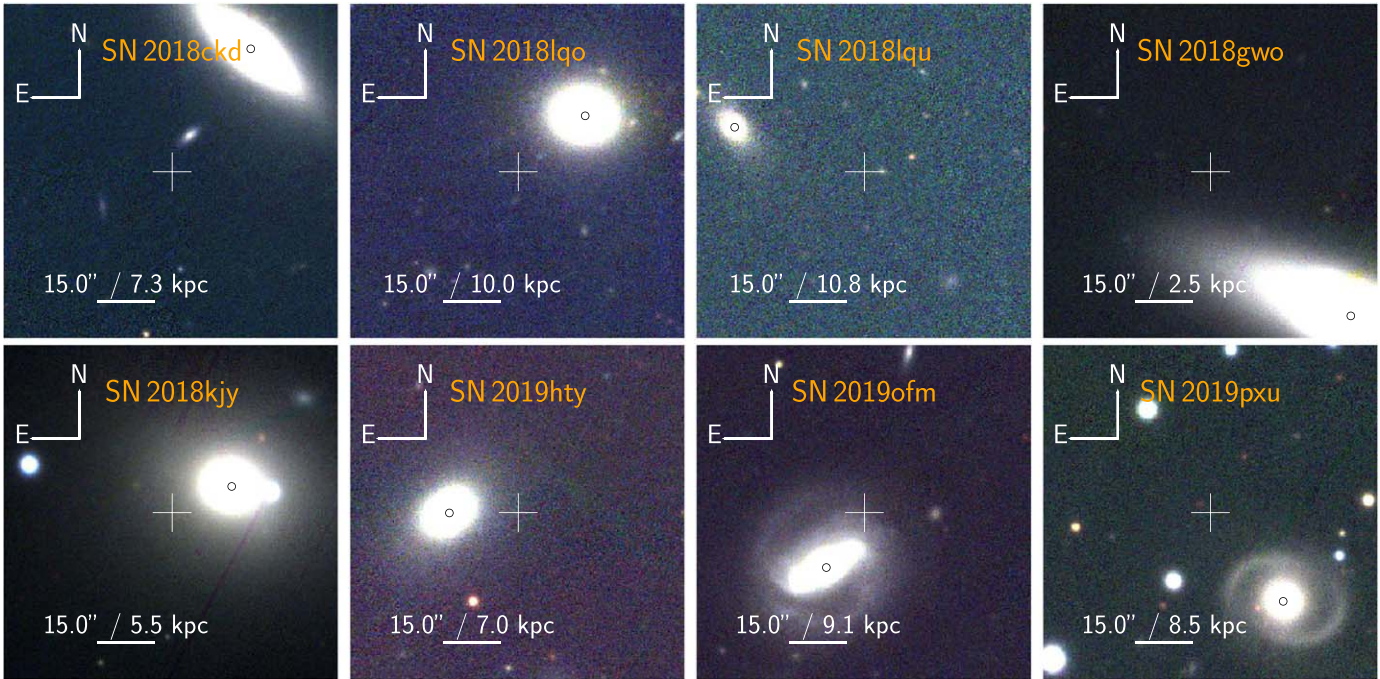
Figure 2. RGB composite archival images of the locations of the eight Ca-rich gap transients in the ZTF CLU sample. The images were taken from the PS1 survey (Chambers et al. 2016). In each panel, the white cross-hair shows the location of the detected transient and the scale shows the projected angular size and physical scale at the redshift of the host galaxy. The apparent host galaxy is marked with a black circle at its core in each panel.

images, we found that the transient was not detected on 2018 August 07.18 (MJD = 58,337.18) down to a 5σ limit of $r \approx 21.16$ mag. The transient exhibited an initial fading of ≈ 0.7 mag in ≈ 3 days following the first detection, followed by a rise to a peak ≈ 10 days later.

The transient was found in the outskirts of CGCG 224-043, an E-type galaxy at $z = 0.032$ (Figure 2), at a projected offset of $\approx 23\farcs2$, corresponding to a physical separation of ≈ 15.5 kpc. We obtained a spectrum of ZTF 18abmxelh with DBSP on 2018 August 21, which exhibited P-Cygni features of He I and Ca II similar to SNe Ib. Subsequent photometry from ZTF and follow-up with P60 + SEDM indicated a faint and fast-evolving (rise time $\lesssim 15$ days) light curve peaking at an absolute magnitude of $M \approx -16.1$ mag (Figure 3). A nebular-phase spectrum of the source at $\approx +50$ days from the r-band peak with LRIS on the Keck I telescope showed strong [Ca II] emission lines, confirming a fast nebular-phase transition and the classification of this source as a Ca-rich gap transient.

2.3.3. SN 2018lqu/ZTF 18abttsrb

ZTF 18abttsrb (=SN 2018lqu) was first detected in the ZTF difference imaging pipeline on 2018 September 3.13 (MJD = 58,364.13) at J2000 coordinates $\alpha = 15{:}54{:}11.48$ and $\delta = +13{:}30{:}50.9$, at a magnitude of $r = 20.14 \pm 0.33$ mag. The transient was saved as a candidate SN on its second detection on 2018 September 7, and assigned for spectroscopic follow-up. We reported the transient to the TNS on 2019 November 6 (De 2019b), leading to its IAU name of AT 2018lqu. With forced photometry on the ZTF difference images, we found that the transient was not detected on 2018 August 16.17 (MJD = 58,346.17) down to a 5σ limit of $r \approx 21.16$ mag.

The transient was found in the outskirts of WISEA J155413.91+133102.4, an E-type galaxy at $z = 0.035$ (Figure 2), at a projected offset of $\approx 37\farcs1$, corresponding to a

physical separation of ≈ 26.7 kpc. We obtained a spectrum of ZTF 18abttsrb with DBSP on 2018 September 12, which exhibited P-Cygni features of He I and Ca II similar to SNe Ib. Subsequent photometry from ZTF and follow-up with P60 + SEDM indicated a faint and fast-evolving (rise time $\lesssim 15$ days) light curve peaking at an absolute magnitude of $M \approx -16.4$ mag (Figure 3). A nebular-phase spectrum of the source at $\approx +30$ days from the r-band peak with LRIS on the Keck I telescope showed strong [Ca II] and weak [O I] emission lines, confirming an early transition to the nebular phase and the classification of this source as a Ca-rich gap transient.

2.3.4. SN 2018gwo/ZTF 18acbwazl/Gaia 18dfp/PS 19lf

ZTF 18acbwazl (= SN 2018gwo) was first detected in the ZTF difference imaging pipeline on 2018 October 31.49 (MJD = 58,422.49) at J2000 coordinates $\alpha = 12{:}08{:}38.83$ and $\delta = +68{:}46{:}44.4$, at a magnitude of $g = 19.20 \pm 0.17$ mag. Since the source was detected multiple times on the same night as part of the collaboration high-cadence survey, the source was saved to the GROWTH Marshal on 2018 October 31. The source was detected by ZTF after a month-long gap in survey operations due to maintenance on the P48 camera. The source was first detected on 2018 September 28 by Wiggins (2018) at 16.4 mag (clear filter) and reported to the TNS with the IAU name AT 2018gwo, shortly after the sky region emerged from solar conjunction. An upper limit of 17 mag was reported on the previous night. A low-resolution spectrum from the Three Hills Observatory was reported to the TNS on 2018 September 30 and 2018 October 6 by Leadbeater (2018), consistent with an SN Ib/c with a reddened continuum near peak light, causing this source to be renamed SN 2018gwo. Subsequent ZTF photometry showed that the source was detected by ZTF on its post-peak decline tail. We obtained a spectrum of the source
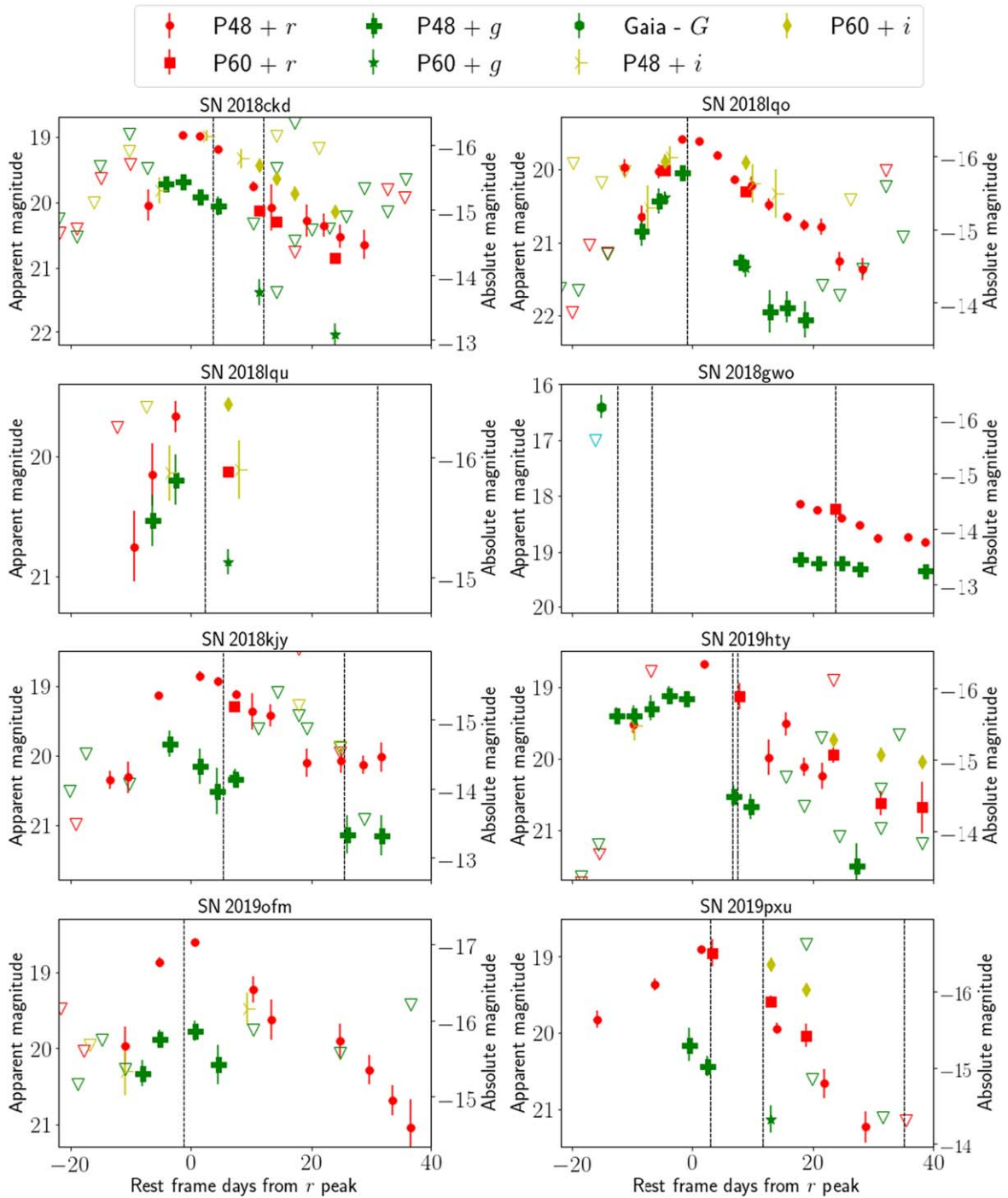
Figure 3. Photometric evolution near peak light of the Ca-rich gap transients presented in this sample, with time presented with respect to the *r*-band light curve of the individual sources (corrected for Galactic extinction). Filled symbols denote detections from forced photometry on the ZTF difference images (see figure legend), while hollow inverted triangles denote 5σ upper limits at the position of the transient. Red points denote *r*-band photometry, green points denote *g*-band photometry, yellow points denote *i*-band photometry, and cyan points denote photometry in the clear filter. The vertical dashed lines denote the epochs of spectroscopy. For SN 2018gwo, we also show public TNS photometry from Gaia & Wiggins (2018) (see legend).

with P60 + SEDM on 2018 November 6, which exhibited a weak continuum with emerging broad [Ca II] and Ca II lines.

The transient was found in the outskirts of NGC 4128, an S0 galaxy at a distance (median reported in NED) of 28.6 Mpc (Figure 2), at a projected offset of ≈54″.2 corresponding to a physical projected distance of ≈8.6 kpc. Although the transient was not detected by ZTF around peak light, we found the public observations combined with the follow-up to be

consistent with a Ca-rich gap transient. First, the initial detection and prior non-detection of the source reported by P. Wiggins suggest a fast rise to an absolute magnitude of $M \approx -16.0$ mag (in clear filter; Figure 3). The transient subsequently declined rapidly by ≈2 mag within ≈30 days after peak, confirming the faint peak luminosity and fast photometric evolution of the event. The peak light spectra together with the SEDM spectrum taken at ≈30 days are

consistent with an SN Ib/c[27] in the photospheric phase, which exhibits a fast transition to the nebular phase. We obtained a follow-up spectrum of the transient with LRIS on the Keck I telescope on 2018 December 04, which exhibited strong [Ca II] emission and weak [O I] emission, confirming the classification of this source as a Ca-rich gap transient.

2.3.5. SN 2018kjy/ZTF 18acsodbf/PS 18cfh

ZTF 18acsodbf (= SN 2018kjy) was first detected in the ZTF difference imaging pipeline on 2018 December 3.36 (MJD = 58,455.36) at J2000 coordinates $\alpha = 06:47:17.96$ and $\delta = +74:14:05.9$, at a magnitude of $r = 19.56 \pm 0.14$ mag. The transient was saved as a candidate SN on its second detection on 2018 December 4, and assigned for spectroscopic follow-up. The transient was detected by the PS1 survey (Chambers et al. 2016) on 2018 December 17 and reported to the TNS on 2018 December 22 (Chambers et al. 2018), acquiring the IAU name AT 2018kjy. With forced photometry on the ZTF difference images, we found three more lower-significance detections up to ≈ 7 days before the first alert was issued. The last non-detection of the source was on 2018 November 19.48 (MJD = 58,442.48) to a 5σ limit of $g \approx 20.45$ mag.

The transient was found in the outskirts of NGC 2256, an E-type galaxy at $z = 0.017$ (Figure 2), at a projected offset of $\approx 17\rlap{.}''2$, corresponding to a physical separation of ≈ 6.4 kpc. We obtained a spectrum of ZTF 18acsodbf with DBSP on 2018 December 14, which exhibited narrow P-Cygni features of He I, O I, and Ca II and a reddened continuum similar to the Ca-rich gap transient PTF 12bho (Lunnan et al. 2017). Subsequent photometry from ZTF and follow-up with P60 + SEDM confirmed a faint and fast-evolving (rise time ≈ 17 days) light curve peaking at an absolute magnitude of $M \approx -15.6$ mag (Figure 3). Subsequent spectra of the source taken with Keck/ LRIS $+30$ days and $+120$ days from the peak showed a fast transition to the nebular phase dominated by [Ca II] emission, confirming its classification as a Ca-rich gap transient.

2.3.6. SN 2019hty/ZTF 19aaznwze/ATLAS 19nhp/PS 19bhn

ZTF 19aaznwze (= SN 2019hty) was first detected in the ZTF difference imaging pipeline on 2019 June 14.18 (MJD = 58,648.18) at J2000 coordinates $\alpha = 12:55:33.03$ and $\delta = +32:12:21.7$, at a magnitude of $g = 19.62 \pm 0.19$ mag. The transient passed the machine-learning thresholds on the GROWTH Marshal on 2019 June 20 and was saved for spectroscopic follow-up. The transient was detected by the Asteroid Terrestrial-impact Last Alert System (ATLAS) survey (Tonry et al. 2018) on 2019 June 19 (Tonry et al. 2019a), reported to the TNS on the same date, and assigned the IAU name AT 2019hty. With forced photometry on the ZTF difference images, we found an additional detection of the source on 2019 June 11.24 (MJD = 58,645.24) at a magnitude of $g = 19.52 \pm 0.12$. The last non-detection of the source was on 2019 June 08.23 (MJD = 58,642.23) to a 5σ limit of $r \approx 21.43$ mag.

The transient was found in the outskirts of WISEA J125534.50+321221.5, an E-type galaxy at $z = 0.023$ (Figure 2), at a projected offset of $\approx 18\rlap{.}''7$, corresponding to a

physical separation of ≈ 8.7 kpc. We obtained a spectrum of ZTF 19aaznwze with SEDM and DBSP on 2019 July 1, which exhibited a Type Ib–like spectrum with a reddened continuum and a broad P-Cygni feature of the Ca near-infrared (NIR) triplet. Photometric follow-up with SEDM and data from ZTF showed a faint peak magnitude of $M \approx -16.1$ mag and a rise time of ≈ 15 days (Figure 3). We obtained an additional spectrum of the source with DBSP at ≈ 40 days from peak light, which showed a broad emerging line of [Ca II] and weak [O I], confirming a fast transition to the nebular phase dominated by [Ca II] emission, and classifying this source as a Ca-rich gap transient.

2.3.7. SN 2019ofm/ZTF 19abrdxbh/ATLAS 19tjf

ZTF 19abrdxbh (= SN 2019ofm) was first detected in the ZTF difference imaging pipeline on 2019 August 20.15 (MJD = 58,715.15) at J2000 coordinates $\alpha = 14:50:54.65$ and $\delta = +27:34:57.6$, at a magnitude of $g = 20.43 \pm 0.24$ mag. The transient met the machine-learning thresholds and was saved to the GROWTH Marshal on 2019 August 24. ZTF detection was reported by the AMPEL (Nordin et al. 2019b) automatic stream to the TNS on 2019 August 23 (Nordin et al. 2019a), acquiring for it the IAU name AT 2019ofm. With forced photometry on the ZTF difference images, we found an additional detection of the source on 2019 August 17.24 (MJD = 58,712.24) at a magnitude of $r = 20.07 \pm 0.26$. The last non-detection of the source was on 2019 August 17.15 (MJD = 58,712.15) to a 5σ limit of $g \approx 20.40$ mag.

The transient was found on top of the spectroscopic binary–type galaxy IC 4514 at $z = 0.030$ (Figure 2), at a projected offset of $\approx 18\rlap{.}''2$, corresponding to a physical offset of ≈ 11.2 kpc. We obtained a spectrum of the source with DBSP on 2019 August 27, which exhibited clear features of a 1991bg-like SN Ia at the host redshift. Following the first detection, the source rose to a peak absolute magnitude of $M_r \approx -16.6$ mag, suggesting a subluminous SN Ia consistent with the spectroscopic classification. We obtained a follow-up spectrum of the source with LRIS at ≈ 175 days after peak light, which showed that the source had transitioned to the nebular phase exhibiting [Ca II] as the only detectable broad feature in the spectrum. Together with the non-detection of Fe-group features typically seen in 1991bg-like objects, the strong [Ca II] feature suggested that SN 2019ofm was similar to the Ca-rich gap transients PTF 09dav and SN 2016hnk, thus classifying the source as a Ca-rich gap transient.

2.3.8. SN 2019pxu/ZTF 19abwtqsk/ATLAS 19uvg/PS 19fwq

ZTF 19abwtqsk (=SN 2019pxu) was first detected in the ZTF difference imaging pipeline on 2019 September 4.50 (MJD = 58,730.50) at J2000 coordinates $\alpha = 05:10:12.61$ and $\delta = -00:46:38.6$, at a magnitude of $r = 20.09 \pm 0.20$ mag. The transient met the machine-learning thresholds and was saved to the GROWTH Marshal on 2019 September 22 on its third detection in the ZTF alert stream. The transient was detected by the ATLAS survey on 2019 September 10 (Tonry et al. 2019b) and reported on the same date to the TNS, acquiring the IAU name AT 2019pxu. The field was not covered by the survey >30 days before the first detection, and hence we were unable to determine a recent upper limit from the first detection.

---

[27] Although not used as a defining characteristic of the class, the only SNe Ib/ c reported thus far in the outskirts of early-type galaxies are found to be Ca-rich gap transients.

Table 2
Photometry of All the Sources Presented in This Paper

Object	MJD	Rest-frame Phase (days from r peak)	Filter	Magnitude	Instrument
SN 2018ckd	58,242.31	−34.53	r	>20.53	P48+ZTF
SN 2018ckd	58,245.34	−31.57	r	>18.89	P48+ZTF
SN 2018ckd	58,248.27	−28.71	r	>20.95	P48+ZTF
SN 2018ckd	58,255.26	−21.88	r	>20.70	P48+ZTF
SN 2018ckd	58,258.25	−18.96	r	>20.64	P48+ZTF
SN 2018ckd	58,262.30	−15.01	r	>19.87	P48+ZTF
SN 2018ckd	58,267.31	−10.12	r	>19.65	P48+ZTF
SN 2018ckd	58,270.32	−7.18	r	20.28 ± 0.24	P48+ZTF
SN 2018ckd	58,276.19	−1.45	r	19.21 ± 0.03	P48+ZTF
SN 2018ckd	58,279.17	1.46	r	19.23 ± 0.04	P48+ZTF
SN 2018ckd	58,282.19	4.41	r	19.42 ± 0.04	P48+ZTF
SN 2018ckd	58,285.17	7.32	r	>18.28	P48+ZTF
SN 2018ckd	58,288.24	10.32	r	19.99 ± 0.08	P48+ZTF
SN 2018ckd	58,289.23	11.29	r	20.36 ± 0.07	P60+SEDM
SN 2018ckd	58,291.24	13.25	r	20.32 ± 0.35	P48+ZTF
SN 2018ckd	58,292.25	14.24	r	20.54 ± 0.09	P60+SEDM
SN 2018ckd	58,295.24	17.16	r	>21.00	P60+SEDM
SN 2018ckd	58,297.27	19.14	r	20.52 ± 0.25	P48+ZTF
SN 2018ckd	58,300.18	21.98	r	20.59 ± 0.18	P48+ZTF
SN 2018ckd	58,302.25	24.00	r	21.08 ± 0.07	P60+SEDM

Notes. The photometry has not been corrected for Galactic extinction. Phases are indicated with respect to the time from the best-fit r-band peak. Upper limits are at 5σ confidence at the location of the transient.

(This table is available in its entirety in machine-readable form.)

The transient was found in the outskirts of the spiral galaxy WISEA J051011.32-004702.5 at $z = 0.028$, at a projected offset of $\approx 30\farcs9$ (Figure 2), corresponding to a physical projected offset of ≈ 17.6 kpc. We obtained a peak light spectrum of the source with P200 + DBSP on 2019 October 3, which exhibited a Type Ib–like spectrum and a reddened continuum similar to the Ca-rich gap transient PTF 12bho. Subsequent photometry from ZTF and P60 + SEDM indicated a rise time of ≈ 17 days and a faint peak absolute magnitude of $M = -16.4$ mag. We obtained a follow-up spectrum with LRIS on 2019 October 27, which showed a faint continuum with emerging broad emission lines of [Ca II] and Ca II, confirming a fast nebular transition and the classification of the source as a Ca-rich gap transient.

2.4. Photometry

We obtained *gri* photometry of the transients from data taken with the P48 ZTF camera (Bellm et al. 2019a), which were processed with the ZTF data processing system (Masci et al. 2019). Light curves were extracted using forced point-spread function (PSF) photometry (Masci et al. 2019) at the location of the transient in the difference images, where the location was determined from the median position of the source reported in all alerts of the transient in the ZTF transient detection pipeline. We report detections of the transients in the forced photometry for epochs where the signal-to-noise ratio (S/N) was higher than 3σ, while 5σ upper limits are reported for other epochs. We include data acquired in the public survey as well as those acquired in the higher-cadence internal collaboration and Caltech surveys. In cases where the transient was covered by an internal survey and had more than one visit per night, we performed an inverse variance weighted binning of the flux measurements in bins of 2.5 days to improve the S/N of the measurements. We performed the same binning for reporting

upper limits, where we used the inverse variance weighted flux uncertainty to report the 5σ upper limit for that epoch.

We obtained additional multi-color photometry near peak light with the SEDM rainbow camera on the Palomar 60 inch telescope, and the data were processed using the SEDM image reduction pipeline. Image subtraction against archival references from the Sloan Digital Sky Survey (SDSS) and PS1 was performed, and difference magnitudes were obtained using the pipeline described in Fremling et al. (2016). We show the photometric evolution of these transients near peak light in Figure 3, while the data are presented in Table 2. We corrected the photometry for foreground Galactic extinction using the maps in Schlafly & Finkbeiner (2011) and the extinction law of Cardelli et al. (1989), assuming $R_V = 3.1$.

2.5. Late-time Imaging

We obtained additional late-time photometry of the transients with the Wafer-scale Imager for Prime (WaSP) on the Palomar 200 inch telescope, which was reduced with the pipeline described in De et al. (2020). We used LRIS on the Keck I telescope for late-time imaging of some transients reported in this paper, and the data were reduced using the automated `lpipe` pipeline (Perley 2019). Image subtraction was not necessary for the late-time imaging for most sources since the majority were far from their host galaxies, and we report aperture photometry measurements (accounting for aperture corrections) for these sources, calibrated against the PS1 (Chambers et al. 2016) catalog.

For sources whose photometry was deemed to be contaminated by host galaxy light from visual inspection (which was found to be true only for SN 2018kjy), we performed image subtraction using reference images from WaSP obtained >1 year after the peak of the transient light curve. The image subtraction was performed by first aligning the science image
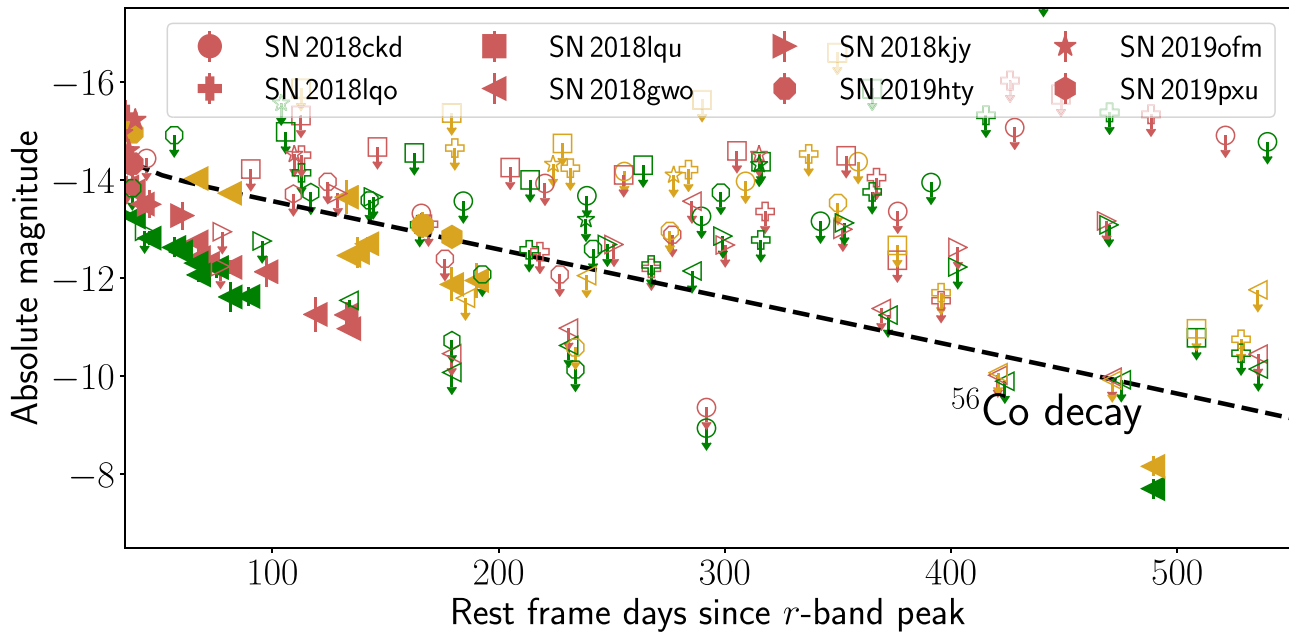
Figure 4. Late-time photometric evolution of the Ca-rich gap transients in the CLU sample, as a function of rest-frame time from the r-band peak. Each object is assigned a separate symbol for late-time detections as indicated in the legend. The colors denote individual filters: brown for the r band, light green for the g band, and gold for the i band. Upper limits are indicated as hollow symbols with arrows in the respective filter colors. The black dashed line shows the decline rate expected from the radioactive decay of ^{56}Co using an Arnett model with a ^{56}Ni mass of 0.015 $M_\odot$, under the assumption of complete trapping of γ-rays.

to the reference image by aligning the two images to the same system calibrated against Gaia DR2 (Gaia Collaboration et al. 2018). The alignment was performed by first extracting a source catalog for both the science and the reference image using `SExtractor` (Bertin 2006) followed by astrometric alignment using the `scamp` code with Gaia DR2 as the reference catalog.

The images were then resampled to the same output grid using `Swarp` (Bertin et al. 2002) and flux-scaled to a common zero-point. Image subtraction was performed using the `ZOGY` code (Zackay et al. 2016) using an input PSF model for the science and reference image using `PSFEx` (Bertin 2011). Forced PSF photometry was performed on the generated difference image to estimate the flux and flux uncertainty at the transient position, including an additional Monte Carlo simulation of the PSF-fit flux variance across the difference images to account for uncorrected correlated noise in the difference image output.

However, we caution that in several cases, the latest images from LRIS showed evidence of diffuse sources near the transient, which we were unable to subtract due to the absence of a template (ideally acquired several hundred days after the latest observation), and thus report the host-contaminated aperture photometry fluxes only. As in the case of the ZTF photometry, we report detections of sources whose S/N was higher than 3σ, and detections with 5σ upper limits. The late-time photometric evolution for the sample is shown in Figure 4. We discuss the local environments of the Ca-rich gap transients as observed in the late-time imaging in Section 4.2.

2.6. Spectroscopy

Spectroscopic follow-up of transients near peak light was obtained as a part of the regular classification effort of the CLU experiment. Typically one spectrum was obtained near peak light for initial spectroscopic classification and a sequence of nebular-phase spectra were obtained starting at least ≈ 30 days

after peak. The SEDM spectrograph was used for spectroscopy for only two of these sources (SN 2018gwo and SN 2019hty) since they were typically too faint (>19 mag) for SEDM spectroscopy. The SEDM data were reduced using the `pysedm` (Rigault et al. 2019) automatic pipeline. Peak light spectroscopy for the rest of the sample was obtained using the DBSP, and the data were reduced using the `pyraf-dbsp` pipeline (Bellm & Sesar 2016).

We obtained two epochs of spectroscopy of SN 2018gwo with the APLY200 spectrograph at Three Hills Observatory. The spectra were reduced using ISIS software.[28] The spectrum images were bias- and dark-subtracted, flat-field corrected using a tungsten halogen lamp, corrected for geometric distortions, and sky background subtracted before extracting the spectrum profile. The spectrum was wavelength-calibrated using an Ne/Ar reference lamp and calibrated in relative flux using as a reference, a hot star (HD 123299) from the MILES library of spectra[29] measured the same night at similar airmass. We obtained follow-up spectroscopy for some sources using the Alhambra Faint Object Spectrograph and Camera (ALFOSC) on the Nordic Optical Telescope (NOT). The NOT data were reduced using the `FOSCGUI` pipeline.[30]

Late-time nebular spectroscopy was obtained using LRIS on the Keck I telescope starting from ≈ 30 days after peak light. For some sources, we obtained up to four epochs of nebular-phase spectra using LRIS. The data were reduced using the automated `lpipe` pipeline. We present the complete list of spectroscopic observations in Table 3, while the spectra are presented in Figure 5. In addition, we used publicly available spectra from the TNS for SN 2018gwo and some events in the control sample (Appendix). Spectra for the literature sample of events were obtained from WISeREP (Yaron & Gal-Yam 2012) and

---

[28] By C. Buil; http://www.astrosurf.com/buil/isis-software.html.
[29] http://miles.iac.es/
[30] http://graspa.oapd.inaf.it/foscgui.html

Table 3
Log of Spectroscopic Observations of All Objects Presented in This Paper

Object	Observation Date (UTC)	MJD	Phase (days from r peak)	Telescope + Instrument	Range Å	Resolution $\lambda/\delta\lambda$
SN 2018ckd	2018-06-12	58,281.3	+3	P200 + DBSP	3500–10000	1000
SN 2018ckd	2018-06-21	58,290.2	+12	P200 + DBSP	3500–10000	1000
SN 2018ckd	2018-08-08	58,338.3	+57	Keck I + LRIS	3500–10000	1000
SN 2018ckd	2019-04-03	58,576.5	+291	Keck I + LRIS	3500–10000[†]	1000
SN 2018lqo	2018-08-21	58,351.2	−1	P200 + DBSP	3500–10000	1000
SN 2018lqo	2018-10-12	58,403.3	+49	Keck I + LRIS	3500–10000	1000
SN 2018lqu	2018-09-12	58,373.1	+2	P200 + DBSP	3500–10000	1000
SN 2018lqu	2018-10-12	58,403.2	+31	Keck I + LRIS	3500–10000	1000
SN 2018gwo	2018-09-30	58,391.8	−12	THO + ALPY	3700–7500	100
SN 2018gwo	2018-10-06	58,397.8	−6	THO + ALPY	3700–7500	100
SN 2018gwo	2018-11-06	58,428.5	+23	P60 + SEDM	3800–9200	100
SN 2018gwo	2018-12-04	58,456.6	+51	Keck I + LRIS	3500–10000	1000
SN 2018gwo	2019-03-07	58,549.5	+143	Keck I + LRIS	3500–10000	1000
SN 2018gwo	2019-06-03	58,637.3	+230	Keck I + LRIS	3500–10000	1000
SN 2018kjy	2018-12-14	58,466.3	+5	P200 + DBSP	3500–10000	1000
SN 2018kjy	2019-01-04	58,487.4	+25	Keck I + LRIS	3500–10000	1000
SN 2018kjy	2019-04-03	58,576.2	+113	Keck I + LRIS	3500–10000	1000
SN 2019hty	2019-07-01	58,665.2	+6	P200 + DBSP	3500–10000	1000
SN 2019hty	2019-07-02	58,666.2	+7	P60 + SEDM	3800–9200	100
SN 2019hty	2019-08-04	58,699.2	+40	P200 + DBSP	3500–10000	1000
SN 2019ofm	2019-08-27	58,722.3	−1	P200 + DBSP	3500–10000	1000
SN 2019ofm	2020-02-18	58,897.5	+168	Keck I + LRIS	3500–10000	1000
SN 2019pxu	2019-09-24	58,750.4	+3	P60 + SEDM	3800–9200	100
SN 2019pxu	2019-10-03	58,759.5	+11	P200 + DBSP	3500–10000	1000
SN 2019pxu	2019-10-27	58,783.5	+35	Keck I + LRIS	3500–10000	1000
SN 2019pxu	2020-02-18	58,897.3	+146	Keck I + LRIS	3500–10000	1000
SN 2018dbg	2018-08-04	58,334.0	+22	P200 + DBSP	3500–10000	1000
SN 2018fob	2018-08-21	58,351.0	−8	P200 + DBSP	3500–10000	1000
SN 2018fob	2018-08-31	58,361.0	+0	P60 + SEDM	3800–9200	100
SN 2018fob	2019-04-03	58,576.0	+209	Keck I + LRIS	3500–10000	1000
SN 2018kqr	2018-12-14	58,466.3	+1	P200 + DBSP	3500–10000	1000
SN 2018kqr	2018-12-27	58,479.2	+14	P200 + DBSP	3500–10000	1000
SN 2019yz	2019-02-20	58,534.2	+7	NOT + ALFOSC	3800–9500	300
SN 2019yz	2019-04-15	58,588.2	+61	P60 + SEDM	3800–9200	100
SN 2019yz	2019-06-08	58,642.0	+114	P60 + SEDM	3800–9200	100
SN 2019yz	2019-07-02	58,666.0	+138	P60 + SEDM	3800–9200	100
SN 2019yz	2019-09-26	58,752.2	+224	Keck I + LRIS	3500–10000	1000
SN 2019abb	2019-01-26	58,509.2	−4	P200 + DBSP	3500–10000	1000
SN 2019abb	2019-02-09	58,523.0	+9	P60 + SEDM	3800–9200	100
SN 2019abb	2019-02-10	58,524.9	+11	NOT + ALFOSC	3800–9500	300
SN 2019abb	2019-04-06	58,579.2	+64	Keck I + LRIS	3500–10000	1000
SN 2019abb	2020-01-24	58,872.0	+353	Keck I + LRIS	3500–10000	1000
SN 2019ape	2019-02-12	58,526.4	−13	P200 + DBSP	3500–10000	1000
SN 2019ape	2019-03-01	58,543.1	+2	NOT + ALFOSC	3800–9500	300
SN 2019ape	2019-12-03	58,820.0	+274	Keck I + LRIS	3500–10000	1000
SN 2019ccm	2019-04-06	58,579.2	+6	Keck I + LRIS	3500–10000	1000
SN 2019ccm	2019-09-28	58,754.0	+178	Keck I + LRIS	3500–10000	1000
SN 2019txl	2019-04-06	58,579.0	+11	Keck I + LRIS	3500–10000	1000
SN 2019txl	2020-02-18	58,897.0	+318	Keck I + LRIS	3500–10000	1000
SN 2019txr	2019-06-04	58,638.0	+28	Keck I + LRIS	3500–10000	1000
SN 2019txr	2020-02-18	58,897.0	+276	Keck I + LRIS	3500–10000	1000
SN 2019txt	2019-05-13	58,616.0	+10	P200 + DBSP	3500–10000	1000
SN 2019txt	2019-06-04	58,638.0	+31	Keck I + LRIS	3500–10000	1000
SN 2019txt	2020-01-24	58,872.0	+259	Keck I + LRIS	3500–10000	1000
SN 2019gau	2019-06-04	58,638.9	−4	P60 + SEDM	3500–10000	100
SN 2019gau	2020-02-18	58,897.0	+260	Keck I + LRIS	3500–10000	1000
SN 2019gsc	2019-06-04	58,638.2	−2	P200 + DBSP	3500–10000	1000
SN 2019gsc	2019-07-04	58,668.0	+27	Keck I + LRIS	3500–10000	1000
SN 2019ttf	2019-07-04	58,668.0	+10	Keck I + LRIS	3500–10000	1000
SN 2019ttf	2020-03-22	58,930.0	+269	Keck I + LRIS	3500–10000	1000
SN 2019mjo	2019-08-01	58,696.0	+7	P200 + DBSP	3500–10000	1000
SN 2019mjo	2020-01-24	58,872.0	+176	Keck I + LRIS	3500–10000	1000

Object	Observation Date (UTC)	MJD	Phase (days from r peak)	Telescope + Instrument	Range Å	Resolution $\lambda/\delta\lambda$
SN 2019ouq	2019-08-04	58,699.3	+6	P200 + DBSP	3500–10000	1000
SN 2019ouq	2020-01-24	58,872.0	+173	Keck I + LRIS	3500–10000	1000

Note. † denotes spectra that do not have high enough S/N to detect features.

attributed to the original source where relevant. All data presented in this paper will be publicly released on WISeREP and as an electronic supplement upon publication.

3. Analysis of the Combined Sample

Here, we present a combined analysis of the spectroscopic and photometric properties of the sample of Ca-rich gap transients presented in this paper and those of the literature sample of events that satisfy our selection criteria. We begin with a qualitative analysis of the spectroscopic properties, particularly to highlight the existence of a continuum of spectroscopic characteristics in the full sample of events. We outline the procedures used for a quantitative analysis of the full sample of events, and present quantitative results on the photometric and spectroscopic properties of the sample to highlight trends across the continuum of spectroscopic properties. We use these results to discuss implications for the progenitor channels in Section 6.

3.1. Photospheric-phase Spectra

Since we aim to characterize the peak light spectral diversity in this section, we discuss objects for which a medium-resolution spectrum was available within ≈10 days of peak light—16 of the total sample of 18 objects[31] have photospheric-phase spectra acquired near the peak of the light curve. The photospheric-phase spectra of this sample are diverse, and most notably separate into SN Ib/c–like (absence of a strong Si II line, with a continuum of He I line strengths) and SN Ia–like (with strong Si II lines) objects. This distinction is a natural parallel to the traditional classification scheme invoked for the broader population of hydrogen-poor SNe (Filippenko 1997; Gal-Yam 2017). We thus proceed by defining two spectroscopic classes within the sample of Ca-rich gap transients based on their similarity to either SNe Ib/c or SNe Ia near peak light and refer to them as Ca-Ib/c and Ca-Ia objects. Within the photometric selection criteria defined in this experiment, the relative occurrence rate of the Ca-Ib/c to the Ca-Ia objects is 6:1, although a true-rate estimate would require incorporating the luminosity functions of the two classes (see Section 5).

3.1.1. The Ca-Ib/c Class

In Figure 6, we plot the photospheric-phase spectra of the Ca-Ib/c objects. Prominent spectral lines detected in the photospheric phase are marked, along with three optical lines of He I and their P-Cygni absorption regions due to the known similarity of these objects to SNe Ib at peak (Perets et al. 2010). The ZTF sample of events is dominated by Type Ib–like spectra near peak light (exhibiting He I λ5876, λ6678, and

λ7065) in the photospheric-phase spectra albeit with a range of line strengths and velocities. The He I λ6678 line is usually contaminated by the nearby Si II λλ6347, 6371 lines (Sullivan et al. 2011; Kasliwal et al. 2012; De et al. 2018a). Other common features in the peak light spectra include P-Cygni features of O I λ7774 and Ca II H&K and the NIR triplet. SN 2012hn is the only object that does not show any evidence of He I in its peak spectrum (Valenti et al. 2014). We also do not conclusively identify He I in the peak light spectrum of SN 2018gwo. We thus tentatively classify SN 2018gwo as a Ca-Ic although the low S/N and resolution of the peak spectrum preclude a definite classification.

Upon closer inspection, the set of peak light spectra shown in Figure 6 is demarcated into two groups of events—one with events characterized by flat continua across the entire spectral range and one with events characterized by strong suppression of flux at bluer wavelengths and red continua. We indicate these two classes of events with different colors (dark green and red) in Figure 6, and throughout the rest of this manuscript. The spectra of events in the first class are relatively homogeneous, and show clear evidence of strong He I at normal photospheric velocities (≈8000–11,000 km s^{-1}; see Section 3.1.3). Notably, these objects exhibit a strong continuum in the blue side of the spectrum (below 5500 Å) and clear absorption features of Ca II, Mg I and Fe II superimposed on the blue-side continuum.

On the other hand, events in the latter group show strong suppression of the continuum flux in the blue side of the spectrum (below 5500 Å) producing a spectrum with redder colors. These exhibit a diverse range of line velocities, ranging from events with normal photospheric velocities (SN 2019pxu) to peculiar low-velocity (≈4000–6000 km s^{-1}) events such as PTF 12bho and SN 2018kjy. Absorption features of metals blueward of 5500 Å (Ca II, Mg I, and Fe II) are only weakly detected due to the strong suppression of flux in this region. Notably, SN 2012hn and SN 2018gwo in this group do not show evidence of He I (and hence would be Ca-Ic objects nominally), while SN 2018kjy exhibits only weak signatures of low-velocity He I in its spectrum. Given the small number of events, it is unclear whether there is a continuum of events between these two types of objects. We proceed by referring to the two classes of objects as objects with green and red continua respectively, and use the same color scheme as in Figure 6.

There is considerable diversity in the presence and strength of He lines in the peak light spectra of the Ca-Ib/c objects. The identification of He is a crucial aspect for understanding the progenitors of these explosions since the presence of He in the ejecta is indicative of an He-rich progenitor system. However, He lines visible in the optical region are non-thermally excited (Dessart et al. 2012; Hachinger et al. 2012) and hence their absence does not necessarily preclude the presence of He in the ejecta. The detection of He lines is dependent on the amount of

---

[31] SN 2007ke and PTF 11bij are the only objects that do not have a peak light spectrum.
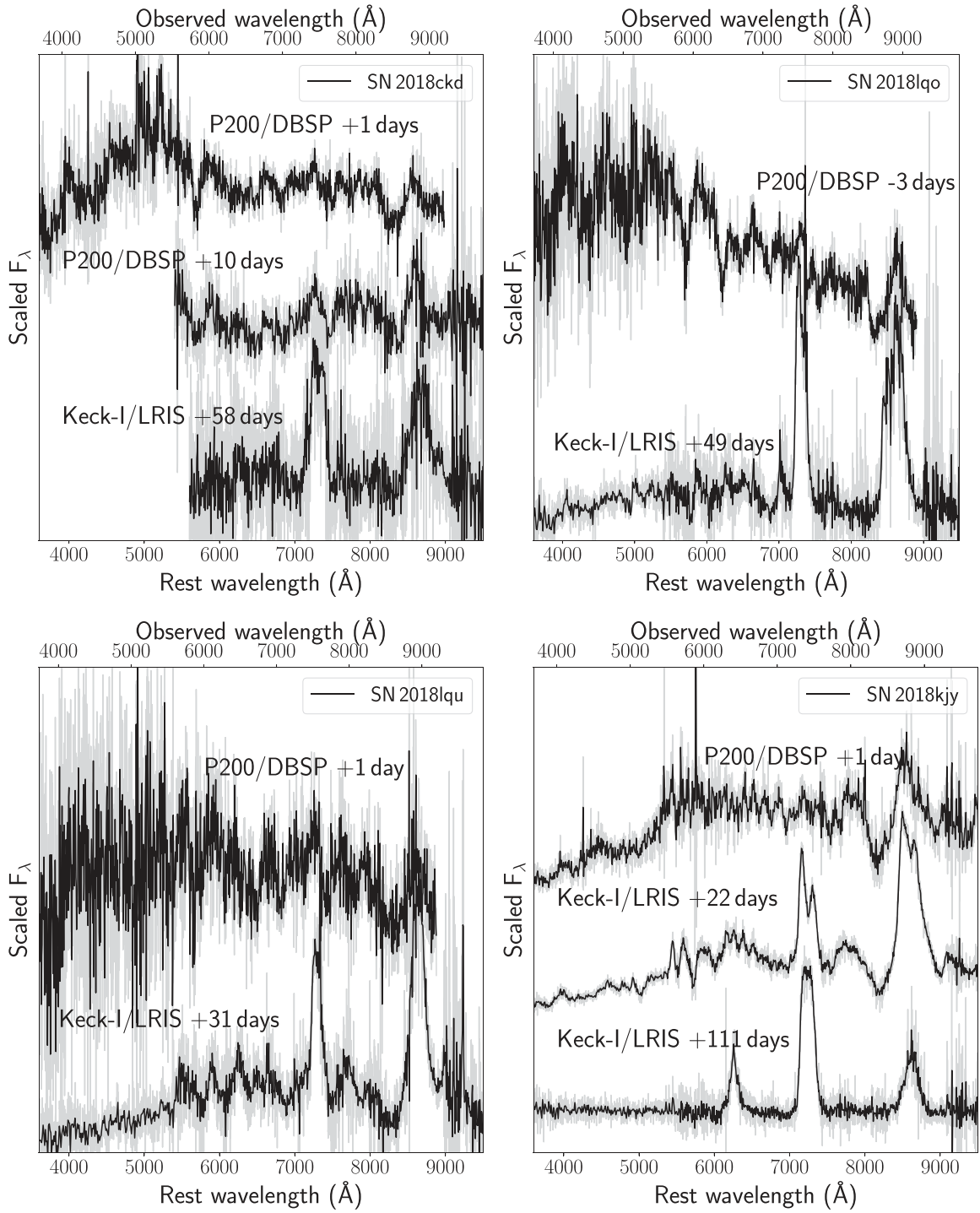
Figure 5. Spectroscopic sequence of the sample of Ca-rich gap transients presented in this paper. In each panel, the object name is indicated in the legend and the phase of the spectrum is denoted next to each spectrum with respect to the peak of the *r*-band light curve. The gray lines show the unbinned spectra while the black lines show the same spectra binned to improve the S/N.

(The data used to create this figure are available.)

[56]Ni mixing in the ejecta, since [56]Ni is able to excite He I transitions non-thermally. Thus, the presence of He lines also constrain the radioactive mixing in the ejecta. While most of the Ca-Ib/c objects exhibit prominent and unambiguous He I lines in the optical, similar to the prototype event SN 2005E, these lines are difficult to unambiguously identify in peculiar events.

In Figure 7, we show zoomed-in regions of the peak light spectra of the sample around the optical He I lines at 5876 Å, 6678 Å and 7065 Å. The identification of He is complicated by the contamination of the He I 5876 Å line with the nearby Na I line seen in SNe Ic, thus requiring the detection of multiple He I lines at similar velocities to conclusively confirm the presence of He. This necessitates a careful examination of the features
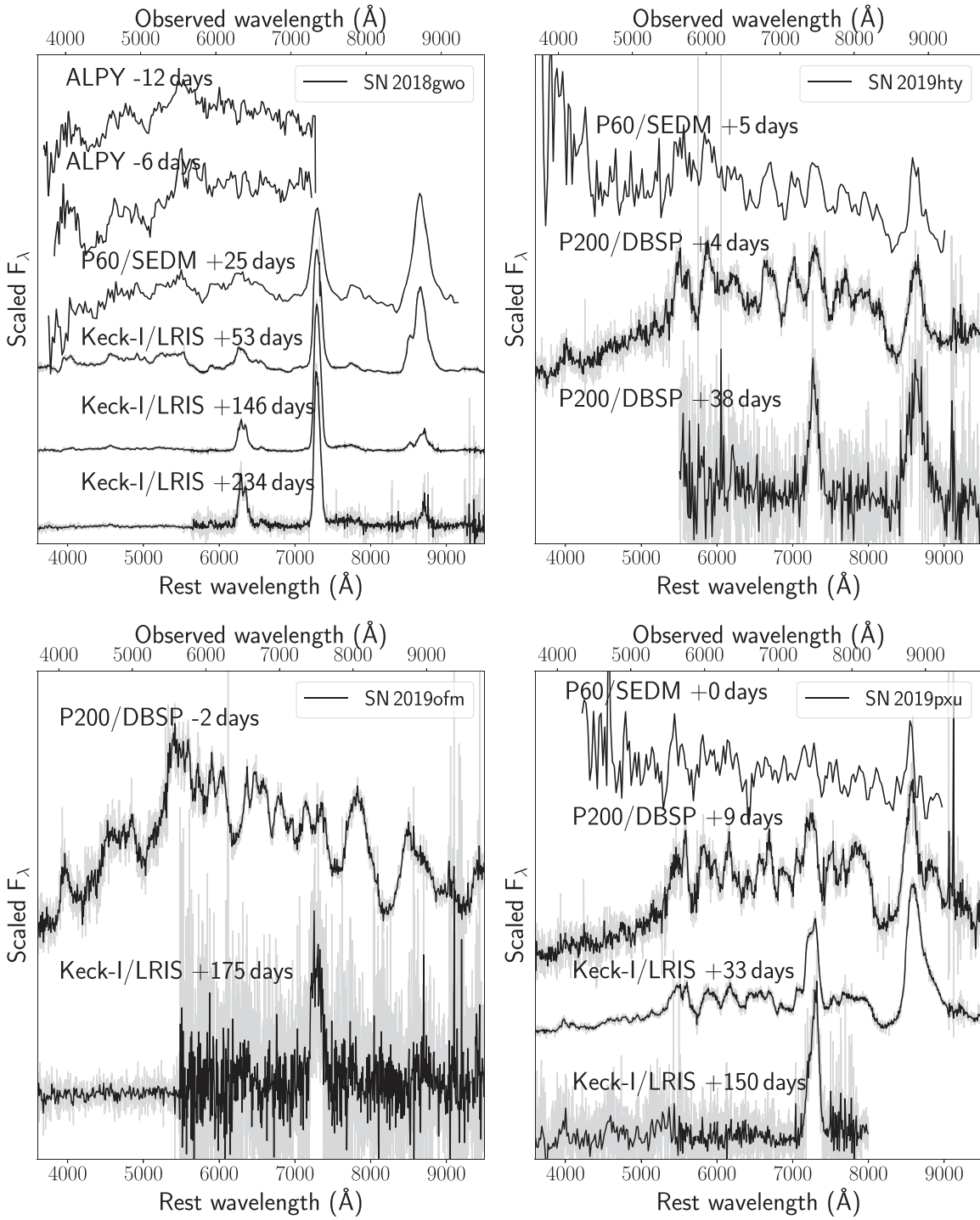
Figure 5. (Continued.)

around the other optical He I lines at 6678 Å and 7065 Å. We note that all the green Ca-Ib/c events exhibit unambiguous evidence of He I at similar velocities at all the optical transitions.

However, the family of events with red continua exhibit much more diverse properties around the He I transitions, which include peculiar events like SN 2012hn, PTF 12bho and SN 2018kjy. Only SN 2019hty exhibits unambiguous P-Cygni absorption in all the He I lines and thus He can be confirmed. In the progression from SN 2019pxu to SN 2012hn, we see a gradual change in the strength and absorption depth of the He

lines. Specifically, we note the appearance of an emission feature at the expected absorption position of the He I $\lambda7065$ line that gets stronger from SN 2019pxu to SN 2012hn. This emission feature has been attributed to C II in the spectral modeling of SN 2012hn, although it could also be associated with Al II (Kasliwal et al. 2010; Sullivan et al. 2011; De et al. 2018a). In the same sequence of objects the He I $\lambda7065$ line gets progressively weaker until it is not detected at all in SN 2012hn. The same trend is also detected in the He I $\lambda6678$ line although the identification of He I $\lambda6678$ in SN 2012hn is
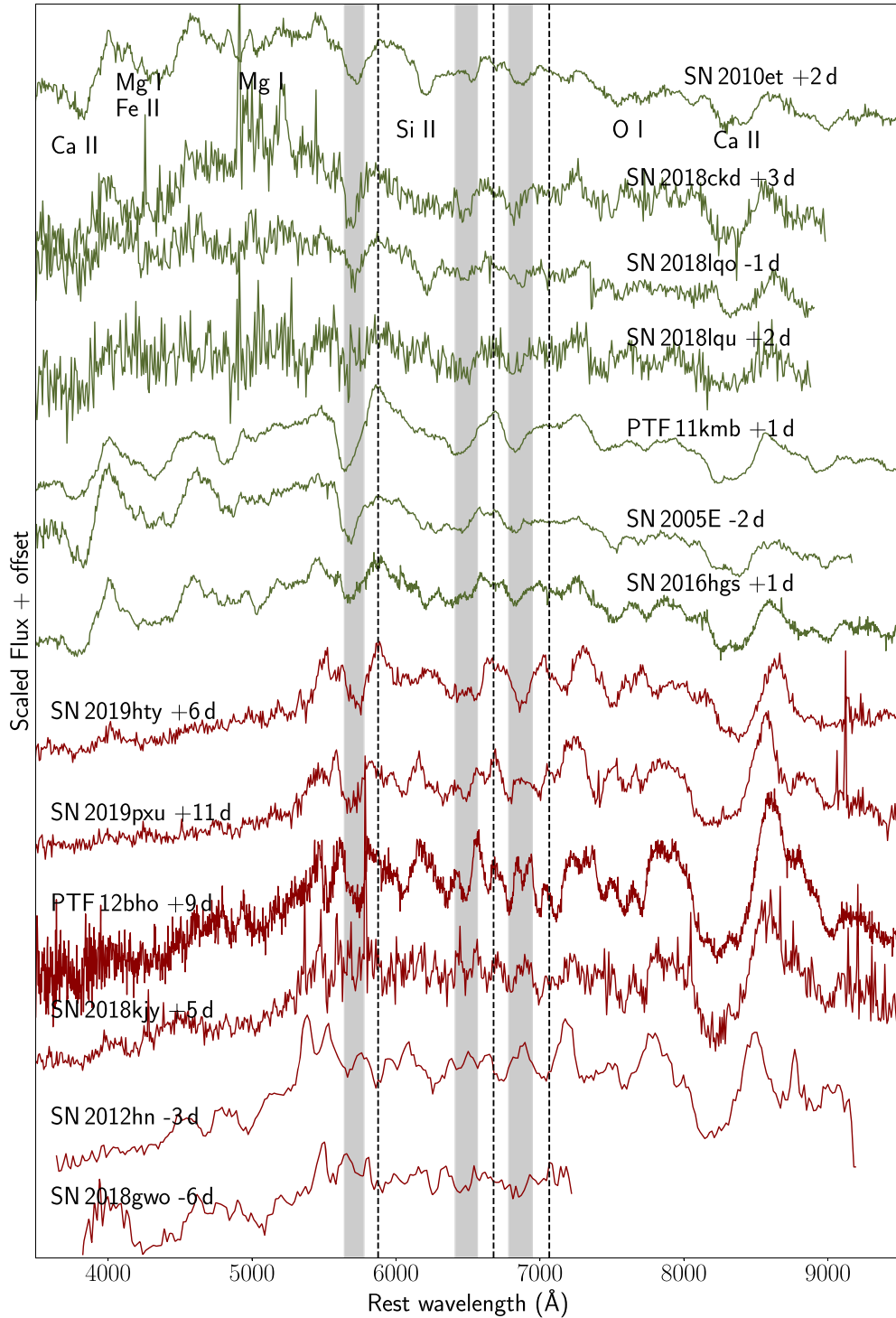
Figure 6. Photospheric-phase spectra of Ca-rich gap transients that exhibit SN Ib/c–like features (termed Ca-Ib/c objects) in the ZTF sample combined with the same for events in the literature. The transient name and phase of the spectrum are indicated next to each spectrum. The spectrum color separates the two primary spectral types in the sample based on the shape of the continuum—the events plotted in green have peak spectra characterized by flat or green continua, while spectra in red show events that exhibit strong suppression of flux at bluer wavelengths thus exhibiting red continua. The dashed lines show the rest-frame wavelengths of three optical He I lines, while the shaded bars show the expected P-Cygni absorption minima for velocities ranging from 5000 to 12,000 km s^{-1}.

complicated by the presence of the nearby Si II line. SN 2012hn does not show any evidence of He either in its optical or in its NIR spectra (Valenti et al. 2014). We thus find evidence of a continuum of He line strengths in these events, which range from events with strong He lines to those with very weak or absent He lines.

3.1.2. The Ca-Ia Class

Figure 8 shows a comparison of the photospheric- and nebular-phase spectra of the three Ca-Ia objects in the sample, indicated by orange markers throughout this manuscript. These objects exhibit the typical features of 1991bg-like objects defined by a strong Ti II trough in the blue side of the spectrum.
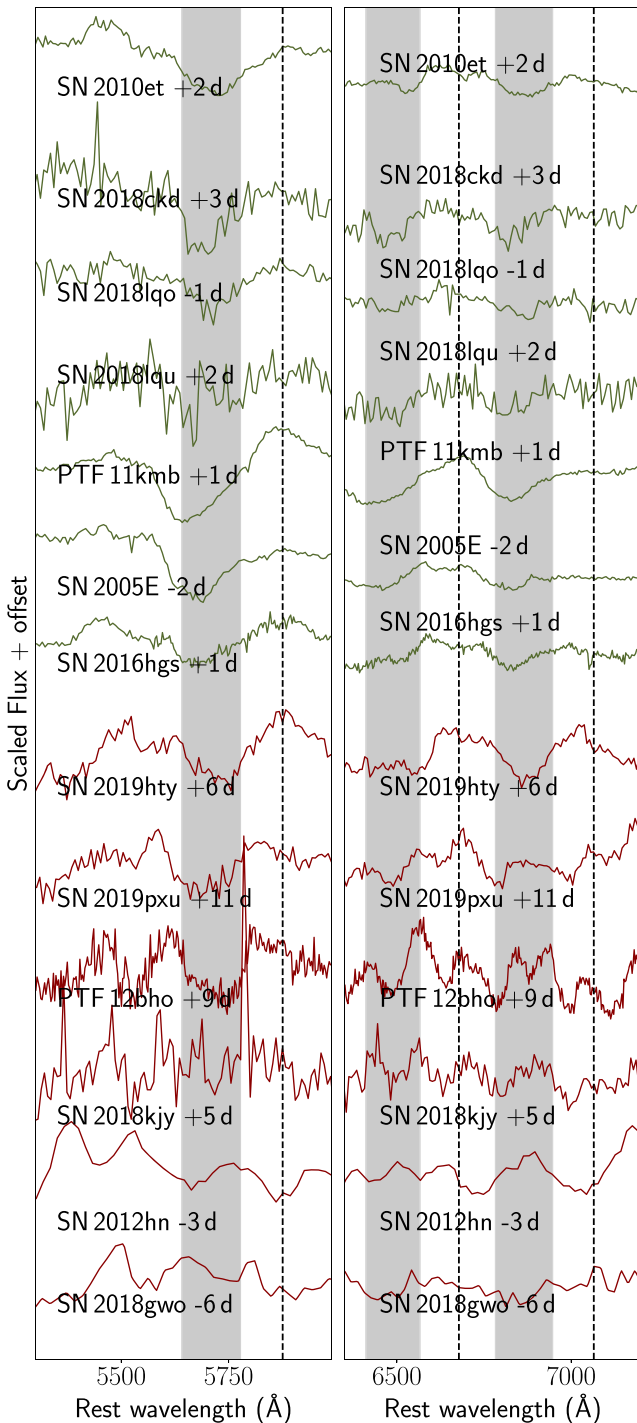
Figure 7. Zoomed-in plots of the photospheric-phase spectra of the Ca-Ib/c objects around the expected positions of He I transitions. The left panel shows the region around the He I λ5876 line and the right panel shows the region including the He I λ6678 and λ7065 lines. The color coding of the spectra is the same as that in Figure 6. The black dashed lines show the rest-frame positions of the He I lines, while the gray shaded regions show the absorption region for the velocity range of 5000–12,000 km s^{-1}.

In addition, all of these objects exhibit mild to strong line blanketing features shortward of 5000 Å in the blue side of the spectrum. Such features are typically indicative of the outer ejecta being rich in Fe-group material that efficiently absorbs the blue flux (Nugent et al. 1997; Polin et al. 2019a). We note that SN 2019ofm exhibits several similarities to the peak light

spectrum of SN 2016hnk (although with lower line velocities), while PTF 09dav exhibits some different features and line strengths, some of which were attributed to rare elements like Sc II and Sr II in Sullivan et al. (2011). Although the peak light spectra are broadly similar, such exotic elements were not required in the spectral modeling of SN 2016hnk in Galbany et al. (2019) and Jacobson-Galán et al. (2020), and hence are unlikely for SN 2019ofm given the spectral similarity between the two objects.

Given the lack of prominent He lines in both the Ca-Ic objects and Ca-Ia objects, it is instructive to compare the peak light spectra of the two classes. In Figure 9, we plot the peak light spectrum of SN 2012hn—the only unambiguous Ca-Ic object in the sample—along with the peak light spectra of two Ca-Ia objects, SN 2019ofm and SN 2016hnk. It is worth noting the striking resemblance between the spectra of SN 2012hn and SN 2019ofm, barring the weaker strength of the Si II line in SN 2012hn (which leads to its Ca-Ic classification). Specifically, we find that although the velocities are different in the three objects, they show similar features over the entire optical spectrum. The only discrepancies are in the bluer part of the spectrum where the Ca-Ia objects show features from Fe-group elements (near ≈4000 Å). SN 2016hnk exhibits a very strong Si II line similar to normal/subluminous SNe Ia (Gal-Yam 2017), while SN 2019ofm exhibits a weaker Si II line but with all the characteristic SN Ia features, and SN 2012hn exhibits the weakest Si II line and nearly the same spectral features as SN 2019ofm.

Sun & Gal-Yam (2017) demonstrated that SN I subtypes (Ia/Ib/Ic) occupy different loci on the line depth diagram of Si II λ6150 Å and O I λ7774 Å measured in peak-brightness spectra (see their Figure 9). In order to quantitatively investigate the striking similarities between the Ca-Ia and Ca-Ic objects, we performed these measurements in a manner similar to that of Sun & Gal-Yam (2017). SN 2016hnk exhibits a λ6150 line depth of ≈0.6 and a depth ratio of λ6150/λ7774 ≈ 0.75, similar to 91bg-like SNe Ia in the Sun & Gal-Yam (2017) sample. However, we find that SN 2019ofm exhibits a λ6150 line depth of ≈0.35 and a depth ratio of λ6150/λ7774 ≈ 0.83 and is exactly at the SN Ia–SN Ic classification boundary suggested in that work.

Similarly, the peak spectrum of SN 2012hn exhibits a λ6150 depth of ≈0.3 and a depth ratio of λ6150/λ7774 ≈ 1.0, which falls exactly on the classification boundary for SNe Ib/c in that sample. In particular, we note that SN 2019ofm and SN 2012hn occupy an empty phase space in the classification diagram of Sun & Gal-Yam (2017)—with SN 2019ofm being a transitional Ia–Ic object and SN 2012hn being a transitional Ib–Ic object. We thus conclude that there may be a continuum of events from Ca-Ia to Ca-Ic to Ca-Ib objects based on their peak light photospheric spectral properties. We discuss this sequence together with the photometric- and nebular-phase properties in Section 6.

3.1.3. Photospheric Velocities

For a quantitative comparison of the spectral features, we performed fits of the most prominent spectroscopic features of the combined sample of events, and list the derived parameters in Table 4. The aim of this exercise is to elucidate the photospheric velocity evolution of the most prominent spectral lines in these transients as they hold clues to the density structure of the ejecta and internal emission powering
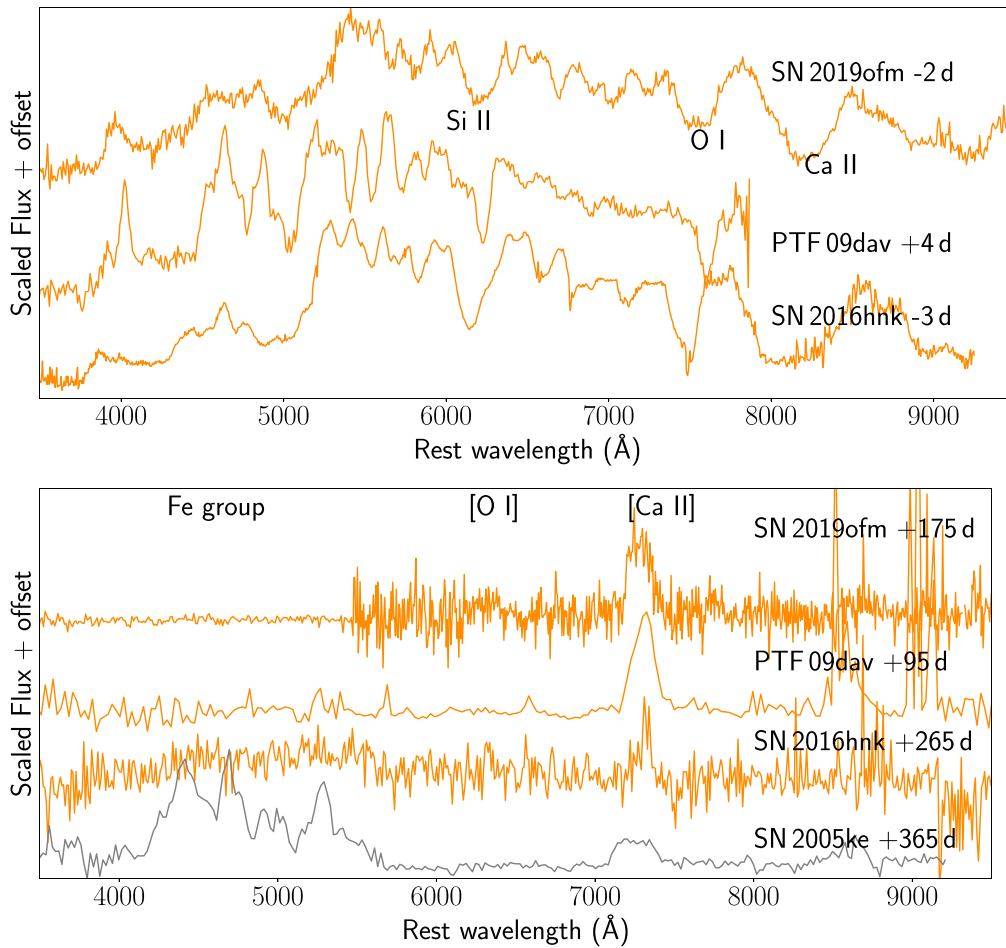
Figure 8. Photospheric-phase (top panel) and nebular-phase (bottom panel) spectra of Ca-rich gap transients that exhibit SN Ia–like features (termed Ca-Ia objects) in the ZTF sample combined with the same for events in the literature. The transient name and phase of the spectrum are indicated next to each spectrum. The prominent photospheric lines of Si II, O I, and Ca II are marked in the peak light spectra plot while the nebular lines of [O I], [Ca II], and Fe-group elements are marked in the lower panel. In the lower panel, we also show a nebular-phase spectrum of the SN 1991bg–like event SN 2005ke to highlight the differences between 1991bg-like objects and Ca-rich objects in terms of the absence of Fe-group features in the blue part of the spectrum.
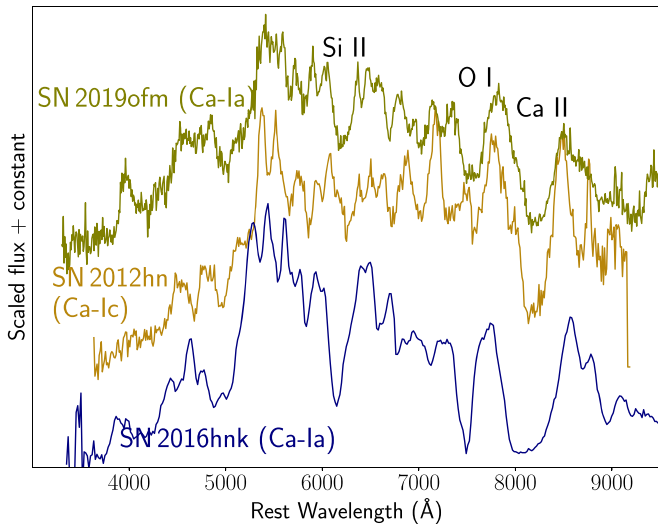
Figure 9. Comparison of the peak light optical spectra of He-poor Ca-Ib/c event SN 2012hn and the two Ca-Ia events SN 2016hnk and SN 2019ofm. The prominent spectral features of Si II, O I, and Ca II are marked.

mechanism (Piro & Nakar 2014; Sell et al. 2015). These velocity estimates are also necessary for quantitative estimates of the explosion kinetics (Arnett 1982; Arnett et al. 1985). We

follow procedures similar to those used in Liu et al. (2016) and Fremling et al. (2018) for normal stripped-envelope SNe. He I is the most common spectral feature near peak light in the sample of Ca-Ib/c events, and hence we estimate the velocity of the He I λ5876 line by fitting a low-order polynomial to the flux around the line. We estimate the uncertainties in the velocity by Monte Carlo sampling of the flux in the relevant wavelength region.

We estimate the flux uncertainty by subtracting the smooth polynomial fit from the spectral data and compute the noise rms as the standard deviation of the flux from the smoothed spectrum. We then add a Gaussian distribution of noise to the spectrum using the wavelength-dependent flux rms as the standard deviation, and compute the spectral fit parameters for the several realizations of the input spectrum. While O I λ7774 is also detected in most of the peak light spectra, we do not fit the absorption in this line since it appears to be uniformly contaminated by another nearby absorption feature (likely Mg II; e.g., Valenti et al. 2014; De et al. 2018a). We perform the same fitting for the He I λ7065 line in the spectra where it is detected in the Ca-Ib/c events, while the same is computed for the Si II λ6355 line in the case of the Ca-Ia events.

The velocity estimates from fitting He I λ5876 and λ7065 are largely consistent in the Ca-Ib/c events. However, the velocities and detection of He in the red events are complicated

Table 4
Spectral Fit Parameters for the Sample of Ca-rich Gap Transients Presented in This Paper, together with the Fits for the Literature Sample of Ca-rich Gap Transients

Object	Phase (days)	V_1 (km s^{-1})	V_2 (km s^{-1})	[Ca II]/[O I]	References
SN 2018ckd	+1	9660 ± 110 (λ5876)	10090 ± 140 (λ7065)	⋯	This work
SN 2018ckd	+10	8260 ± 650 (λ5876)	⋯	⋯	This work
SN 2018ckd	+58	⋯	⋯	>3.38	This work
SN 2018lqo	−2	8230 ± 150 (λ5876)	8270 ± 100 (λ7065)	⋯	This work
SN 2018lqo	+49	5090 ± 310 (λ5876)	⋯	>12.51	This work
SN 2018lqu	+1	11100 ± 410 (λ5876)	10550 ± 280 (λ7065)	⋯	This work
SN 2018lqu	+31	5720 ± 500 (λ5876)	...*	>8.38	This work
SN 2018gwo	+23	5150 ± 570 (λ5876)	⋯	⋯	This work
SN 2018gwo	+53	4780 ± 100 (λ5876)	6660 ± 80 (λ7065)	5.16 ± 0.08	This work
SN 2018gwo	+146	⋯	⋯	3.98 ± 0.06	This work
SN 2018gwo	+243	⋯	⋯	2.70 ± 0.08	This work
SN 2018kjy	+1	...*	2470 ± 170 (λ7065)	⋯	This work
SN 2018kjy	+22	6610 ± 90 (λ5876)	⋯	⋯	This work
SN 2018kjy	+111	⋯	⋯	4.44 ± 0.24	This work
SN 2019hty	+4	7480 ± 120 (λ5876)	8200 ± 50 (λ7065)	⋯	This work
SN 2019hty	+5	8200 ± 1140 (λ5876)	7600 ± 350 (λ7065)	⋯	This work
SN 2019hty	+38	⋯	⋯	>3.27	This work
SN 2019ofm	−2	⋯	7380 ± 230	⋯	This work
SN 2019ofm	+168	⋯	⋯	>2.15	This work
SN 2019pxu	+0	10310 ± 430 (λ5876)	...*	⋯	This work
SN 2019pxu	+8	9320 ± 100 (λ5876)	3110 ± 80 (λ7065)	⋯	This work
SN 2019pxu	+32	7790 ± 90 (λ5876)	3650 ± 180 (λ7065)	⋯	This work
SN 2019pxu	+146	⋯	⋯	>8.30	This work
SN 2005E	−2	10200 ± 200 (λ5876)	9800 ± 80 (λ7065)	⋯	[1]
SN 2005E	−1	10260 ± 60 (λ5876)	9960 ± 60 (λ7065)	⋯	[1]
SN 2005E	+20	4450 ± 230 (λ5876)	4980 ± 60 (λ7065)	⋯	[1]
SN 2005E	+53	4430 ± 80 (λ5876)	4540 ± 150 (λ7065)	8.39 ± 0.26	[1]
SN 2007ke	+20	4370 ± 100 (λ5876)	4210 ± 310 (λ7065)	⋯	[1]
PTF 09dav	+2	⋯	6140 ± 100 (λ6355)	⋯	[2]
PTF 09dav	+8	⋯	5070 ± 70 (λ6355)	⋯	[2]
PTF 09dav	+13	⋯	5070 ± 120 (λ6355)	⋯	[2]
PTF 09dav	+88	⋯	⋯	>22.35	[2]
SN 2010et	+2	8210 ± 70 (λ5876)	8880 ± 60 (λ7065)	⋯	[3]
SN 2010et	+27	7340 ± 110 (λ5876)	7990 ± 120 (λ7065)	⋯	[3]
SN 2010et	+62	3620 ± 440 (λ5876)	7080 ± 360 (λ7065)	⋯	[3]
SN 2010et	+87	⋯	⋯	6.15 ± 0.51	[3]
SN 2010et	+115	⋯	⋯	6.14 ± 1.36	[3]
PTF 11bij	+45	⋯	⋯	>7.06	[3]
SN 2012hn	−3	7230 ± 320 (λ5800)	⋯	⋯	[4]
SN 2012hn	+4	7400 ± 160 (λ5800)	⋯	⋯	[4]
SN 2012hn	+6	7490 ± 70 (λ5800)	⋯	⋯	[4]
SN 2012hn	+13	6740 ± 220 (λ5800)	⋯	⋯	[4]
SN 2012hn	+25	5200 ± 40 (λ5800)	⋯	⋯	[4]
SN 2012hn	+150	⋯	⋯	2.25 ± 0.05	[4]
PTF 11kmb	+1	11670 ± 50 (λ5876)	9910 ± 40 (λ7065)	⋯	[5]
PTF 11kmb	+24	8520 ± 170 (λ5876)	7320 ± 260 (λ7065)	⋯	[5]
PTF 11kmb	+89	⋯	⋯	8.97 ± 0.30	[5]
PTF 11kmb	+124	⋯	⋯	10.07 ± 0.70	[5]
PTF 12bho	+9	7210 ± 170 (λ5876)	3010 ± 50 (λ7065)	⋯	[5]
PTF 12bho	+17	7520 ± 250 (λ5876)	3520 ± 300 (λ7065)	⋯	[5]
PTF 12bho	+51	⋯	⋯	12.10 ± 0.66 (λ5876)	[5]
PTF 12bho	+129	⋯	⋯	>9.57	[5]
SN 2016hgs	−8	15010 ± 200 (λ5876)	11120 ± 310 (λ7065)	⋯	[6]
SN 2016hgs	−4	12880 ± 110 (λ5876)	10610 ± 400 (λ7065)	⋯	[6]
SN 2016hgs	+1	10750 ± 100 (λ5876)	10200 ± 90 (λ7065)	⋯	[6]
SN 2016hgs	+28	⋯	⋯	>4.80	[6]
SN 2016hgs	+59	⋯	⋯	11.52 ± 4.37	[6]
SN 2016hnk	−3	⋯	10350 ± 60 (λ6355)	⋯	[7]
SN 2016hnk	−2	⋯	10020 ± 30 (λ6355)	⋯	[7]
SN 2016hnk	−1	⋯	9740 ± 20 (λ6355)	⋯	[7]
SN 2016hnk	+0	⋯	9690 ± 40 (λ6355)	⋯	[7]
SN 2016hnk	+1	⋯	9610 ± 90 (λ6355)	⋯	[7]
SN 2016hnk	+1	⋯	9720 ± 90 (λ6355)	⋯	[7]

Table 4
(Continued)

Object	Phase (days)	V_1 (km s^{-1})	V_2 (km s^{-1})	[Ca II]/[O I]	References
SN 2016hnk	+1	⋯	9850 ± 130 (λ6355)	⋯	[7]
SN 2016hnk	+3	⋯	9060 ± 70 (λ6355)	⋯	[7]
SN 2016hnk	+4	⋯	8760 ± 50 (λ6355)	⋯	[7]
SN 2016hnk	+6	⋯	8590 ± 40 (λ6355)	⋯	[7]
SN 2016hnk	+6	⋯	8200 ± 160 (λ6355)	⋯	[7]
SN 2016hnk	+8	⋯	8440 ± 760 (λ6355)	⋯	[7]
SN 2016hnk	+10	⋯	7970 ± 110 (λ6355)	⋯	[7]
SN 2016hnk	+16	⋯	6820 ± 70 (λ6355)	⋯	[7]
SN 2016hnk	+26	⋯	6250 ± 140 (λ6355)	⋯	[7]
SN 2016hnk	+31	⋯	5880 ± 80 (λ6355)	⋯	[7]
SN 2016hnk	+32	⋯	5760 ± 210 (λ6355)	⋯	[7]
SN 2016hnk	+35	⋯	5610 ± 90 (λ6355)	⋯	[7]
SN 2016hnk	+47	⋯	5080 ± 110 (λ6355)	⋯	[7]
SN 2016hnk	+265	⋯	⋯	>4.07	[8]

Note. For each spectrum, we measured both the He I λ5876 and λ7065 velocity (if detected) for the Ca-Ib/c events, and only the Si II λ6355 velocity for the Ca-Ia events. We indicate the line measured in brackets next to the velocity measurements for each spectrum phase. Values denoted by * indicate epochs where the S/N of the spectrum was not high enough in the region of interest to measure the specific parameter. The velocity for SN 2012hn was measured using the feature near 5800 Å at peak light since it did not exhibit He signatures. For phases where the spectrum exhibited nebular emission features, we report the measured [Ca II]/[O I] ratio or lower limits when [O I] was not detected (see text). Archival spectra were obtained from the Weizmann Interactive Supernova Data Repository (WISeREP; Yaron & Gal-Yam 2012). The data were originally published in [1] Perets et al. (2010), [2] Sullivan et al. (2011), [3] Kasliwal et al. (2012), [4] Valenti et al. (2014), [5] Lunnan et al. (2017), [6] De et al. (2018a), [7] Galbany et al. (2019), and [8] Jacobson-Galán et al. (2020).

(This table is available in its entirety in machine-readable form.)

by several factors. While SN 2019hty shows an unambiguous presence of both of the He I lines we measure, the λ7065 line absorption in the other objects is contaminated by emission from a nearby blueward feature (see Figure 7), which could be associated with C II (Valenti et al. 2014) or Al II (Kasliwal et al. 2012; De et al. 2018a). Thus, the He I velocities are discrepant between the two lines for these objects. However, we report all these measurements for completeness.

SN 2012hn does not show clear signs of He I in its peak light spectra, and hence we compute the velocity for the nearby 5800 Å feature (suggested to be due to Na I or Cr II in Valenti et al. 2014) assuming that the peak of the feature near maximum light corresponds to the rest wavelength of the line. The low S/N and resolution of the spectrum of SN 2018gwo do not allow us to conclusively identify He I, and hence we do not measure the corresponding velocity for this object. SN 2018kjy exhibits a peculiar peak light spectrum with a large number of low-velocity ($\sim$2500 km s^{-1}) lines. While He I λ7065 is identifiable in the peak light spectrum, we caution that due to the large number of low-velocity lines, we only tentatively identify He I λ5876 in the peak light spectrum.

In Figure 10, we plot the evolution of the prominent photospheric-phase He I λ5876 and λ7065 (for the Ca-Ib/c events) and Si II λ6355 line (for the Ca-Ia events) velocities as a function of phase from the r-band peak. For comparison, we also plot the evolution of the He I line velocities observed in the sample of normal SNe Ib presented in Liu et al. (2016). The He I λ7065 velocity in most of the red events is much lower than that in the events with green continua. As stated in Section 3.1.3, this discrepancy is due to the blending of a nearby emission feature blueward of λ7065 that contaminates the velocity measurement, thus making the velocity evolution uncertain. SN 2018kjy stands out as a peculiar low-velocity event as evident from the large number of narrow lines visible in its peak light spectrum (see Figure 5), exhibiting several similarities to the low-velocity

spectrum observed in PTF 12bho. SN 2012hn does not exhibit signatures of He I in its peak light spectrum and hence we show the velocity evolution of the nearby 5800 Å feature, likely associated with Na I.

It is worth noting that the Si II λ6355 velocities in the Ca-Ia events vary—both PTF 09dav and SN 2019ofm exhibit lower (by $\approx$3000 km s^{-1}) velocities than SN 2016hnk at peak ($\approx$11,000 km s^{-1}). The combined sample of photospheric-phase velocities shows a consistent trend of decreasing velocities with time, consistent with a receding photosphere (in mass coordinates) in the SN ejecta. Comparing this to the normal Type Ib events in the comparison sample, we find that while the photospheric velocities are similar near peak light, the Ca-rich gap transients exhibit a much faster drop to low photospheric velocities around $\approx$20 days after peak light. A faster drop in photospheric-phase velocities suggests that the photospheric line-forming regions recede into the inner and slower layers of the ejecta faster than normal SNe Ib, consistent with the lower ejecta masses and faster transition to the optically thin nebular phase observed in these events.

3.2. Nebular-phase Spectra

3.2.1. The Ca-Ib/c Class

In Figure 11, we show a comparison of the nebular-phase spectra of the Ca-Ib/c class of objects. Despite the diversity in photospheric-phase colors and velocities, the nebular-phase spectra are relatively homogeneous, and are dominated by strong [Ca II] emission and weak [O I] emission (if [O I] is detected at all). The low-velocity events SN 2018kjy and SN 2019pxu exhibit double-peaked lines near the [Ca II] doublet early in the nebular phase, similar to those observed in PTF 12bho (Lunnan et al. 2017), although later spectra exhibit a single unresolved [Ca II] feature. Since SN 2018gwo
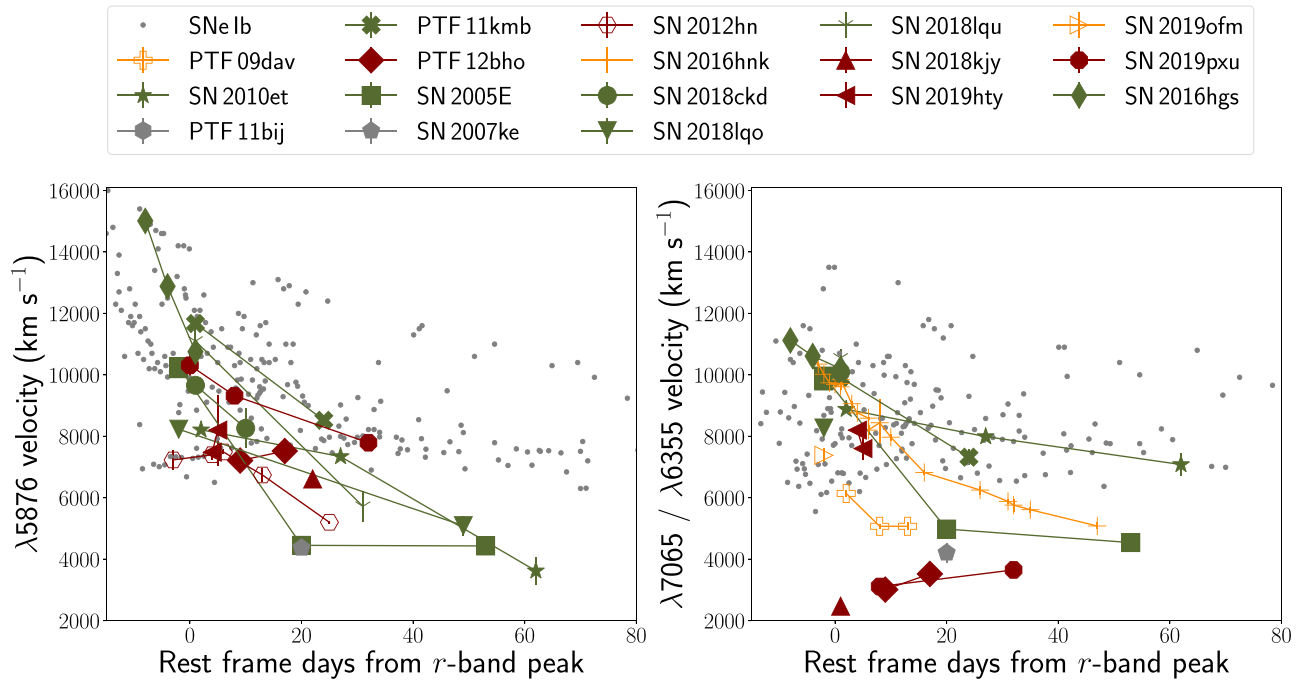
Figure 10. Evolution of photospheric line velocity as a function of phase from the r-band peak for the combined sample of Ca-rich gap transients discussed in this paper. Points joined by solid lines represent the velocity evolution for the same object. We also plot the velocity evolution of the respective lines observed in normal SNe Ib in the sample of Liu et al. (2016), as gray dots in the background. Individual events are shown by markers as indicated in the legend, with their marker colors indicating whether they belong to the Ca-Ib/c class with green (shown in dark green) or red (shown in red) continua, or to the Ca-Ia class (shown in orange). The left panel shows the velocity evolution of the prominent He I λ5876 line in cases where it is unambiguously identified (with solid symbols), or the likely nearby Na I feature (for SN 2012hn in hollow symbols). The right panel shows the velocity evolution of the He I λ7065 feature for the Ca-Ib/c events and the Si II λ6355 feature for the Ca-Ia events.

is a relatively nearby event at 30 Mpc, our nebular-phase spectral sequence extends out to $\approx$235 days, showing that [Ca II] emission continues to dominate the spectrum from the earliest to these very late phases and hence the Ca-rich classification is independent of the exact phase of the nebular spectrum. We note that the events with red continua SN 2012hn, SN 2018kjy, and SN 2018gwo exhibit relatively stronger [O I] lines relative to [Ca II], when compared with other objects observed at similar phases. SN 2012hn and SN 2018gwo are also notable for exhibiting clear signatures of Fe-group elements around 4000–6000 Å similar to the late-time spectra of subluminous SNe Ia.

3.2.2. The Ca-Ia Class

Figure 8 shows the nebular-phase spectra for the Ca-Ia objects, which are dominated by [Ca II] lines. It is important to note the difference between the Ca-Ia objects and the class of 1991bg-like objects in the nebular phase—while the 1991bg-like objects exhibit strong features of Fe-group elements in the blue part of the spectrum in the nebular phase, the Ca-Ia objects show nearly no signatures of such features in the blue-side spectra at similar phases. We demonstrate this by plotting a nebular-phase spectrum of the 1991bg-like object SN 2005ke (Silverman et al. 2012) in Figure 8. SN 2005ke also exhibits a strong emission feature at 7290 Å near [Ca II]; however this feature could be associated with [Fe II] and [Ni II] emission given the strong Fe-group elements observed in the blue side of the spectrum (Flörs et al. 2020; see also Polin et al. 2019b who suggest that this feature is due to [Ca II]). Unlike the Ca-Ib/c objects, the Ca-Ia objects exhibit very weak or no [O I] emission in the nebular phase. The nebular-phase spectrum of

SN 2016hnk (Galbany et al. 2019) exhibits a narrow double-peaked feature at the [Ca II] line, and is noticeably narrower than those of other objects.[32] However this could be due to the very late phase of the spectrum—unavailable for the other, fainter objects in this class.

3.2.3. [Ca II]/[O I] Ratio

In the nebular-phase spectra of the combined sample of events, we fit a Gaussian to the [Ca II] and [O I] emission features to estimate their flux ratio. We compute the fluxes by fitting a single Gaussian (see, e.g., Jerkstrand 2017) to the respective line emission features. We do not compute the absolute flux in these lines as spectro-photometric calibration is not available for several spectra in the literature.[33] Instead, we compute the [Ca II]/[O I] ratio for each spectrum. For several late-time spectra [O I] is barely or not detected. In such cases, we compute an upper limit on the [O I] flux by using the rms of the flux around the expected position of the line center to compute a 1σ upper limit on the [O I] flux assuming that the [Ca II] and [O I] lines have the same velocity width (this provides a lower limit on the [Ca II]/[O I] ratio). We estimate the uncertainties in the line ratios by computing the standard deviations in these quantities from 1000 Monte Carlo realizations of the spectra, where the samples are created by adding flux uncertainties in the same way as with the photospheric-phase spectra. Table 3 lists the best-fit parameters

---

[32] However, the late-time spectrum of SN 2016hnk reported by Jacobson-Galán et al. (2020) does not show a clear double peak.

[33] Absolute calibration would also require contemporaneous photometry, which is largely unavailable.
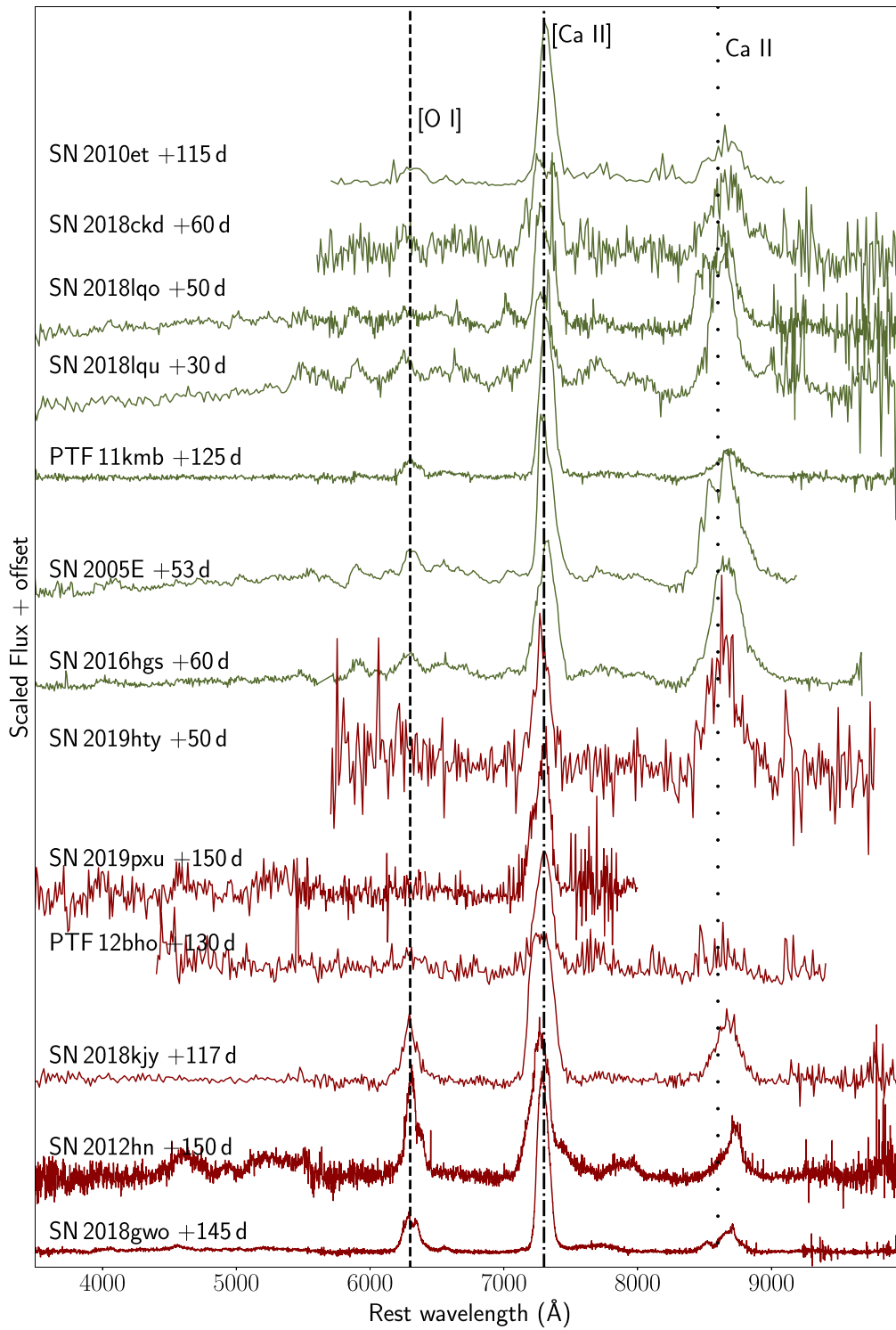
Figure 11. Nebular-phase spectra of the Ca-Ib/c events in the ZTF sample combined with the same for events in the literature. The transient name and phase of the spectrum are indicated next to each spectrum. The color coding of the spectra is the same as that in Figure 6. The prominent nebular lines of [O I], [Ca II], and Ca II are marked.

for the sample of events in this paper as well as for all published spectra in the literature.

We plot the evolution of the [Ca II]/[O I] ratio in these sources compared to a sample of nebular-phase spectra of other types of stripped-envelope SNe in ZTF in Figure 12. These spectra were obtained either as a part of confirmation spectra for candidate Ca-rich gap transients identified from photometry or as a part of nebular-phase follow-up of a volume-limited sample of stripped-envelope SNe (C. Fremling et al. 2020, in

preparation). The Ca-rich gap transients occupy a unique phase space in this plot with high [Ca II]/[O I] at all phases in their evolution. We also show the threshold of [Ca II]/[O I] = 2 used to select the sample of Ca-rich gap transients in this paper, which clearly separates out the Ca-rich events from the normal events, which primarily occupy a phase space of [Ca II]/[O I] $\lesssim$ 1 at all phases. We note that several of the red Ca-Ib/c events exhibit relatively low [Ca II]/[O I] at all phases, where the [Ca II]/[O I] values are smaller by a factor of $\approx$2 than those
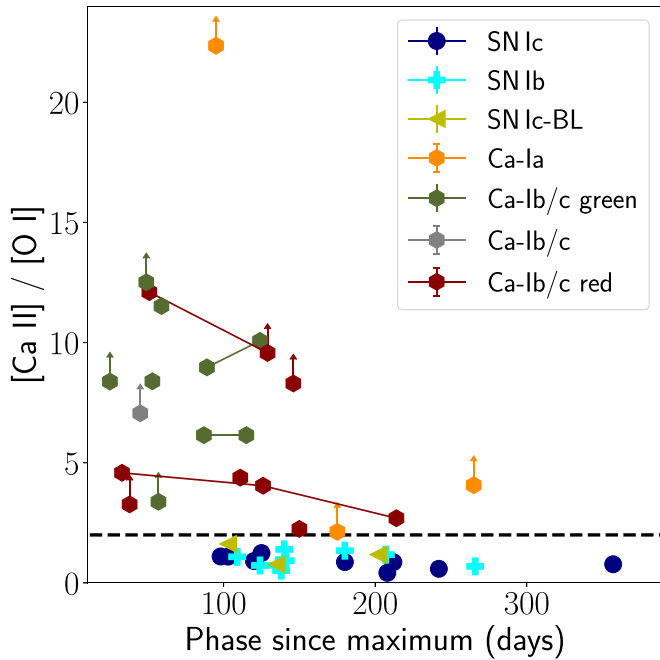
Figure 12. [Ca II]/[O I] ratio for the Ca-rich gap transients and stripped-envelope SNe in the ZTF volume-limited experiment. The black horizontal dashed line shows the [Ca II]/[O I] ratio defined as the threshold in this paper for classification as a Ca-rich transient. Symbols with upward arrows indicate lower limits on the [Ca II]/[O I] ratio where the [O I] feature is not detected with statistical significance. The Ca-rich events are indicated by hexagons with colors that reflect their peak light spectroscopic appearance as discussed in the text.

of the green Ca-Ib/c events. This trend is consistent with the qualitative analysis in Section 3 where we note stronger [O I] features in the red events. The [Ca II]/[O I] estimates result in lower limits for all the Ca-Ia events, suggesting that [O I] is not detected in the nebular-phase spectra of these objects.

3.3. Photometric Evolution

In Figure 13, we compare the r-band light curves of the ZTF sample of Ca-rich gap transients near peak light, to four characteristic light curves of the literature Ca-rich events PTF 09dav (Sullivan et al. 2011), PTF 10iuv (Kasliwal et al. 2012), PTF 12bho (Lunnan et al. 2017), and SN 2016hgs (De et al. 2018a). The comparison sample is chosen to encompass the diversity of the photospheric-phase spectral properties reported in the literature sample. The r-band light curves of the full ZTF sample are largely similar to those of the comparison sample, with the exception of SN 2019ofm and SN 2019pxu, which exhibit more luminous and broader light curves than the comparison objects. SN 2018lqo exhibits a prominent early-time "bump" of ≈ 1 mag as compared to the light curve of SN 2010et. Excess emission is also marginally detected in the light curve of SN 2018kjy, although at much lower significance.

In the bottom right panel of Figure 13, we show a zoomed-in image of the early r-band light curves of SN 2018lqo and SN 2018kjy together with that of SN 2016hgs, which was previously reported as a peculiar Ca-rich gap transient with a prominent double-peaked light curve. For comparison, we plot the well-sampled light curve of SN 2010et, which shows a purely monotonic rise in its early light curve, as is found for all the other events in the full sample. The early excess emission in the light curve of SN 2018lqo is similar in luminosity and timescale to the early emission in SN 2016hgs. Early excess in

SN 2018kjy is detected but is of lower significance, and hence we do not discuss it further here. SN 2018gwo has no ZTF coverage near peak light, although the peak light photometry published on the TNS and the late-time decay tail are consistent with the literature sample of events if we assume that the source was first detected ≈ 7 days before peak light. We caution, however, that we are unable to measure the time of peak or any other light-curve parameter for this object due to the absence of photometry around peak.

3.3.1. Light-curve Parameters

We fit the light curve of each transient (in every filter available) around peak light (within 20 days of peak) with a low-order polynomial (order of 3 to 4) and derive parameters describing the light-curve peak and timescale. We perform the same fitting for all multi-color photometry data available for the literature sample of Ca-rich gap transients. We use the functional fits to determine the times of peak in each filter, the peak apparent and absolute magnitudes (m_p and M_p respectively), and the characteristic rise time and decline time. We define the rise and decay time ($t_{r, 1/2}$ and $t_{f, 1/2}$) of the light curve as the time it takes to rise or decline to half flux from peak light. In addition, we compute the characteristic decay of the light curve (in magnitudes) in 7 days from peak light, denoted by Δm_7.

We estimate uncertainties on these quantities by Monte Carlo sampling of the derived parameters from 1000 realizations of each light curve using the photometric uncertainties of each point in the light curve. We restrict our fitting to photometric bands that have at least one data point before peak light, since it is not possible to estimate the peak magnitude without a corresponding detection before peak. In addition, for sources that do not have photometry sampling the relevant time period of the rise or fall of the light curve, we do not compute the respective Δm_7, rise time, or fall time. For SN 2018gwo, photometry is not available around peak light, and hence we use the reported photometry near peak on the TNS (Wiggins 2018) as a lower limit on the peak magnitude. In computing the peak apparent and absolute magnitude, we also correct the photometry of the literature events for Galactic extinction using the maps of Schlafly & Finkbeiner (2011) and the extinction law of Cardelli et al. (1989) with $R_V = 3.1$.

We do not correct for any additional host galaxy extinction due to the absence of Na I D absorption in their spectra and the remote locations of these events. The only exception is SN 2012hn, for which we assume a host extinction of $E(B - V) = 0.2$ mag, which was estimated from Na I D absorption in its spectra (Valenti et al. 2014). The best-fit parameters from the light-curve fitting are given in Table 5.

3.3.2. Color Evolution

Figure 14 shows the $g - r$ and $r - i$ color evolution of the complete sample of Ca-rich gap transients discussed in this paper. For comparison to other types of SNe, we also show the well-sampled color curves of the nearby SN Ia 2011fe (Nugent et al. 2011) and the SN Ib iPTF 13bvn (Cao et al. 2013). Ca-rich gap transients redden rapidly in $g - r$ color compared to SNe Ia, although the color evolution has a trend similar to that of the SN Ib iPTF 13bvn. However, all the Ca-rich gap transients are redder than iPTF 13bvn in $g - r$ at similar epochs. The same trend is also seen in the $r - i$ color evolution. The $g - r$ evolution of both the Ca-Ib/c objects
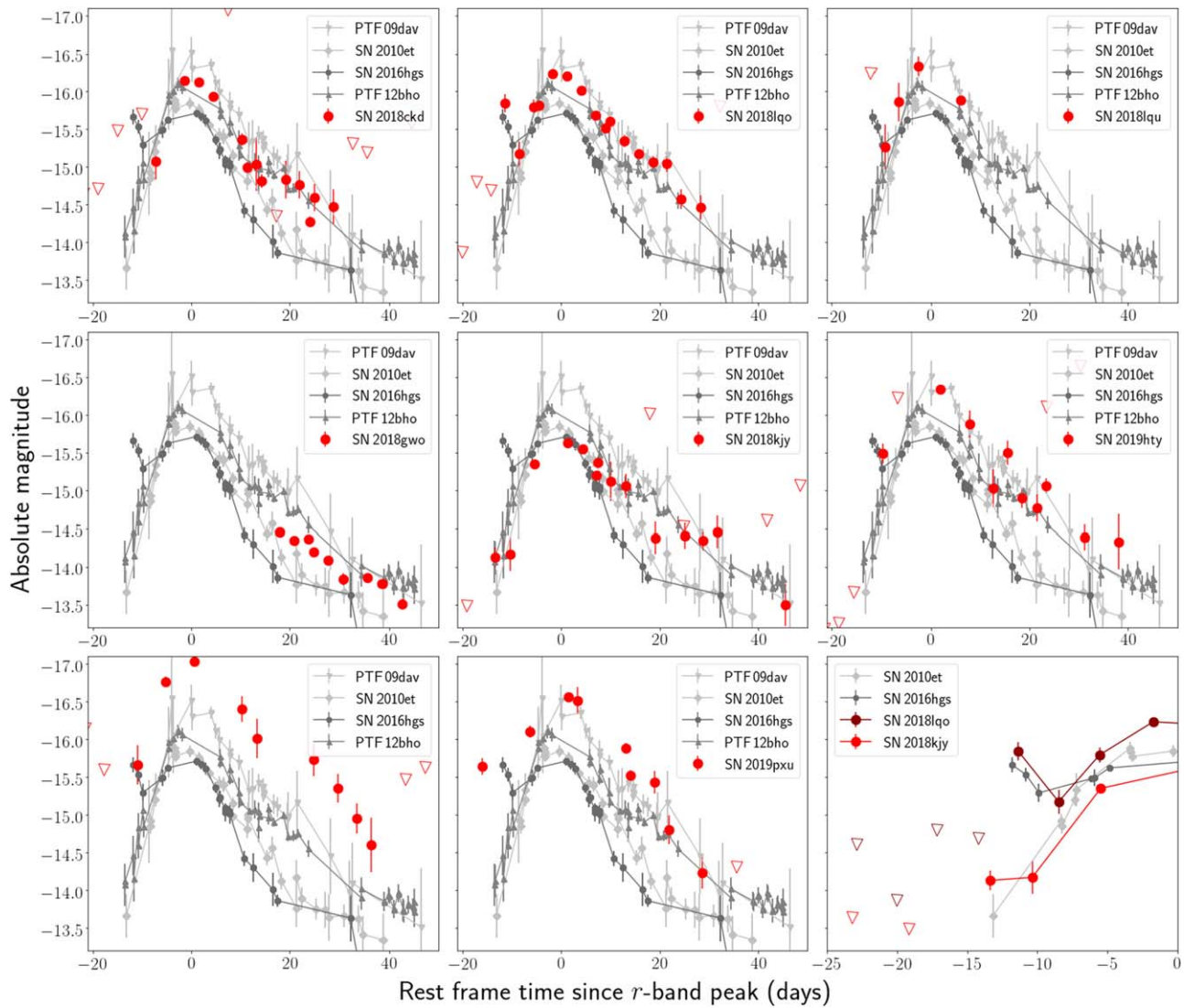
Figure 13. Comparison of the r-band evolution of this sample of Ca-rich gap transients to some previously confirmed events—PTF 09dav (Sullivan et al. 2006), SN 2010et (Kasliwal et al. 2012), PTF 12bho (Lunnan et al. 2017), and SN 2016hgs (De et al. 2018a). In each panel, the r-band photometry for the ZTF sample is presented as red points while the archival sources are plotted in shades of gray. The photometric evolution is shown as a function of rest-frame time from the best estimate of the r-band peak (except in the case of SN 2018gwo; see text). Inverted triangles denote 5σ upper limits. Bottom right panel: Comparison of the early-time bumps seen in the light curves of some of the transients in the ZTF Ca-rich sample to those of the literature events SN 2016hgs (which exhibits an early-time bump; De et al. 2018a) and SN 2010et (which exhibits a monotonic rise; Kasliwal et al. 2012).

with red continua and the Ca-Ia objects is systematically redder than that of the Ca-Ib/c objects with green continua, consistent with the suppressed blue flux in the spectra of the former objects. We note that the complete sample of Ca-rich gap transients occupies a narrow distribution around $g - r \approx 0.7$ mag near peak light, which we later use to simulate their light curves for estimation of volumetric rates from the ZTF survey (Section 5).

3.3.3. Luminosity, Width, and Color Relationship

In Figure 15, we plot the peak r-band magnitude of the transients as a function of the decline in r band in 7 days from peak (Δm_7) and the time taken to fall to half the maximum flux ($t_{f,1/2}$). While some objects have well-sampled light curves on the rise to estimate the time taken to rise from half-maximum flux to maximum, the majority of literature events do not have well-constrained pre-peak light curves and hence we only plot the fall time from peak. We choose the r band as it is the most

commonly available filter for the combined photometric sample and allows us to perform a homogeneous analysis on the largest number of objects. For comparison of this phase space to the general trend followed by thermonuclear SNe, we plot the same parameters for SNe Ia. We use the sample of ZTF SN Ia light curves published in Yao et al. (2019), and compute the same quantities using the fitting techniques mentioned above with the r-band light curves. The distribution of these SNe Ia shows the expected luminosity–width relationship (the Phillips relation; Phillips 1993) with more luminous events being systematically slower-evolving.[34] In order to investigate the presence of a luminosity–width relationship in the full sample

---

[34] Note that the canonical relationship for SNe Ia is defined using the magnitude decline in 15 days after peak in the B band versus peak absolute magnitude M_B. However, we choose to conduct this analysis on Δm_7 against peak absolute magnitude in the r band M_r since the faint and fast-declining Ca-rich gap transients usually lack photometry extending beyond ≈ 15 days from maximum.

Table 5
Light-curve Fit Parameters for the Sample of Ca-rich Gap Transients Presented in This Paper, together with the Fits for the Literature Sample of Ca-rich Gap Transients

Object	Filter	t_p MJD	m_p	M_p	$t_{r,\,1/2}$ (days)	$t_{f,\,1/2}$ (days)	Δm_7 (mag)	References
SN 2018ckd	r	58277.67 ± 0.33	18.95 ± 0.02	-16.17	6.20 ± 0.29	8.68 ± 0.54	0.54 ± 0.04	This work
SN 2018ckd	g	58274.21 ± 1.31	19.69 ± 0.07	-15.43	$\cdots$	10.17 ± 1.78	0.33 ± 0.19	This work
SN 2018ckd	i	58280.67 ± 0.66	19.00 ± 0.08	-16.12	7.88 ± 0.60	12.60 ± 1.07	0.33 ± 0.05	This work
SN 2018lqo	r	58351.92 ± 0.23	19.62 ± 0.02	-16.21	7.33 ± 0.25	10.47 ± 0.50	0.41 ± 0.02	This work
SN 2018lqo	g	58349.97 ± 0.35	20.09 ± 0.05	-15.73	5.80 ± 0.27	7.67 ± 0.41	0.64 ± 0.06	This work
SN 2018lqo	i	58353.41 ± 1.85	19.49 ± 0.17	-16.33	7.69 ± 1.76	11.04 ± 1.49	0.37 ± 0.14	This work
SN 2018lqu	r	58370.83 ± 2.27	19.57 ± 0.30	-16.44	7.40 ± 1.37	$\cdots$	$\cdots$	This work
SN 2018kjy	r	58460.93 ± 0.33	18.85 ± 0.06	-15.63	$\cdots$	12.36 ± 1.49	0.31 ± 0.06	This work
SN 2018kjy	g	58458.18 ± 1.81	19.81 ± 0.25	-14.68	$\cdots$	$\cdots$	0.64 ± 0.46	This work
SN 2019hty	r	58657.90 ± 0.83	18.63 ± 0.05	-16.38	8.81 ± 0.78	11.55 ± 0.76	0.33 ± 0.04	This work
SN 2019hty	g	58653.44 ± 0.68	19.01 ± 0.08	-16.00	$\cdots$	8.05 ± 0.84	0.59 ± 0.12	This work
SN 2019ofm	r	58723.58 ± 1.02	18.60 ± 0.04	-17.03	8.39 ± 1.14	11.07 ± 1.16	0.34 ± 0.06	This work
SN 2019ofm	g	58721.71 ± 1.65	19.69 ± 0.11	-15.94	$\cdots$	$\cdots$	$\cdots$	This work
SN 2019pxu	r	58747.78 ± 0.48	18.90 ± 0.04	-16.56	$\cdots$	11.83 ± 0.57	0.30 ± 0.03	This work
SN2005E	B	53387.15 ± 0.35	18.14 ± 0.13	-14.52	$\cdots$	5.06 ± 1.26	$\cdots$	[1]
SN2005E	V	53387.15 ± 0.51	17.51 ± 0.07	-15.15	$\cdots$	7.93 ± 0.89	0.62 ± 0.12	[1]
SN2005E	R	53388.72 ± 0.71	17.13 ± 0.05	-15.53	$\cdots$	8.90 ± 1.25	0.55 ± 0.12	[1]
SN2005E	I	53389.51 ± 1.32	16.73 ± 0.07	-15.93	$\cdots$	$\cdots$	0.39 ± 0.14	[1]
SN2007ke	R	54369.54 ± 1.82	17.77 ± 0.06	-16.59	$\cdots$	10.29 ± 1.73	0.33 ± 0.14	[1]
PTF 09dav	r	55054.38 ± 0.78	19.86 ± 0.09	-16.22	6.26 ± 0.63	9.28 ± 1.00	0.49 ± 0.08	[2]
SN 2010et	r	55359.36 ± 0.25	19.03 ± 0.03	-15.69	6.30 ± 0.32	9.62 ± 0.55	0.49 ± 0.03	[3]
SN 2010et	g	55357.04 ± 0.39	19.56 ± 0.08	-15.15	$\cdots$	8.01 ± 0.95	0.61 ± 0.11	[3]
SN 2010et	i	55361.86 ± 0.73	18.90 ± 0.04	-15.82	$\cdots$	$\cdots$	0.32 ± 0.05	[3]
PTF 11bij	r	55635.44 ± 1.60	20.28 ± 0.10	-15.68	$\cdots$	9.46 ± 2.40	0.45 ± 0.22	[3]
SN2012hn	B	56031.06 ± 0.48	18.72 ± 0.06	-13.42	$\cdots$	7.44 ± 1.02	0.69 ± 0.12	[4]
SN2012hn	V	56031.60 ± 0.63	17.15 ± 0.03	-14.99	$\cdots$	$\cdots$	0.32 ± 0.05	[4]
SN2012hn	R	56031.06 ± 0.84	16.59 ± 0.02	-15.55	$\cdots$	15.23 ± 1.00	0.14 ± 0.05	[4]
SN2012hn	r'	56035.62 ± 2.94	16.90 ± 0.11	-15.24	$\cdots$	11.74 ± 3.01	0.26 ± 0.21	[4]
SN2012hn	I	56037.90 ± 3.17	16.22 ± 0.01	-15.92	$\cdots$	9.01 ± 3.17	0.40 ± 0.20	[4]
SN2012hn	G	56031.01 ± 0.80	17.45 ± 0.17	-14.69	$\cdots$	9.31 ± 2.22	0.47 ± 0.27	[4]
SN2012hn	g'	56031.01 ± 0.83	17.45 ± 0.16	-14.69	$\cdots$	9.31 ± 2.13	0.47 ± 0.24	[4]
PTF 11kmb	r	55800.73 ± 0.34	18.79 ± 0.01	-15.57	$\cdots$	11.35 ± 0.42	0.28 ± 0.02	[5]
PTF 11kmb	g	55797.95 ± 1.01	19.37 ± 0.03	-14.99	$\cdots$	10.41 ± 1.13	0.36 ± 0.09	[5]
PTF 12bho	r	55992.00 ± 0.25	18.99 ± 0.03	-16.04	6.97 ± 0.27	10.29 ± 0.35	0.42 ± 0.02	[5]
SN 2016hgs	r	57691.80 ± 0.24	18.91 ± 0.03	-15.45	$\cdots$	9.43 ± 0.38	0.42 ± 0.03	[6]
SN 2016hgs	g	57683.22 ± 1.00	19.48 ± 0.10	-14.88	$\cdots$	13.29 ± 0.98	0.25 ± 0.10	[6]
SN 2016hgs	i	57692.85 ± 0.21	18.54 ± 0.03	-15.82	$\cdots$	9.47 ± 0.34	0.44 ± 0.03	[6]
SN2016hnk	B	57691.35 ± 0.60	18.92 ± 0.05	-15.31	$\cdots$	7.00 ± 0.62	0.75 ± 0.09	[7]
SN2016hnk	V	57691.74 ± 0.74	17.46 ± 0.03	-16.77	$\cdots$	$\cdots$	0.39 ± 0.08	[7]
SN2016hnk	r	57692.78 ± 0.43	17.18 ± 0.02	-17.05	$\cdots$	12.78 ± 0.62	0.32 ± 0.03	[7]
SN2016hnk	i	57691.34 ± 0.78	17.34 ± 0.03	-16.89	$\cdots$	$\cdots$	0.27 ± 0.06	[7]
SN2016hnk	z	57697.79 ± 2.42	17.38 ± 0.07	-16.85	$\cdots$	$\cdots$	0.09 ± 0.06	[7]
SN2016hnk	g	57695.27^*	18.53 ± 0.04	-15.70	$\cdots$	6.47 ± 2.25	0.76 ± 0.10	[7]

Note. t_p denotes the time of peak in the respective filter, m_p denotes the peak apparent magnitude (corrected for Galactic extinction using the maps of Schlafly & Finkbeiner (2011)), M_p denotes the peak absolute magnitude, $t_{r,\,1/2}$ denotes the rise time to peak from half of the peak flux, and $t_{f,\,1/2}$ denotes the fall time from peak to half the peak flux. Δm_7 denotes the drop in magnitude from the time of peak to 7 days after peak. Photometry for some of the sources in the literature was obtained from the Open Supernova Catalog (Guillochon et al. 2017). The data were originally published in [1] Perets et al. (2010), [2] Sullivan et al. (2011), [3] Kasliwal et al. (2012), [4] Valenti et al. (2014), [5] Lunnan et al. (2017), [6] De et al. (2018a), and [7] Galbany et al. (2019).

(This table is available in its entirety in machine-readable form.)

of Ca-rich objects, we compute the Spearman correlation coefficient between the two pairs of plotted parameters and find no significant evidence of correlation. The corresponding correlation coefficients are 0.25 between M_p and Δm_7 (p-value of 0.35) and -0.36 between M_p and $t_{f,\,1/2}$ (p-value of 0.18), suggesting no statistically significant correlation between these parameters.

We now examine possible differences in the photometric properties between the Ca-Ib/c and the Ca-Ia objects. Due to the absence of peak light spectroscopy for SN 2007ke and

PTF 11bij, we are unable to ascertain the nature of the blue continuum at peak light; however, their early nebular-phase spectra show lines characteristic of SNe Ib/c suggesting their membership in the class of Ca-Ib/c objects. The peak luminosity distributions of green and red events among the Ca-Ib/c objects are consistent with each other; however, the Ca-Ia objects are typically more luminous. The total number of events remains too small for us to draw a conclusion on the statistical significance of the differences. Specifically, we note that the Ca-Ib/c events with red continua exhibit systematically
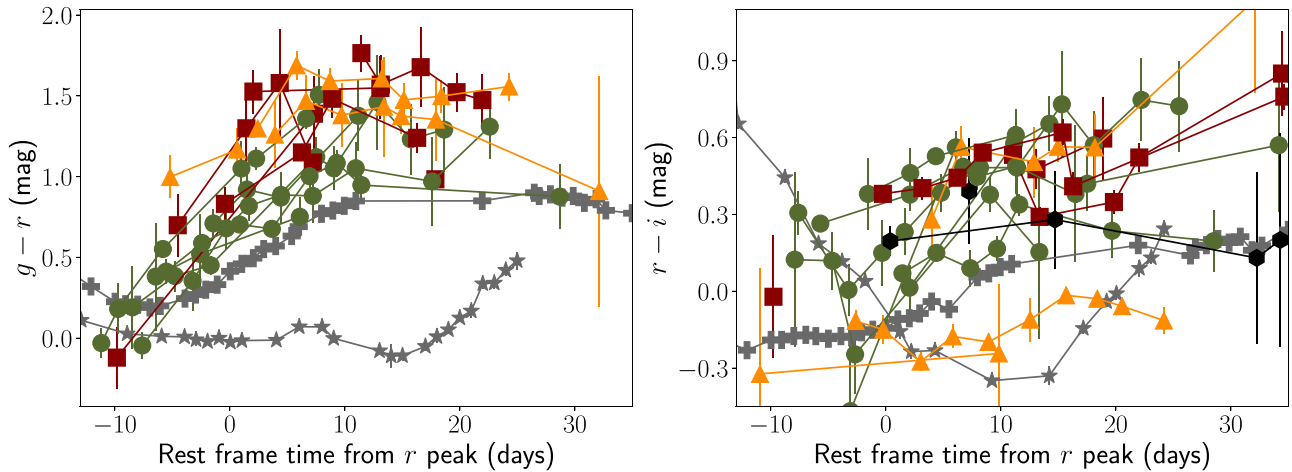
Figure 14. Comparison of the $g - r$ and $r - i$ color curves of the sample of known Ca-rich gap transients, color-coded by their spectroscopic membership in the green Ca-Ib/c (green circles), red Ca-Ib/c (red squares), or Ca-Ia (orange triangles) class. For comparison, we also show the color evolution curves of the Type Ia SN 2011fe (Nugent et al. 2011) as dark gray stars and the Type Ib iPTF 13bvn (Cao et al. 2013) as dark gray crosses, which are systematically bluer in $g - r$ than the Ca-rich gap transients at similar epochs. Events in the combined sample without a peak light spectrum are shown as black circles.
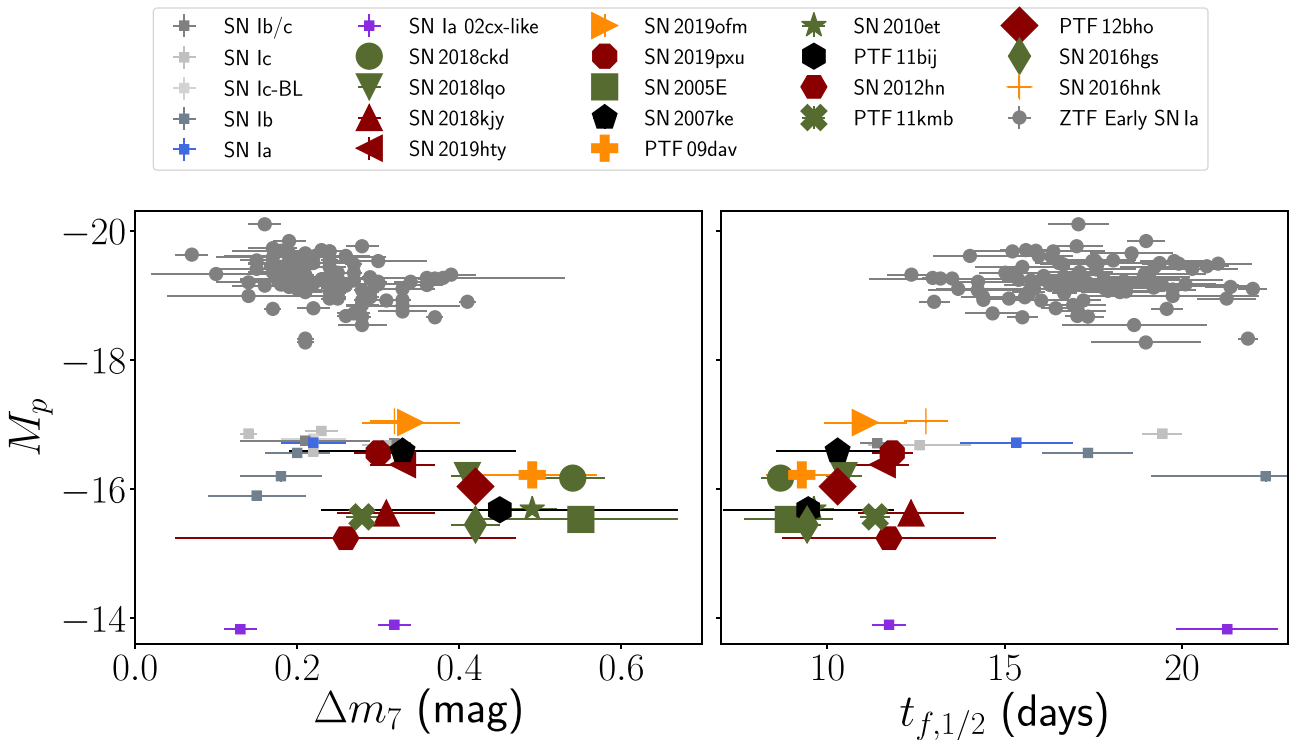
Figure 15. Luminosity–width phase space for the r-band light curves of Ca-rich gap transients (symbols are shown with the object names in the legend). The individual events are colored by their spectral type at peak light. Green Ca-Ib/c events are indicated by green and those with reddened continua are indicated by red. Ca-Ia events are indicated in orange and the marker symbols for all events are indicated in the legend. We are unable to constrain the peak light spectroscopic properties of SN 2007ke and PTF 11bij, and hence show these objects in black. For comparison, we plot the same phase space of timescales for the ZTF 2018 early SN Ia sample in Yao et al. (2019) as gray dots, together with the same parameters for objects in the control sample (squares; indicated in the legend by their spectroscopic type at peak).

slower light curves than the Ca-Ib/c events with green continua, as shown by their smaller Δm_7 and larger $t_{\mathrm{f},1/2}$ values. A two-sample Kolmogorov–Smirnov (K-S) test suggests that the null hypothesis probability that the two sets of values are drawn from the same underlying population is <5% for $t_{\mathrm{f},1/2}$ and <18% for Δm_7. While this is only marginally significant due to the small number of events, we further examine this trend in Figure 16.

We show the dependence of Δm_7 as a function of the $g - r$ color of the transient near peak light in Figure 16. The $g - r$

photometric colors at peak light are not available for several events in the combined sample, and hence we use both the spectro-photometric colors derived from peak light spectroscopy and the photometric colors where available. Since the photometric colors are not always available at the same phase as the spectroscopy, there are differences between the derived photometric and spectro-photometric colors. The Ca-Ib/c events separate into two classes of events based on their $g - r$ colors, while the Ca-Ia events exhibit colors intermediate between the two classes but redder than the green Ca-Ib/c
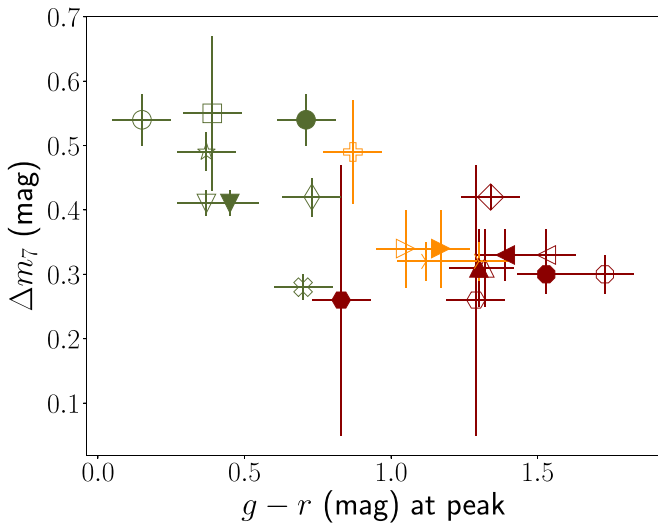
Figure 16. Dependence of the rate of light-curve evolution post-peak in the r band (Δm_7) on the transient $g - r$ color at peak. The symbol color coding and markers are the same as those used in Figure 15. Hollow symbols indicate colors computed from spectro-photometry on observed spectra within ≈ 10 days of peak light, while solid symbols indicate colors derived from peak light photometry where available. The colors have been corrected for foreground Galactic extinction.

events. Specifically, we note that the Ca-Ib/c events with bluer $g - r$ colors at peak exhibit larger Δm_7 (faster photometric evolution) at peak, while the red Ca-Ib/c events are slower-evolving, consistent with the trend observed in Figure 15. However, we caution against drawing conclusions about any correlations between these two parameters as the photometric and spectro-photometric colors are not available at the same phase in all cases. We find that the green and red events in the Ca-Ib/c sample are separated at $g - r \approx 1$ mag at peak light; the Ca-Ia objects also exhibit redder colors of $g - r > 1$ mag at peak, consistent with their line-blanketed spectra.

3.3.4. Dependence on Spectroscopic Properties

In Figure 17, we plot the photospheric velocity at peak light against the peak r-band magnitude of the sources to examine the dependence of the photospheric-phase velocity on the peak luminosity of each event. In the case of SN 2018kjy, we are unable to measure the He line velocities directly due to the large number of narrow lines, and hence we estimate typical line velocities in the spectra from the P-Cygni absorption velocities of ≈ 4000 km s^{-1}. We do not find a clear dependence of the photospheric-phase velocity on the peak luminosity of the events, but note that the events with green continua have higher photospheric-phase velocities than the red events.

The right panel of Figure 17 shows the dependence of the peak light photospheric velocity on the rate of decay of the light curve, Δm_7. As per the formalism for radioactively powered light curves laid down in Arnett (1982), the peak light photospheric velocity and light-curve evolution near peak are indicators of the ejecta mass in the explosion. We thus also plot lines of constant ejecta mass in the right panel to guide the eye to the range of ejecta masses in the sample. We construct these lines by creating analytic light curves using the formalism of Arnett (1982) assuming two constant opacities of $\kappa = 0.07$ cm^2 g^{-1} (as relevant for SNe Ib/c; Cano 2013; Taddia et al. 2018) and $\kappa = 0.2$ cm^2 g^{-1} (relevant for completely ionized

hydrogen-free material). We caution, however, that the Arnett diffusion model has several assumptions which may not be satisfied in these explosions (see Khatami & Kasen 2019 for a review). We do not find a dependence of the peak photospheric velocity on the light-curve evolution near peak. It is important to note that the inferred ejecta masses can vary significantly depending on the assumed opacity. The majority of Ca-Ib/c events with green continua lie on the contours of lower ejecta masses (between 0.1 and 0.4 $M_\odot$), while the red Ca-Ib/c and Ca-Ia events lie near larger ejecta masses (up to ≈ 1 $M_\odot$ for $\kappa = 0.07$ cm^2 g^{-1}, but < 0.5 $M_\odot$ for $\kappa = 0.2$ cm^2 g^{-1}). However, we stress that redder events also likely have higher effective optical opacity in the ejecta than their green counterparts, as evident from the strong suppression of flux in the blue, which would suggest increased bound–bound opacity from Fe-group material. As such, this effect would decrease the ejecta masses inferred from assuming a constant opacity across all events.

3.3.5. Late-time Photometric Evolution

In Figure 4, we show the late-time (> 40 days after r-band peak) photometric evolution of the sample of Ca-rich gap transients presented in this paper together with published photometry of events in the literature. While most of the late-time photometry presented here was obtained using targeted follow-up observations using P60 + SEDM, P200 + WaSP, and Keck I + LRIS, we also stack several epochs (over up to 30 days) of the high-cadence ZTF observations to derive flux limits at late times. Owing to its small distance, SN 2018gwo has good photometric follow-up from ZTF up to ≈ 100 days from the estimated peak time. We also show a numerically computed Arnett model (Arnett 1982) for the decline rate expected from a radioactively powered light curve with ejecta mass of 0.5 $M_\odot$ and ^{56}Ni mass of 0.015 $M_\odot$. The model parameters are chosen based on the typical values found in previous studies (Perets et al. 2010; Kasliwal et al. 2012; Valenti et al. 2014; De et al. 2018a).

Compared to the expected ^{56}Ni decay tail shown in Figure 4, the luminosity at late times is much fainter than the prediction from the Arnett model, while the decay slope is also steeper for these events. The characteristics are consistent with the fast-rising light curves of these events, which suggest low ejecta masses and incomplete γ-ray trapping at late times. Figure 4 also shows the last deep photometric limits obtained using P200 and Keck for this sample of events, extending out to ≈ 1.5 years after peak light. Although SN 2018gwo is detected with Keck (owing to its small distance) out to ≈ 500 days after peak light, the very late-time follow-up photometry for all the objects could be potentially contaminated by underlying host systems. We discuss the presence of potential underlying host stellar systems from late-time imaging in Section 4.

4. Locations and Host Environments

Here, we examine the environments and host properties of the Ca-rich gap transients analyzed in our sample. The host environments of the literature sample of transients have been noted in several works previously for their preference for old environments located far away from their host galaxies, with no evidence of parent stellar populations at the location of the transients (Perets et al. 2010, 2011; Kasliwal et al. 2012; Yuan et al. 2013; Lyman et al. 2014, 2016; Mulchaey et al. 2014;
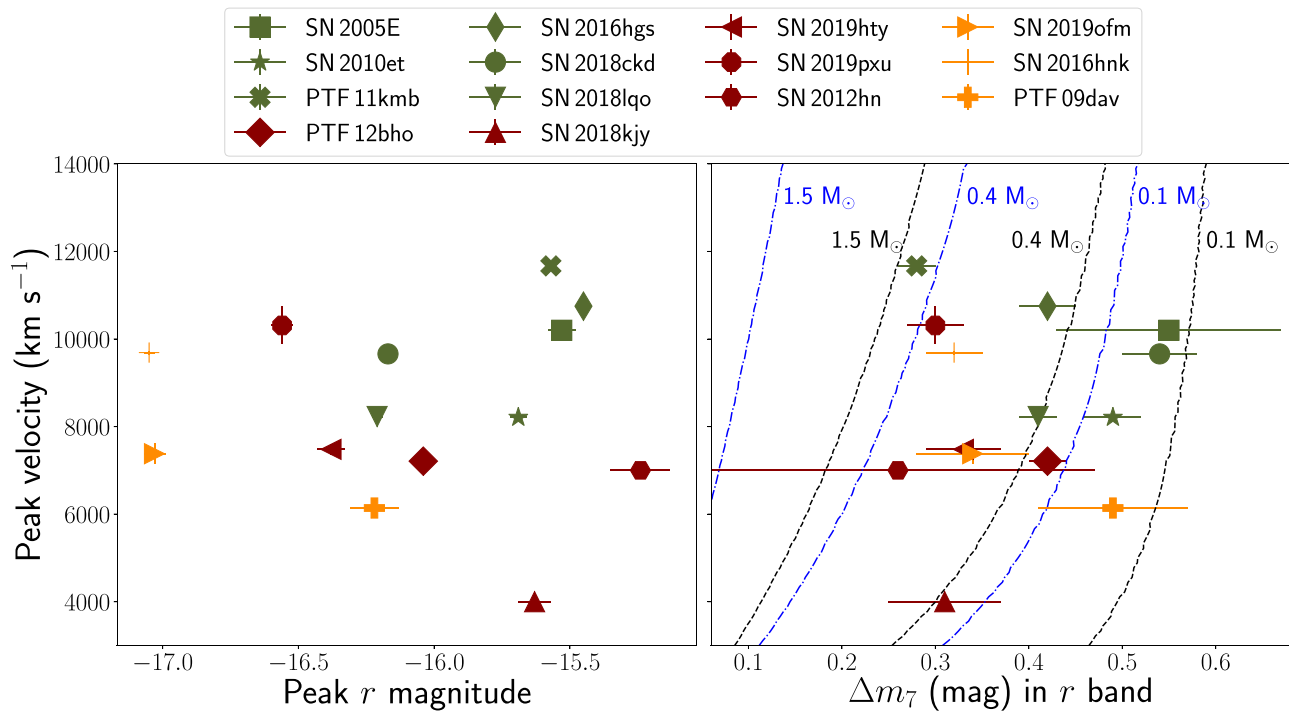
Figure 17. Photospheric-phase line velocities as a function of the light-curve peak luminosity (in the r band) and the timescale of evolution (characterized by Δm_7) for the sample of Ca-rich gap transients analyzed in this paper. We use the velocity of the He I $\lambda 5876$ feature from the spectrum taken closest to the estimated time of peak light in the r band (if available within 10 days of peak) for the Ca-Ib/c objects, and the Si II $\lambda 6355$ velocity for the Ca-Ia objects. The left panel shows the peak velocity as a function of the peak r-band magnitude and the right panel shows the peak velocity as a function of Δm_7. The right panel also shows the contours of the constant ejecta mass computed using the analytical model of Arnett (1982) to guide the eye on the range of ejecta masses found in the sample. We show the ejecta mass contours for two different optical opacities of $\kappa = 0.07$ cm^2 g^{-1} (black dashed lines) and $\kappa = 0.2$ cm^2 g^{-1} (blue dotted–dashed lines).

Lunnan et al. 2017; De et al. 2018a; Shen et al. 2019). Additionally, Yuan et al. (2013) found that the offset distribution of a subset of events in the literature sample is inconsistent with the stellar mass profiles of their host galaxies, while Yuan et al. (2013) and Shen et al. (2019) show that their offset distributions are consistent with globular clusters or old metal-poor stellar populations. Frohmaier et al. (2018) show that the preference for large host offsets in the PTF sample cannot be explained by the reduced recovery efficiency on top of bright galaxies. However, all of these works are based on heterogeneous samples of events gathered from different surveys with diverse selection effects that are difficult to quantify. As this is the first unbiased systematic experiment to classify a large sample of Ca-rich gap transients, we perform a systematic analysis of their locations and host environments.

4.1. Host Galaxy Morphology

We begin with analyzing the host galaxy morphologies of these events. Our selection criteria for these events did not include any restrictions on the host galaxy type. Six out of the eight events in this sample were found in S0/E early-type host galaxies (four out of the eight were in E-type galaxies), and all of the events were found at projected galactocentric offsets > 6 kpc. Two events (SN 2019ofm and SN 2019pxu) were found in late-type galaxies, although at relatively large host offsets (11 and 17.5 kpc respectively, corresponding to host-normalized offsets of 2.1 and 4.5 R_e[35]). Notably, both the Ca-Ia objects SN 2016hnk and SN 2019ofm were found in late-type star-forming galaxies, while PTF 09dav was found to be

hostless in late-time imaging and the nearest galaxy with a known redshift was a star-forming spiral ≈40 kpc from the transient location. However, we caution that PTF 09dav is close to several faint extended sources (see Figure 3 in Kasliwal et al. 2012), which could be nearby dwarf galaxies; it also shows Hα emission in its latest nebular-phase spectrum, although it could be associated with circumstellar photoionized gas around the SN (Kasliwal et al. 2012).

Nevertheless, the preference of these transients for old host environments with large offsets is striking as compared to other types of transients in the local universe. The preference for early-type galaxies in this sample is reminiscent of that observed for 91bg-like SNe Ia (Howell 2001; Neill et al. 2009; Perets et al. 2010; Taubenberger 2017), although the preference of Ca-rich gap transients for early-type galaxies is more extreme than that for these events. A total of 19 91bg-like SNe Ia were classified in the CLU experiment in the span of time considered in this paper, out of which 10 events were found in early-type galaxies while the rest were in late-type galaxies. The near-equal distribution in early- and late-type galaxies for 91bg-like SNe Ia is consistent with the stellar mass distribution between early-type and late-type galaxies in the local universe (Kochanek et al. 2001; Bell et al. 2003).

4.2. Locations and Offset Distribution

In Figure 18, we compare the host offset distribution of the ZTF Ca-rich gap transients (both in physical projected distance and in host-normalized distance) to that of other types of SNe in the volume-limited experiment—SNe Ia, SNe II, and SNe Ib/c. The host offsets for each event in the sample are computed from the host galaxy in the CLU catalog, which is

---

[35] R_e is defined as the half-light radius of the apparent host galaxy.
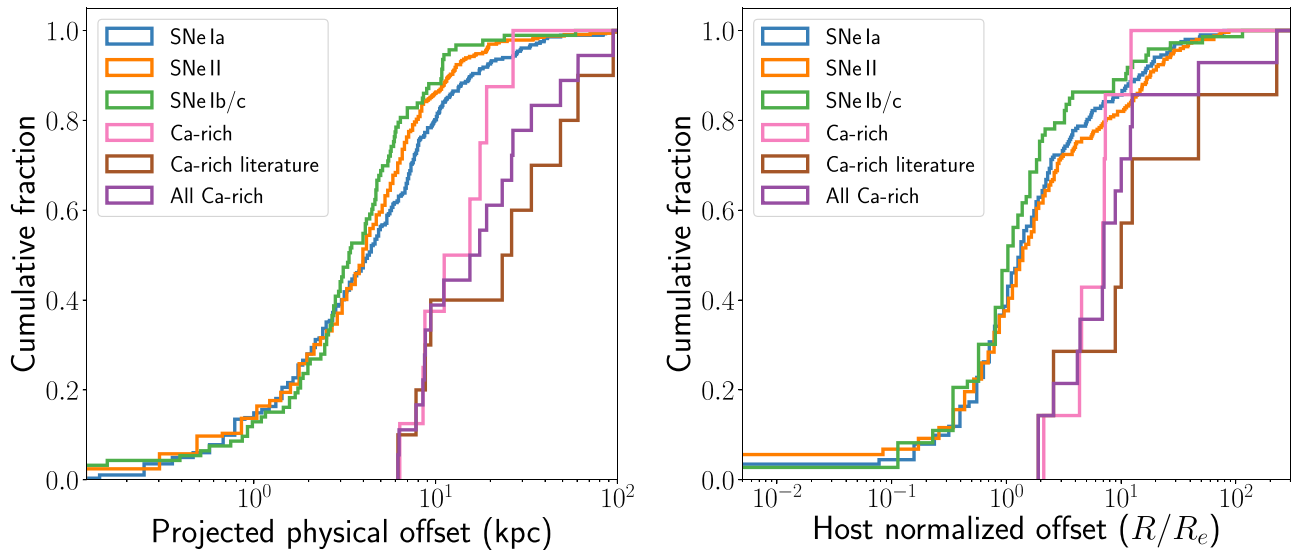
Figure 18. Projected offset distribution of all transients in the CLU experiment. The left panel shows the distribution in units of physical projected distance (kpc), while the right panel shows the distribution in host offset normalized by the half-light Petrosian radius of the host galaxy. The half-light Petrosian radii are derived from the SDSS (Abolfathi et al. 2018) catalog, and hence are limited to transients occurring in the SDSS footprint.

confirmed to be at the same redshift as the SN. As shown in Figure 18, SNe Ib/c show systematically smaller physical offsets than SNe II, while SNe II show systematically smaller offsets than SNe Ia. However, the Ca-rich gap transients exhibit a significantly skewed distribution of larger offsets (in terms of both physical offsets and host-normalized offsets) than any of the object types in the comparison sample.

Using a two-sample K-S test, we can rule out the possibility that the entire population of SNe Ia and Ca-rich gap transients in the ZTF sample originates from the same underlying population at 99.9% confidence. For comparison, we also show the host offset distribution of the literature sample of Ca-rich gap transients and the total combined sample of Ca-rich gap transients, whose distribution appears to extend out to larger galactocentric offsets. A K-S test between the ZTF and literature samples of offsets does not indicate a statistically significant difference between the two distributions (p-value of 0.28); however, the limitation of the CLU experiment to finding transients within $100''$ of their host galaxies prevents us from finding objects with very large host offsets. The consistent offset distributions justify the use of the full sample of offset distributions to estimate the incompleteness of the CLU sample (Section 5).

Several previous works have suggested that the lack of Ca-rich gap transients at small host offsets may be due to their faint light curves, which would make them difficult to detect on top of high surface brightness regions on galaxies (Foley 2015). Frohmaier et al. (2017) presented the recovery efficiency for the PTF pipeline as a function of the source magnitude and local surface brightness, demonstrating that the recovery efficiency is indeed lower in regions of high surface brightness. Yet, Frohmaier et al. (2018) showed that the preference of the small PTF sample of Ca-rich gap transients for large host offsets cannot be explained by the reduced recovery efficiency on bright galaxy backgrounds.

While the recovery efficiency for the ZTF pipeline is currently not available, we can empirically examine if the offset locations for the faint Ca-rich gap transients in the ZTF sample can be primarily explained by poor recovery efficiency on the cores of galaxies. In Figure 19, we show the projected offset
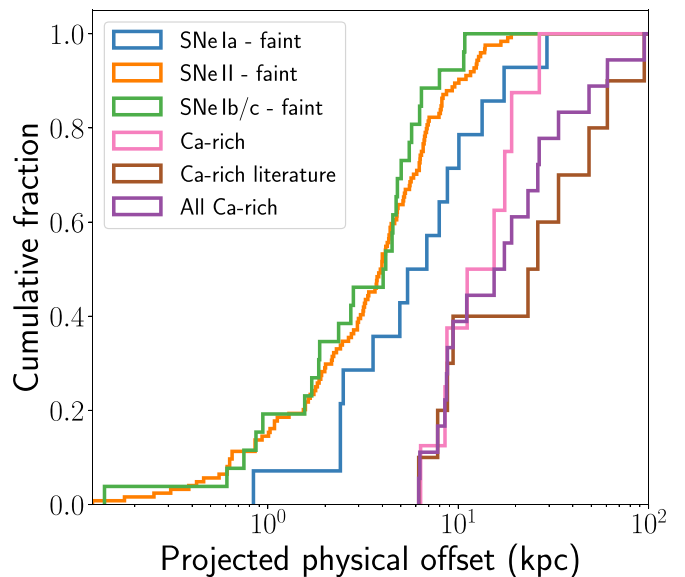
Figure 19. Projected offset distribution of all faint transients that were detected at $M > -17$ in the CLU experiment.

distribution of all transients fainter than $M = -17$ mag in the CLU experiment. The offset distribution of the SNe II, SNe Ib/c, and SNe Ia in this low-luminosity sample extends from the smallest offsets at <1 kpc to ≈ 30 kpc. Notably the Ca-rich gap transients continue to stand out with large host offsets of at least 5 kpc (extending out to ≈ 40 kpc). The skewed offset distribution of Ca-rich gap transients even in this sample of low-luminosity transients suggests that the low recovery efficiency of faint transients cannot completely explain the remote locations of these events.

We further compare the environments of 91bg-like SNe Ia to those of the Ca-rich gap transients. We plot the projected offset distributions of all SNe Ia, 91bg-like SNe Ia, and Ca-rich gap transients in Figure 20. We also show the simulated radial distribution of globular clusters from Shen et al. (2019) for two different Sérsic indices. The literature sample analyzed in this
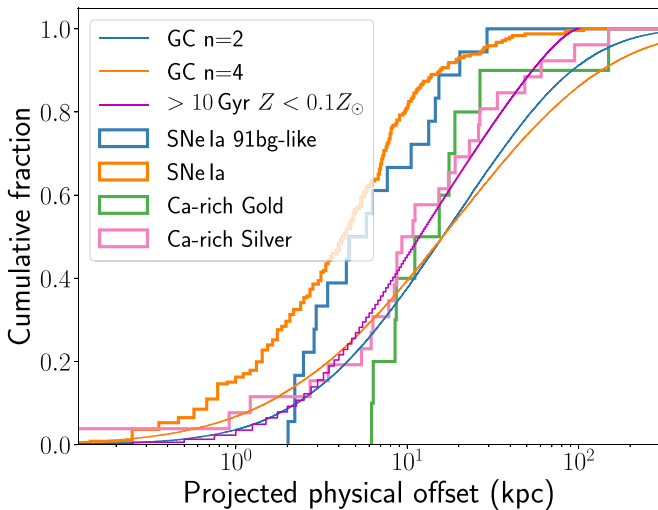
Figure 20. Offset distribution comparison of the "gold" and "silver" samples of Ca-rich gap transients discussed in this paper to those of all SNe Ia and 91bg-like SNe Ia in the volume-limited experiment. Our gold sample includes the literature sample of events (which includes the gold sample discussed in Shen et al. 2019 in addition to the Ca-Ia objects discussed in this work) and the ZTF sample, while the silver sample includes the silver sample discussed in Shen et al. (2019) in addition to the ZTF sample of events. We also show the simulated offset distribution of globular clusters for two Sérsic indices, as well as the offset distribution for old (>10 Gyr), metal-poor ($Z < 0.1\, Z_\odot$) stars discussed in Shen et al. (2019).

paper includes Ca-Ia events from the literature, in addition to the "gold" sample in Shen et al. (2019). Thus, in plotting the radial offset distribution of the sample of Ca-rich events, we define our new "gold" sample by adding the ZTF sample of events to the literature sample (including all the Ca-Ia objects, amounting to a total of 18 events).

We also define a new "silver" sample by adding the ZTF sample of events to the silver sample in Shen et al. (2019), which included Ca-rich events without photometric constraints at peak light (amounting to a total of 24 events). 91bg-like SNe Ia show systematically smaller offsets than the Ca-rich gap transients in this sample, and systematically larger offsets than the full population of SNe Ia. A two-sample K-S test between the offset distributions of SN 91bg–like SNe Ia and the gold and silver samples of Ca-rich gap transients produces null hypothesis probabilities of being drawn from the same underlying population at <2.5% and <10% respectively. We conclude that the discrepancies between the environments of 91bg-like and Ca-rich events suggest that stellar mass alone does not dictate the rates of Ca-rich gap transients. Long delay times and/or low metallicities in these remote environments of early-type galaxies have thus been suggested to play an important role (Perets et al. 2010; Yuan et al. 2013; Meng & Han 2015; Shen et al. 2019).

In addition to being skewed toward larger offsets compared to SNe Ia, the Ca-rich gold and silver samples exhibit offset distributions different from those of globular clusters and old metal-poor stars from IllustrisTNG simulations (Marinacci et al. 2018; Naiman et al. 2018; Nelson et al. 2019). Specifically, the gold sample distribution is skewed toward larger offsets than these two populations. However, the silver sample offset distribution is more consistent with both these distributions (consistent with the result in Yuan et al. 2013 and Shen et al. 2019), although there are discrepancies at relatively large offsets. Notably, all of the Ca-rich gap transients found in

this experiment are in "rich" environments with $\gtrsim$10 galaxies clustered near the nominal host, while Shen et al. (2019) found that 17% of globular cluster hosts are in rich clusters (see Section 4.3).

We examine deep late-time images of the locations of these transients to investigate if there is any evidence for underlying stellar populations at these locations. We show these images in Figure 21. SN 2018ckd shows clear evidence of a relatively bright pointlike source (marked with a yellow circle) offset by <1 kpc from the transient location. This source is also detected in archival imaging of the field in the Dark Energy Camera Legacy Survey's Data Release 8 (Dey et al. 2019) at a magnitude of $r \approx 23.5$ mag and $g - r \approx 0.3$ mag, corresponding to an absolute magnitude of ≈ -11.5 mag if at the redshift of the transient. However, the source is unlikely to be a globular cluster as it is more luminous than nearly the entire known luminosity function of globular clusters (Harris 1996). We orient the slit to include the extended galaxy $\approx 10''$ to the north of SN 2018ckd (marked with a yellow circle) during nebular-phase spectroscopy, and find it to be an unrelated background galaxy at $z = 0.1$, consistent with the photometric redshift of the object in SDSS.

An extended source is detected near the location of SN 2018lqu (marked with a yellow circle), although its redshift is unknown. If at the redshift of the transient, its magnitude of $r \approx 21.4$ would imply an absolute magnitude of $M_r \approx -14.5$ mag similar to a dwarf galaxy's. SN 2018lqo, SN 2018gwo, and SN 2019hty show evidence of faint and extended sources underneath their locations, which likely contaminate our photometry measurements during very late-time imaging (Figure 21). However, we caution that the density of unrelated background sources at the depths of the late-time images (≈ 25 mag) is high (Hogg et al. 1997). Using the methodology of Bloom et al. (2002), we find that the chance coincidence probability of an unrelated ≈ 25 mag galaxy within a $5''$ radius of the transient is $\sim 50\%$, while the same for a $10''$ radius is $\sim 95\%$. Thus, the association of these sources to the transients can only be determined from deep spectroscopy in the future. SN 2018kjy is notable for the smallest host offset (≈ 6 kpc) in the ZTF sample, and is located within the halo of its host galaxy. SN 2019ofm is found on top of its spiral host galaxy, while SN 2019pxu is at a large offset from its spiral host and has a point source (marked with a yellow circle) within $5''$ of its location ($M_r \approx -12.1$ mag if at the redshift of the transient). The latest Keck images of SN 2019ofm and SN 2019pxu still show the transient clearly. Future deep imaging for these events will help disentangle the potential host contamination in our latest photometry measurements, as well as allow inspection of potential underlying hosts.

4.3. Group and Cluster Environments

Given the large host offsets of the Ca-rich gap transient sample, we analyze the environments of the assumed host galaxies to check if they are part of a larger group or cluster that may explain the remote locations of these transients. Mulchaey et al. (2014), Lunnan et al. (2017), and De et al. (2018a) performed a similar analysis on the literature sample of Ca-rich gap transients, and demonstrated that these objects prefer host galaxies in groups and clusters. For each transient, we construct a sample of nearby galaxies by selecting galaxies from the CLU catalog (with a previously known spectroscopic redshift) within
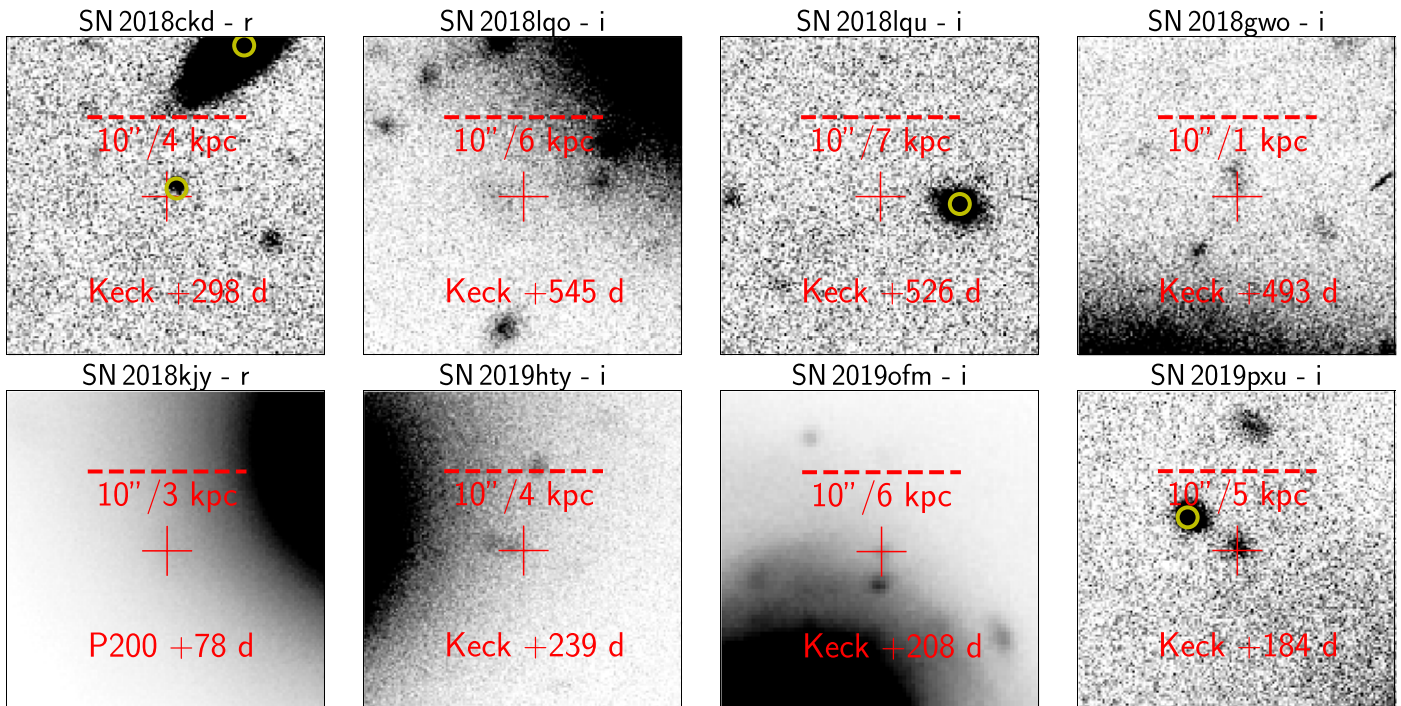
Figure 21. Cutouts of the locations of the Ca-rich gap transients presented in this paper from late-time ground-based imaging of the transient locations. North is up and east is left in each cutout. The source name, filter and phase of observation, instrument used, and physical scale of the image at the redshift of the transient are shown in each panel. The crosses show the location of the transient. Yellow circles mark the locations of potential host systems also detected in pre-explosion archival imaging (see text).

a projected radius of 1 Mpc and a recession velocity difference of ± 3000 km s^{-1} from the location of the transient.

We emphasize that since galaxy catalogs are highly incomplete at the redshifts of these transients (Kulkarni et al. 2018; Fremling et al. 2019), these distributions are only lower limits to the true number of galaxies in the environments of these transients. We show the velocity histograms of the identified galaxies in Figure 22. As shown, the environments of the Ca-rich gap transient host galaxies are largely dominated by groups and clusters with at least 10 known objects within the selection criteria defined above. SN 2018lqo is in the densest environment with 87 known nearby galaxies. We thus conclude that all of the transients in the ZTF sample are in group or cluster environments, consistent with that reported for the literature sample presented in Lunnan et al. (2017) and De et al. (2018a).

5. Volumetric Rates in the Local Universe

In this section, we estimate the volumetric rates of Ca-rich gap transients using the ZTF CLU experiment. As a large-scale systematic and controlled experiment, the volume-limited SN classification effort provides the first direct way to estimate the volumetric rates of this class within 200 Mpc due to its high spectroscopic completeness ($\approx$90%) down to the experiment limiting magnitude of 20 mag.

5.1. Demographics from the Volume-limited Experiment

Since the volume-limited experiment has high spectroscopic classification completeness, a straightforward way to estimate the volumetric rates of Ca-rich gap transients relative to other SNe is to compare the number of events. We perform this analysis by restricting the sample of transients in the CLU

experiment to within the volume where Ca-rich gap transients are detectable. Based on the luminosity function of known events discussed in Section 5.2, we find that the average Ca-rich gap transient (peaking at $M = -16$ mag) is detectable out to 150 Mpc for a flux limit of $r = 20.0$ mag, which is the target limiting magnitude of the CLU experiment. Within the experiment duration mentioned above, a total of eight Ca-rich gap transients were detected along with 133 SNe Ia that were classified in the same volume. So, we can place a lower limit on the rates of Ca-rich gap transients of 6% of the volumetric rates of SNe Ia, or 1.5×10^{-6} Mpc^{-3} yr^{-1} (assuming the SN Ia rate is 2.5×10^{-5} Mpc^{-3} yr^{-1}; Frohmaier et al. 2019). Note that this estimate is likely an underestimate of the true rate of Ca-rich gap transients since SNe Ia will be bright in the 150 Mpc volume (peaking at $\approx$17 mag) and thus detectable during the survey for at least $\approx$100 days around peak, while the average Ca-rich gap transient in this volume is visible for $\approx$10–20 days. In addition, our selection criteria require the detection of each source on the rise to peak, which further limits the sample of fast-evolving Ca-rich transients relative to the slow-rising SNe Ia. A true estimate of the volumetric rate of Ca-rich gap transients thus requires a simulation of the cadence of the ZTF survey together with the characteristic luminosity evolution of a Ca-rich gap transient to be able to estimate the number of sources that pass our light-curve selection criteria as a function of the input volumetric rate.

5.2. Luminosity Function

We aim to derive the luminosity function of Ca-rich gap transients using the controlled sample of events from the CLU experiment. Due to the small number of events, we do not separate the spectroscopic subtypes discussed in this work when estimating luminosity functions and volumetric rates. In
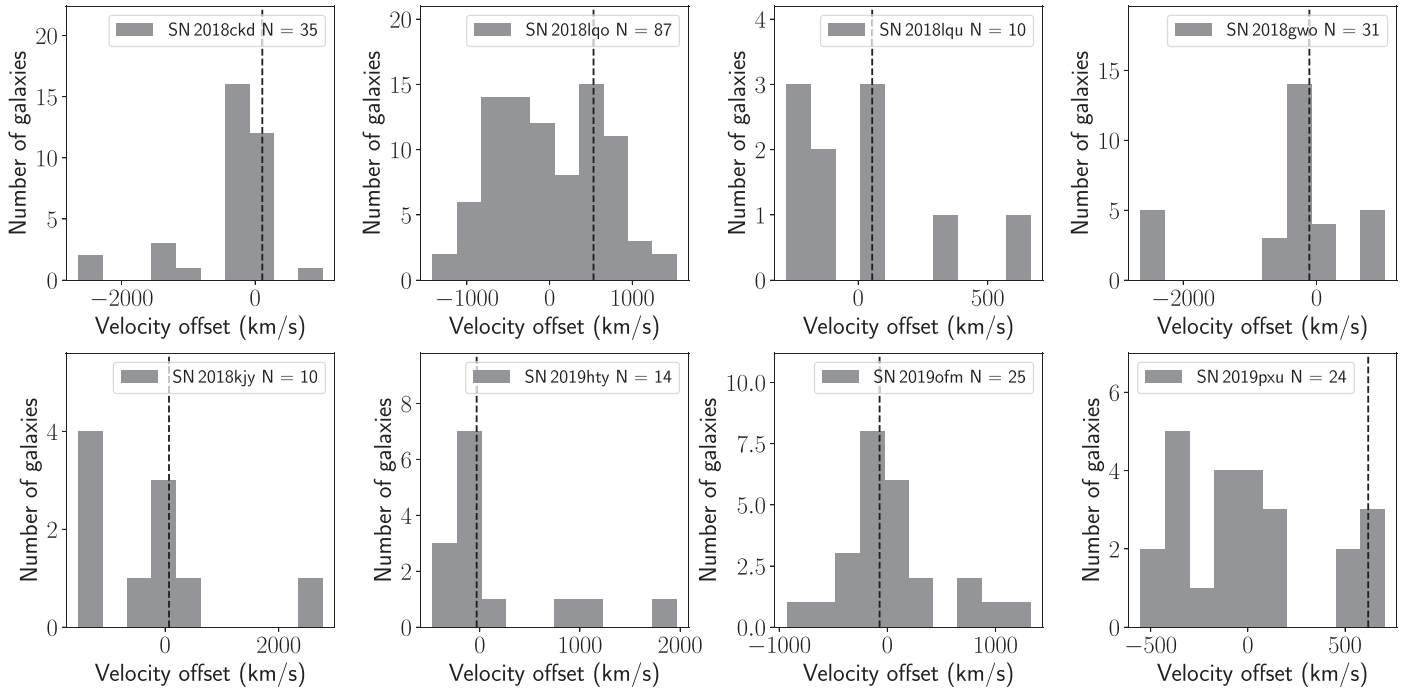
Figure 22. Velocity distributions of galaxies in the environments of the ZTF Ca-rich gap transient sample that have previously known spectroscopic redshifts in the CLU catalog. In each distribution, we define zero velocity as the median of the redshift distribution of all the galaxies in the projected vicinity of the transient, and show the velocity of the assumed (nearest) host galaxy of the transient with a dashed line. The transient name and number of galaxies in each histogram are indicated in the legend.

Figure 23, we show the observed histograms of the peak r-band magnitudes of the literature sample of Ca-rich objects and the ZTF sample of objects. The majority of the literature events exhibit peak magnitudes between $M = -16.5$ mag and $M = -15.5$ mag, while the ZTF sample shows a near-uniform distribution between $M = -17$ mag and $M = -15.5$ mag. However, it is difficult to quantify the selection biases when combining the literature sample of events with the ZTF sample due to the diverse selection criteria of the surveys that detected the literature objects. In order to derive an unbiased luminosity function, we focus specifically on the ZTF sample of events. Despite being classified as part of the CLU experiment, most of the objects in the ZTF sample are not luminous enough to be detectable across the entire experiment volume (200 Mpc) for a limiting magnitude of $r = 20$ mag, and thus volume correction needs to be applied to recover the true luminosity function.

We show a VCLF histogram of the ZTF Ca-rich sample in Figure 23. For each object, we apply a volume correction of $\frac{1}{V_{\max}}$, where $V_{\max}$ is the maximum volume out to which the object would be detectable for a limiting magnitude of 20. For sources that would be detectable at >200 Mpc, we set the relevant volume to 200 Mpc given the volume-limited nature of the experiment. The VCLF shows evidence of an increasing number of events down to the faintest event, and a simple linear polynomial describes the VCLF well. It is difficult to constrain the luminosity function below the faintest observed events, since it is unclear if there is a population of fainter events which would be detectable only within a very small volume (<100 Mpc). Hence, for the purpose of the simulations, we restrict the observed function between $M = -17$ mag (the upper luminosity limit for our sample) and $M = -15.3$ mag (of the faintest observed event, SN 2012hn). We caution that the ZTF CLU experiment is not sensitive to transients brighter than
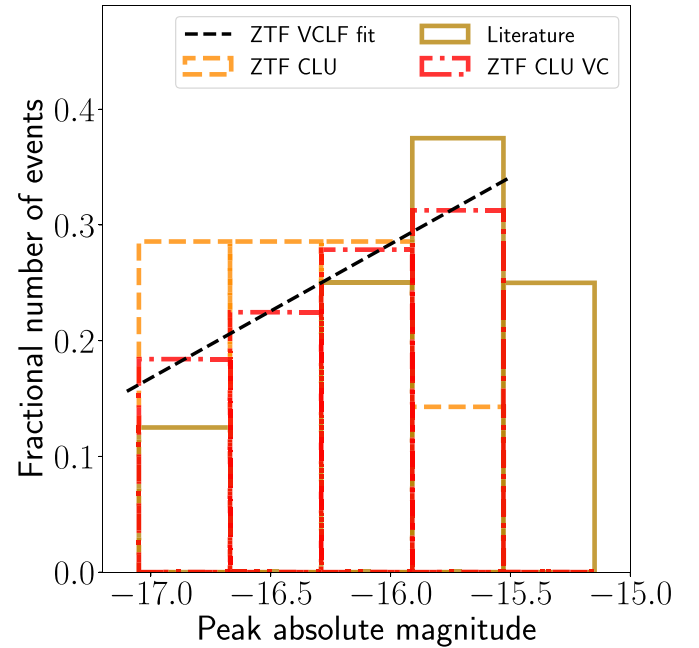
Figure 23. Peak r-band absolute magnitude distribution of the literature sample of Ca-rich gap transients (gold solid) and the ZTF sample (orange dashed). The dotted–dashed distribution in red shows the volume-corrected luminosity function (VCLF) of the ZTF sample, where a $\frac{1}{V_{\max}}$ weighting is applied, with $V_{\max}$ being the maximum volume out to which the transient would be detected by the volume-limited experiment. The black dashed line shows a linear fit to the VCLF.

$M = -17$ mag at peak due to the sample selection criteria, if such a population exists. Our rate estimates are thus limited to events peaking at $-15.3 > M > -17$.
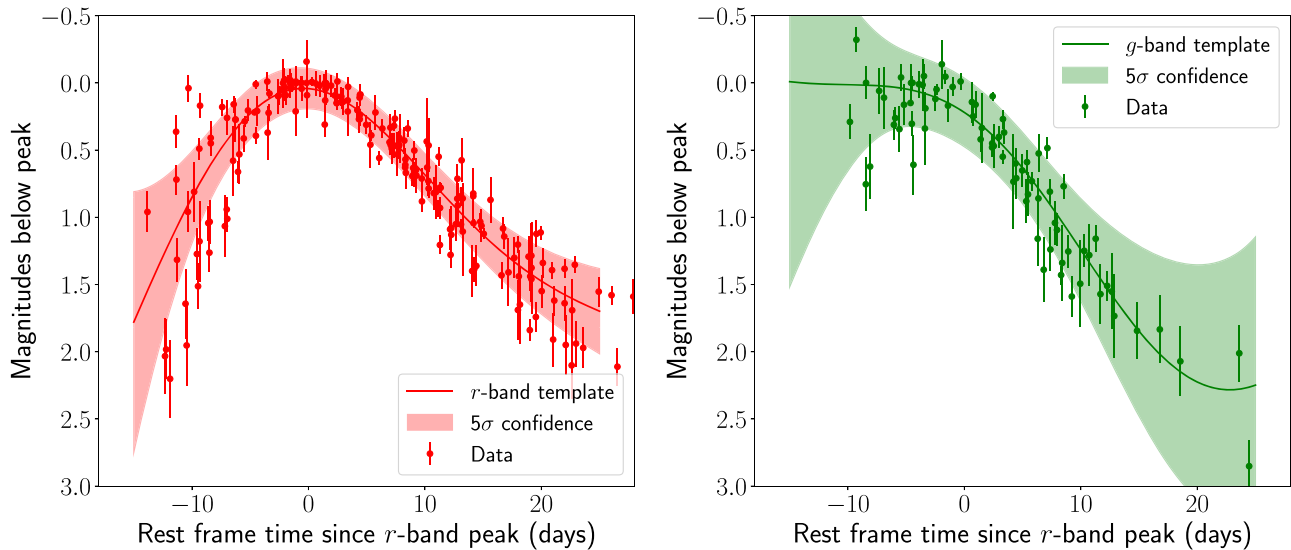
Figure 24. *r*-band and *g*-band light-curve templates for Ca-rich gap transients, normalized to peak magnitude. The points with error bars show the observed light curves with 1σ error bars in the respective filters while the solid lines indicate the best-fit light curve from Gaussian process fitting. The shaded regions indicate the uncertainty intervals derived from the Gaussian process fitting, corresponding to 5σ confidence regions.

5.3. Template Light Curve for a Ca-rich Gap Transient

In order to provide a more robust estimate of the volumetric rates of Ca-rich gap transients, accounting for their low-luminosity light curves and the ZTF survey cadence, we start by constructing a template light curve of a Ca-rich gap transient in the *r* and *g* bands (which have the most photometric coverage) using the data available for the events in the combined sample. Since we are interested in the photometric evolution timescale of each event, we first normalize each light curve by its peak magnitude measured in the respective filter. Time is measured with respect to the best-fit *r*-band peak time. We then fit a Gaussian process model with a constant kernel to the normalized light curves in each filter to construct a normalized light-curve template in the *r* and *g* filters.

We perform the fit in the phase space of magnitude versus time ranging from -15 days before the *r*-band peak to $+25$ days after the *r*-band peak, where there is photometric coverage for more than one object in both filters. This produces the average peak-normalized template light curve and its uncertainty as a function of phase from the *r*-band maximum. We do not include photometry upper limits in the fit. In Figure 24, we show the peak-normalized data and best-fit templates together with their uncertainties for the two filters. In particular, we note that the sample of peak-normalized light curves in both filters is fairly homogeneous around peak light (even though there is a dispersion in the peak magnitudes), suggesting that a single light-curve template normalized to peak magnitude can well capture the shape of the light curve.

5.4. Simulations of the ZTF Survey

Using the derived luminosity function and light-curve templates for the class of Ca-rich gap transients, we estimate their volumetric rates in the local universe using the `simsurvey` code (Feindt et al. 2019). `simsurvey` is capable of simulating transient light curves as would be observed by ZTF for a given input SN template (provided using the `sncosmo` package from Barbary et al. 2016), and an input survey tiling pattern and duration (termed a survey plan). We use the best-fit *r*- and *g*-band templates to construct a

`TimeSeriesSource` model in the `sncosmo` package to simulate the spectral evolution of a Ca-rich gap transient between 15 days before and 25 days after the *r*-band peak. We then use the actual ZTF observing history between 2018 June 1 and 2019 September 30 in any of the public or collaboration surveys as the input survey plan. Since the ZTF reference images were created shortly before the start of the survey and extended well into the time period discussed here for some fields, we only consider pointings that were acquired at least 60 days after the end of reference creation to avoid contamination of the reference images by transient light.

We then simulate the ZTF light curves of the Ca-rich gap transients for a range of input volumetric rates, performing 100 simulations of the ZTF observing plan for each input rate. Based on the observed VCLF, we fix the peak absolute magnitude distribution of the injected transients to a linear function between $M = -15.3$ mag and $M = -17$ mag in the *r* band. We assume a color of $g - r = 0.7$ mag at the *r*-band peak (based on the observed color evolution of the sample). Transients are injected out to a redshift of $z = 0.05$. In order to select transient candidates that would have passed the selection criteria defined in this experiment, we perform quality cuts on the simulated light curves as follows:

1. At least two detections of the source are required above an S/N of 5 in either the $g_{\rm ZTF}$ or $r_{\rm ZTF}$ filter.
2. The peak detected magnitude of the transient should be $m < 20$ in either the $g_{\rm ZTF}$ or $r_{\rm ZTF}$ filter.
3. The transient is observed before peak such that there is at least one detection with S/N > 5 before the peak of the light curve in either the $g_{\rm ZTF}$ or $r_{\rm ZTF}$ filter.

Applying these selection criteria to the sample presented in this paper, all but SN 2018gwo, which was recovered after peak light, satisfy the criteria. We use the average number of transients qualifying for these cuts as the best estimate of the number of detected transients for each input volumetric rate, while the standard deviation of the number detected in the simulations is taken as the uncertainty. We show the expected number of detected transients as a function of the input volumetric rate in Figure 25. Figure 25 also shows the fraction
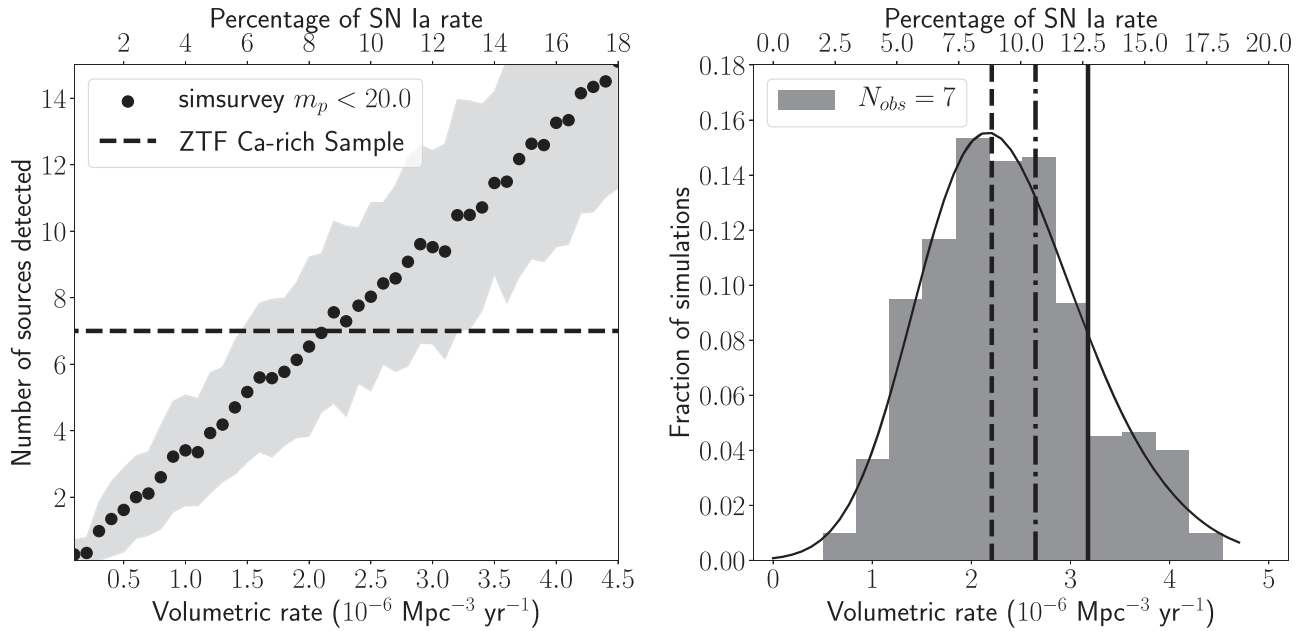
Figure 25. Estimate of the volumetric rate of Ca-rich gap transients with simulations of the ZTF survey using the `simsurvey` code. (Left panel) We show the number of sources passing our selection criteria for the CLU experiment as a function of the input volumetric rate (see text). The points and error bars are the mean and standard deviation of the number of transients recovered as a function of the volumetric rate, while the dashed black line shows the observed number of sources in the experiment. (Right panel) The fraction of simulations producing the observed number of transients as a function of the input volumetric rate. The dependence is fit with a skewed Gaussian distribution shown by the solid line, which we use to derive the best estimate of the volumetric rate and its confidence interval (see text). The dashed line shows the mean of the distribution, the dotted–dashed line shows the rate after correcting for galaxy catalog incompleteness, and the solid line shows the rate estimate after accounting for the transients missed beyond 100″ from their host galaxies.

of simulations that produce the observed number of transients as a function of the input volumetric rate.

Note that `simsurvey` is designed to inject simulated transients over the entire sky for a given input volumetric rate, while the CLU experiment is restricted to transients coincident within 100″ of galaxies with known spectroscopic redshifts. Hence we denote the `simsurvey`-derived rate as $r_{\mathrm{Ca,u,o}}$ with the u subscript indicating "uncorrected for the galaxy catalog completeness," and o indicating "uncorrected for offset distribution." The distribution of the fraction of simulations (Figure 25) is well described by a skewed Gaussian function and we fit the fraction of simulations with this functional form to derive the best estimate of the volumetric rate and its 68% confidence interval (similar to the procedure adopted by Frohmaier et al. 2018). We find a volumetric rate of

$$r_{\mathrm{Ca,u,o}} = (2.21^{+1.01}_{-0.67}) \times 10^{-6} \, \mathrm{Mpc}^{-3} \, \mathrm{yr}^{-1}. \tag{1}$$

Here, we quote the mode of the probability distribution in Figure 25 as the most likely rate, while the median of the rate probability distribution is 2.40×10^{-6} Mpc^{-3} yr^{-1}. The uncertainty intervals correspond to the central 68% confidence region, bounded by the 15.86 and 84.15 percentiles of the derived distribution. The most likely rate corresponds to $\approx 9^{+4}_{-3}\%$ of the SN Ia rate in the local universe ($\approx 2.5 \times 10^{-5}$ Mpc^{-3} yr^{-1}; Frohmaier et al. 2019).

In order to estimate the effect of incompleteness of galaxy catalogs in our estimate of the volumetric rate, we use the estimated redshift completeness factor (RCF) from the ZTF BTS (Fremling et al. 2019) as a function of the Wide-field Infrared Survey Explorer W_1 (3.36 μm) magnitude and redshift of the host galaxies. Taking the observed distribution of the redshift z and W_1 absolute AB magnitude M_{W1} (as obtained from the `Tractor` catalogs described in Lang et al. 2016) of

the ZTF sample of Ca-rich gap transients, we weight each event by $\frac{1}{\mathrm{RCF}(M_{W1}, z)}$ for its host galaxy, and sum up over the sample of seven events relevant to the simulation. With this exercise, we find that the incompleteness of galaxy catalogs leads to an underestimation of the Ca-rich gap transient rate by $\approx 20\%$. Next, analyzing the full sample of 18 events, we find that 3 out of the 18 objects exhibit offsets larger than 100″ of their host galaxies, although we caution that it is hard to quantify the systematic biases associated with the literature events. Accounting for this effect would increase the inferred rate by another $\approx 20\%$. Adjusting for this incompleteness, we derive a rate of

$$r_{\mathrm{Ca}} = (3.19^{+1.45}_{-0.96}) \times 10^{-6} \, \mathrm{Mpc}^{-3} \, \mathrm{yr}^{-1} \tag{2}$$

which is $13^{+6}_{-4}\%$ of the volume-averaged SN Ia rate in the local volume.

Owing to the predominance of early-type hosts in this sample, we also compare this rate against the SN Ia rate in early-type galaxies. Li et al. (2011) report a luminosity function averaged SN Ia rate in early-type galaxies of ≈ 0.05 per 100 yr per 10^{10} L$_{\odot,K}$. Using the local K-band luminosity density in early-type galaxies (Kochanek et al. 2001), we find the corresponding volumetric rate of SNe Ia in early-type galaxies to be $\approx 1.1 \times 10^{-5}$ Mpc^{-3} yr^{-1}. Thus, the inferred rate of Ca-rich gap transients is $\approx 30\%$ of the volume-averaged SN Ia rate in early-type galaxies. We further note that the rate of SNe Ia in early-type galaxies in cluster environments (Mannucci et al. 2008) is $\approx 40\%$ lower than the volume-averaged rate per unit mass in Li et al. (2011). This suggests that the rate of Ca-rich gap transients in early-type galaxies in clusters (which is true for nearly all events in our sample) is nearly $\approx 50\%$ of the SN Ia rate in these environments.

However, we caution that this rate estimate is still strictly a lower limit as we do not include the detection efficiency of the ZTF image subtraction pipeline as a function of transient magnitude and underlying surface brightness. An accurate estimate of the true rate would require us to assign a probabilistic detection likelihood for each simulated detection, using measured detection efficiencies of the ZTF pipeline, which are currently not available. We thus proceed by taking the derived rate as the first measured lower limit to the volumetric rate of Ca-rich gap transients from a large systematic volume-limited experiment.

The derived rate is consistent with those estimated by Perets et al. (2010) from LOSS and Kasliwal et al. (2012) from PTF. Frohmaier et al. (2018) presented the first quantitative analysis of the volumetric rates of Ca-rich gap transients using three events reported by PTF, incorporating the detection efficiency of the PTF pipeline as a function of transient magnitude and background surface brightness. They inferred a rate that could be higher than the rate in this work, of ≈30%–90% of the SN Ia rate in the local universe, although their estimate had large error bars owing to the small number of three events in the PTF sample.

6. Discussion

In this paper, we present observations and analysis of eight new Ca-rich gap transients classified as a part of the ZTF CLU experiment, nearly doubling the sample of known events in the literature. In Section 3 we demonstrate that the ZTF sample shares several similarities to 10 events reported in the literature, while also increasing the diversity of several observed properties among the combined sample. Utilizing the systematic selection criteria of the ZTF sample, we present an analysis of the host environment properties (Section 4) and volumetric rates (Section 5) of the class. In this section, we gather all of these findings to discuss their constraints and implications on the progenitor channels for this class.

6.1. Spectroscopic Subclasses and Correlations

In Section 3, we note the existence of two classes of Ca-rich gap transients distinguished by their spectroscopic appearance at peak—Ca-Ib/c events and Ca-Ia events (see Table 6). We further find a possible continuum of peak light spectral characteristics within the Ca-Ib/c class, wherein the events evolve from green continua with strong P-Cygni features in the blue to events with featureless reddened continua at short ($\lesssim$5500 Å) wavelengths. While the Ca-Ia events are distinguished by their strong Si II features at peak light, we demonstrate a continuum in the peak light spectral features going from Ca-Ia to Ca-Ic to Ca-Ib events. We briefly summarize them here:

1. Ca-Ib/c objects with green continua show strong optical He I features, while events with redder continua show a continuum of strong to weak to no He lines in their peak spectra (Figure 7).
2. He line velocities in red Ca-Ib/c events ($\approx$7000 km s^{-1}) are lower than those observed in green Ca-Ib/c events, which show high photospheric velocities of $\approx$10,000 km s^{-1}.
3. Red Ca-Ib/c events exhibit slower-evolving light curves (as quantified by $t_{f,1/2}$) compared to green events, with a null hypothesis probability (that the two classes are drawn from the same underlying population of $t_{f,1/2}$) of <5%

Table 6
Primary Observational Differences between the Ca-Ia and Ca-Ib/c Objects, and Differences between the Green and Red Ca-Ib/c Objects

Observable	Ca-Ia	Ca-Ib/c Red	Ca-Ib/c Green
Si II?	strong	strong to weak	weak
He I?	no	weak to strong	strong
V (10^3 km s^{-1})	6–10 (8)	4–10 (7)	8–12 (10)
Blanketed?	yes	yes	no
M_p (mag)	−16.2–17	−15.3–16.7	−15.5–16.2
Δm_7 (mag)	0.4	0.3	0.5
$g - r$ (mag)	1.0	1.5	0.4
[Ca II]/[O I]	no [O I]	2.5–10 (4)	7–13 (10)

Note. The velocity row is indicated with V, and shows the range of observed peak velocities together with the typical value. The peak magnitude and [Ca II]/[O I] rows show the range of peak absolute magnitudes in the r band and [Ca II]/[O I] respectively.

(Figure 15). This dependence is corroborated by the $g - r$ color dependence of the photometric evolution (Δm_7) shown in Figure 16.
4. Red Ca-Ib/c events typically exhibit lower [Ca II]/[O I] than green Ca-Ib/c events (by a factor of $\approx$2) at similar phases when the transient spectrum becomes optically thin (Figure 12).
5. Ca-Ia events exhibit more luminous light curves (peak absolute magnitude $M \lesssim -16.5$) than the Ca-Ib/c class, and have red spectroscopic colors/line blanketing and slow photometric evolution similar to those of red Ca-Ib/c events (Figure 15).
6. Although the strong Si II line distinguishes Ca-Ia events from Ca-Ib/c events, there are striking similarities between Ca-Ia and Ca-Ib/c events with redder continua, and we find evidence of a continuum of Si II line strengths going from Ca-Ia to Ca-Ib/c events (Figure 9).

It is worth noting that even most Ca-Ib/c events exhibit weak but identifiable Si II lines blended with the nearby λ6678 He line (Section 3). We thus find evidence of a sequence in the Ca-rich gap transients going from Ca-Ia to red Ca-Ib/c to green Ca-Ib objects, suggesting a potential continuum of underlying explosion conditions and progenitor systems. We show the corresponding spectroscopic sequence in Figure 26, where we plot the peak light spectra of a few representative members of the Ca-Ia and Ca-Ib/c classes. In addition, we show the peak light spectrum of SN 1991bg (Filippenko et al. 1992), which shows several similarities to the Ca-Ia objects. Thus, the underlying cause of this continuum of spectroscopic appearance could provide a clue to the nature of these explosions. We tabulate and quantify the key observational differences between the different spectroscopic classes in Table 6. We now further this idea of a continuum of underlying progenitor systems as an explanation for the diversity observed in Ca-rich gap transients by probing physical explanations for this continuum.

6.2. Constraints on Ejecta Composition and Mixing

The suppression of flux and features at short wavelengths can be explained as an outcome of line blanketing along the line of sight from Fe-group material in the outer ejecta (e.g., Woosley & Weaver 1994; Nugent et al. 1997). Such features are often seen in peculiar thermonuclear SNe (De et al. 2019b), suggestive of Fe group–rich layers in the outer ejecta. The
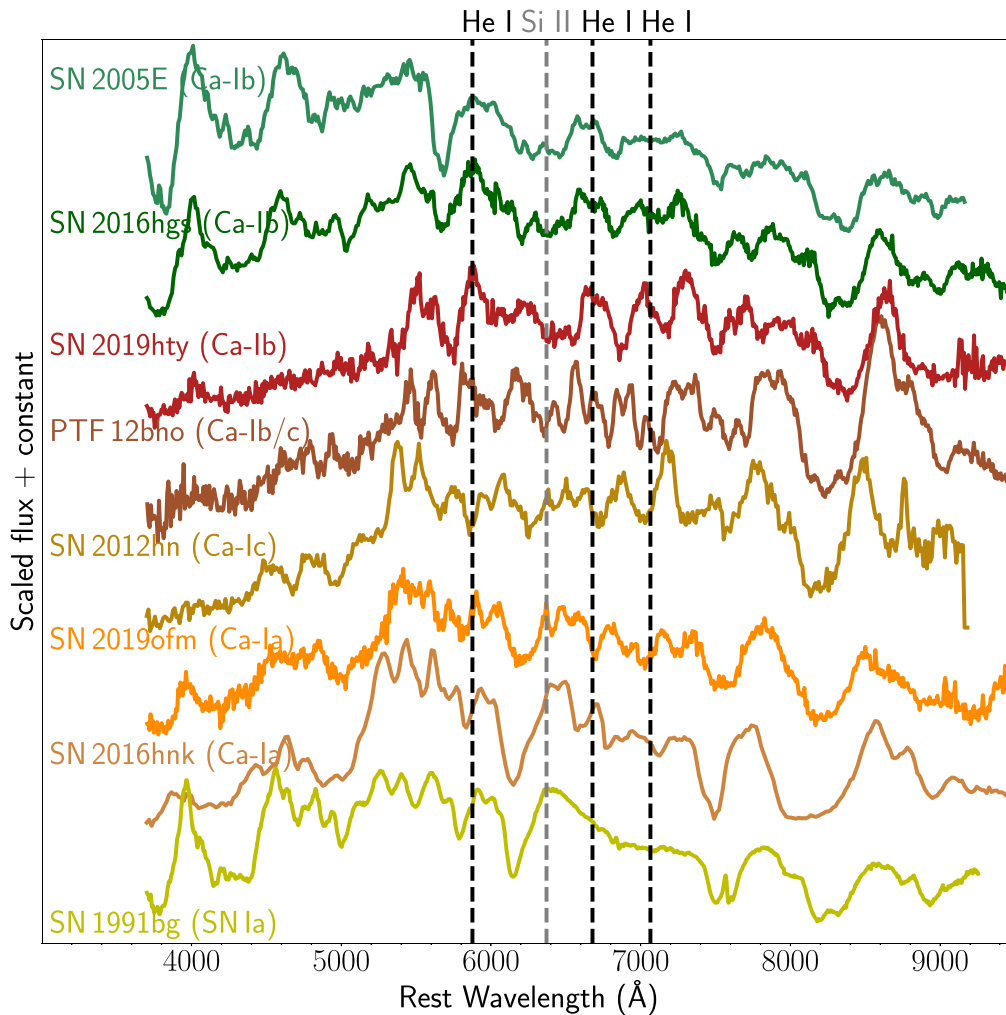
Figure 26. A continuum of spectroscopic and photometric properties in the sample of Ca-rich gap transients. For comparison, we also show the peak light spectrum of SN 1991bg, which shows striking similarities to the Ca-Ia objects. From bottom to top, we find a sequence of events that appear similar to SN Ia 91bg at peak (Ca-Ia events) with strong Si II lines, to SNe Ib/c at peak (Ca-Ib/c events) with weak He lines and line-blanketed continua, and to SNe Ib at peak (Ca-Ib events) with strong optical He I lines and no line blanketing. The colors reflect the photometric colors of the transient at peak. In general, going up the same sequence from bottom to top, the light curves become faster-evolving while the peak $g - r$ colors become bluer. The black dashed lines show the rest wavelength of the optical He I lines and the gray dashed line shows the position of the strong Si II line at $\approx$6360 Å. Note the increasing depth and higher velocity of the Ca II NIR triplet going from the Ca-Ib to the Ca-Ia events.

presence of such material is expected to produce redder colors in the transient (Nugent et al. 1997; Kromer et al. 2010; Polin et al. 2019a) while increasing the effective opacity of the ejecta due to an increase in bound–bound opacity from the Fe-group material. The increased opacity can also produce slower-evolving light curves if we assume that the underlying ejecta mass distribution is the same (see Figure 17; however, this is not expected to be dominant if the increased opacity is confined only to the outer layers of the ejecta).

The variety in the strengths and velocities of the optical He lines provides yet another clue to the underlying ejecta composition. Due to the high ionization temperature of He, the optical He lines may or may not be excited depending on the ejecta temperature and non-thermal excitation from radioactive material (Lucy 1991). Dessart et al. (2012) show that non-thermal excitation from the radioactive decay of ^{56}Ni is crucial for exciting optical He lines seen in the spectra of SNe Ib/c, thus suggesting that SN Ib/c classification may be related to the amount of ^{56}Ni mixing into the He layer instead of the actual He content of the ejecta (but see also Hachinger et al. 2012). While

highly mixed radioactive material in the He layer would produce strong optical He lines, it would also redden the transient color due to the presence of Fe-group material in the outer layers. However, we do not observe this trend in the Ca-rich sample—events with redder continua exhibit weaker (or no) He lines, suggesting a reduction in He content as the amount of Fe-group elements increase in the outer ejecta. In addition, unlike the massive cores in core-collapse SNe, the low optical depth for γ-rays in these low ejecta mass explosions (see De et al. 2018b for a discussion) makes it difficult to hide any non-thermal excitation of He.

While a continuum of Fe-group mass fractions in the outer ejecta appears to explain several of the observables, the reason for the existence of such a continuum remains unclear. This continuum could either be associated with a fundamental transition in the composition of the underlying ejecta, or be due to viewing angle effects. If the outer Fe-group material is produced from He burning in the outer ejecta, one could explain these observations as a continuum of He burning efficiencies in the outer ejecta, wherein the outer ejecta become

richer in Fe-group elements (which cause the line blanketing) as the He burning becomes more complete, thus leading to weaker He lines (see Townsley et al. 2012 for a recent work on the partial burning of He shells).

Nevertheless, it is important to note that the change in peak light continuum properties also appears to affect the appearance of the transient in the late-time nebular phase (its [Ca II]/[O I] ratio) when the ejecta are optically thin and viewing angle effects should be minimal. Both [Ca II] and [O I] are effective coolants of SN ejecta at late times (Fransson & Chevalier 1989) being powered by ^{56}Co decay in the case of normal core-collapse SNe. Together, these observations suggest that cooling in the inner ejecta becomes progressively dominated by [O I] as the outer ejecta become poorer in He content/richer in Fe-group content. Although not discussed thus far, Figure 26 also shows a continuum in the depth and velocity of the prominent Ca II NIR triplet, wherein the absorption becomes deeper and moves to higher velocity over this sequence. Since Ca is a known He burning product (Townsley et al. 2012), this evolution in the Ca II NIR triplet may be associated with the He burning sequence discussed here.

For completeness, we can rule out dust extinction as a possible cause of this evolution—while dust reddening can suppress red continua, it cannot explain the lack of blue-side SN ejecta features seen in the red Ca-Ib/c events. In addition, the remote locations of all of these events and the lack of detectable Na I D absorption in the spectra preclude host galaxy dust extinction.

6.3. Implications for the Explosion Mechanism

6.3.1. Models in the Literature

Shen et al. (2019) summarized the circumstantial evidence used to rule out several progenitor channels in the literature sample based on their environments, hosts, and volumetric rates. Owing to the striking similarities of the host demographics and environments of the ZTF sample and the literature events, our controlled experiment provides corroborating evidence for the preference of these transients for old environments. As in the literature sample, we find core-collapse SNe from massive stars as unlikely progenitor channels due to the prevalence of early-type hosts and large-offset locations with no signs of nearby star formation. On the other hand, the high inferred volumetric rates (lower limit of $\approx 15\%$ of the SN Ia rate) rule out progenitor channels with low expected volumetric rates such as He WD–neutron star mergers, where the field rate is $\sim 100\times$ lower (Toonen et al. 2018; see also Shen et al. 2019 for arguments against the viability of the high volumetric rates of these systems in globular clusters).

We thus consider the explosive burning of He shells on WDs as the strongest candidates for the cause of these events, and proceed by discussing the implications of our findings on the possible explosion conditions. Assuming that Ca-rich gap transients arise from He shell explosions on WDs, we aim to constrain variations in the underlying progenitor configurations and/or the burning mechanisms using the observed continuum of spectroscopic and photometric properties.

In the He shell detonation scenario, a shell of accreted He on the WD surface (accreted from an He-rich companion) can undergo dynamical burning for large shell masses, and detonate explosively to produce a thermonuclear transient (Iben et al. 1989;

Bildsten et al. 2007; Shen & Bildsten 2009; Woosley & Kasen 2011; Sim et al. 2012). Shen et al. (2010) presented calculations of the optical signatures of these events termed ".Ia" SNe, and Perets et al. (2010) suggested that the prototype Ca-rich transient SN 2005E is a result of such a detonation. However, the photometric evolution for the low ejecta mass ($\lesssim 0.2$ $M_\odot$) models presented in Shen et al. (2010) is substantially faster than that for SN 2005E, leading Perets et al. (2010) to suggest that more massive shells could explain the slower light-curve evolution.

Waldman et al. (2011) carried out explosive nucleosynthesis calculations of the shell detonation scenario with a 0.2 $M_\odot$ shell on a 0.45 $M_\odot$ CO WD, and demonstrated the nucleosynthesis of a large amount of intermediate-mass elements together with unburned He in the ejecta. Including non-thermal excitation effects, Dessart & Hillier (2015) showed that these events exhibit low-luminosity light curves, He spectroscopic signatures at peak light, and [Ca II] emission in the nebular phase, and are thus consistent with Ca-rich gap transients. Yet, the relatively slow light-curve evolution of most of the literature events requires even more massive shells ($\gtrsim 0.2$ $M_\odot$) than these calculations if the underlying core is not detonated. In particular, Dessart & Hillier (2015) showed that the ratio of [Ca II] to [O I] emission depends not only on their relative abundance, but also on where the γ-rays from late-time radioactive decay are being deposited, as these lines are primary coolants of the regions of ejecta where they exist. They further showed that the ejecta continue to cool predominantly through [Ca II] emission even if [O I] is present owing to the higher efficiency of [Ca II] cooling, thus pointing out the importance of the mixing of radioactive material as well as the Ca and O regions in determining [Ca II]/[O I] in the nebular phase (Fransson & Chevalier 1989).

Modifications to this scenario involving the detonation of the underlying CO core and the conditions required therefor have also been explored in the literature, first in the context of double-detonation models for SNe Ia (Nomoto 1980, 1982a, 1982b; Woosley et al. 1986; Woosley & Weaver 1994; Livne & Arnett 1995). These initial models invoked thick He shells (~ 0.1 $M_\odot$) for this scenario and were largely ruled out due to the predicted red colors and strong line blanketing signatures found for these configurations (e.g., Nugent et al. 1997).

Later studies found that thin He shells (as low as 0.01 $M_\odot$) on relatively massive CO cores ($\gtrsim 0.8$ $M_\odot$) can detonate the underlying WD (Bildsten et al. 2007; Fink et al. 2010; Shen et al. 2010; Shen & Moore 2014), potentially producing luminous slow-evolving transients akin to normal and sub-luminous SNe Ia (Kromer et al. 2010; Sim et al. 2010; Woosley & Kasen 2011; Polin et al. 2019a). Specifically, the slower-evolving light curves in these models may be consistent with Ca-rich gap transients; however, since the luminosity and timescale of these light curves increase with the underlying total mass (owing to higher Ni production from higher-density cores), Ca-rich gap transients are likely associated with explosions on lower-mass WDs in this scenario.

To this end, Sim et al. (2012) further extended these calculations to lowest-mass CO WDs (≈ 0.45 $M_\odot$) with thick He shells (0.2 $M_\odot$) specifically to probe the parameter space for subluminous and fast-evolving events like Ca-rich events. They found that secondary detonations are likely triggered for these shell masses (although there remain large uncertainties), and presented a suite of simulations varying the extent and

mechanism of the core detonation to demonstrate the corresponding effects on the nucleosynthetic signatures. They specifically noted that their suite of models produced transients brighter (peak absolute magnitude $\lesssim -17$) than the prototype SN 2005E, and thus reproducing the properties would require lower yields of radioactive material that could be possible in lower-density He shells (Shen & Bildsten 2009; Woosley & Kasen 2011) or via significant pollution of the shell with C (Kromer et al. 2010).

6.3.2. Ca-rich Gap Transients from He Shell Explosions

Jacobson-Galán et al. (2020) suggested that the Ca-Ia object SN 2016hnk is consistent with the detonation of a thin (≈ 0.02 $M_\odot$) He shell on a ≈ 0.8 $M_\odot$ WD. This interpretation is based on recent work by Polin et al. (2019b) showing that the ejecta in double-detonation events could cool predominantly through [Ca II] lines in the nebular phase (instead of Fe-group lines as in other SNe Ia) for low total (WD core + He shell) masses ($\lesssim 0.9$ $M_\odot$), even if the Ca abundance in the ejecta is of the order of a few percent. This channel thus provides a promising scenario to explain the origins of Ca-Ia objects, owing to their luminous and slow-evolving light curves, strong line blanketing signatures with SN Ia–like spectra, and [Ca II] emission in the nebular phase. The observed diversity in the peak luminosities could then be associated with a range of WD core masses.

Therefore, it is interesting to extend this mechanism to a continuum of He shell and CO core masses, which may explain the diversity in the population of Ca-Ib/c events with double detonations. Unlike pure shell detonations, which cannot fully explain the relatively slow-evolving light curves of prototypical Ca-rich transients like SN 2005E and SN 2010et (see, for example, Waldman et al. 2011 and Dessart & Hillier 2015), double detonations predict slower-evolving light curves compared to pure shell detonations due to the higher ejecta mass involved (Woosley & Kasen 2011; Sim et al. 2012). Considering that SN 2005E and SN 2010et belong to the class of green Ca-Ib/c events, which have faster-evolving light curves, the problem of slow evolution is even worse for red Ca-Ib/c events, which exhibit slower light curves similar to Ca-Ia events (Figure 15), leading us to consider double detonations for the red Ca-Ib/c events.

Owing to the explosive burning of He-rich material, a common spectroscopic prediction of the He shell double-detonation scenario is a transient marked by strong line blanketing features of Fe-group material and Ti II (at early times when the photosphere is in the He detonation material), in addition to intermediate-mass elements produced from the core burning (Hoeflich & Khokhlov 1996; Nugent et al. 1997; Kromer et al. 2010; Woosley & Kasen 2011; Polin et al. 2019a; Holcomb et al. 2013). Such signatures are also found in pure shell and double detonations on lower-mass WDs (Dessart & Hillier 2015; Sim et al. 2012). While previous attempts to model green Ca-Ib/c objects (Dessart & Hillier 2015; Sim et al. 2012) have had difficulty accounting for the relatively blue colors of these transients at peak, the red colors, line blanketing, and slow evolution make the double-detonation channel an attractive possibility for red Ca-Ib/c events. The typically lower peak luminosity of red Ca-Ib/c events would then require detonations on lower-mass WDs compared to Ca-Ia events.

However, despite having unburned He in the ejecta (Townsley et al. 2012; Sim et al. 2012; Moore et al. 2013;

Polin et al. 2019a), existing works on double detonations do not demonstrate whether He I lines can be reproduced as observed. On the other hand, Si II lines are the most conspicuous spectral features in these models as seen in Ca-Ia objects. Red Ca-Ib/c events show weak but clear signatures of He, sometimes stronger than the Si II lines. We note that existing models have primarily explored this scenario with relatively higher-mass WDs ($\gtrsim 0.8$ $M_\odot$), and without including the non-thermal radiation effects required to excite He lines (Sim et al. 2012 explored lower-mass WDs but without non-thermal effects). Given the continuum of strong to weak He lines observed in the red Ca-Ib/c population, it is possible that these explosions constitute a range of shell burning efficiencies, and correspondingly He content in the ejecta depending on the pressure at the base of the shell at the time of ignition (Moore et al. 2013). Ca-Ia events would then represent the extreme end of this population where He is nearly completely burned to Fe-group elements.

In the nebular phase, red Ca-Ib/c objects often show strong [O I] emission, unlike Ca-Ia events. If both red Ca-Ib/c events and Ca-Ia events arise from double detonations but with different underlying WD masses, this provides observational evidence that core burning becomes less efficient as one moves toward smaller core masses. A possible explanation is core detonation transitioning from converging shock detonations in high-mass cores to edge-lit detonations (Nomoto 1982b; Livne & Glasner 1990, 1991) at the base of the shell for lower-mass WDs. Owing to the lower density of the core in edge-lit detonations, Sim et al. (2012) show that these explosions produce incomplete burning of the core (and thus lower Ni yields and fainter light curves) and larger amounts of O in the core, both consistent with the red Ca-Ib/c population. Alternatively, it is possible that a larger fraction of the Ni produced in the core detonation is convectively mixed into the O-rich regions of the ejecta for lower-mass WD cores, thus producing stronger [O I] emission in the nebular phase.

Ca-Ib/c objects with green continua pose several problems to the general double-detonation picture above, especially with regard to their bluer colors at peak without line blanketing signatures. The lack of these signatures suggests a scenario where the outer ejecta is not significantly enriched with Fe-group elements, while the strong He line signatures indicate low He burning efficiency. Taken together with their systematically faster-evolving light curves, these signatures likely point to a low-efficiency burning mechanism that ejects a small amount of material. Although pure He shell detonation scenarios also predict line-blanketed spectra (due to the abundance of Ti II near the photosphere; e.g., Waldman et al. 2011; Dessart & Hillier 2015), lower He burning efficiency has been shown to be achievable if the pressure at the base of the shell is lower (Perets et al. 2010; Moore et al. 2013). If so, the higher photospheric velocities, relatively fast photometric evolution, and weak [O I] emission in the nebular phase are consistent with the properties of green Ca Ib/c events (Waldman et al. 2011; Dessart & Hillier 2015). The relatively low peak luminosity of this group (Table 6) then translates to a lower amount of radioactive material synthesized in these shell-only explosions compared to double detonations.

Alternatively, such low-efficiency burning conditions may be achieved in pure shell deflagrations. The study of this mechanism is extremely limited at this time but Woosley & Kasen (2011) show that these explosions produce slowly

evolving subluminous light curves, but with low photospheric velocities (≈ 4000 km s^{-1}). However, that study was performed with 1D simulations, which are poorly suited for deflagrations, and future work is required to determine if higher velocities could be achieved to make this a plausible scenario.

We note that early excess emission has so far been clearly seen only in the green Ca-Ib/c objects SN 2016hgs and SN 2018lqo. If these explosions are indeed associated with He shell detonations or deflagrations, these observations suggest that the outer ejecta produced in the shell burning is enriched with short-lived isotopes (e.g., ^{48}Cr, ^{52}Fe, and ^{56}Ni with half-lives of 0.90 days, 0.35 days, and 6.07 days respectively), as has been found in previous simulations of the pure shell detonation scenario (Shen et al. 2010). Although the early bump in iPTF 16hgs is potentially consistent with a core-collapse explosion from a giant He star (e.g., Woosley 2019), the detection of this bump in SN 2018lqo in an old elliptical galaxy strongly precludes a core-collapse interpretation. Although most objects in the green Ca-Ib/c sample do not have well-sampled early-time light curves to detect this early emission, this phenomenon is clearly not ubiquitous in the Ca-Ib objects as demonstrated by the monotonic rise observed in the well-sampled early light curve of SN 2010et (Figure 13).

6.4. Implications for the Progenitor Stellar Populations

We have thus far discussed the implications of diversity in the photometric and spectroscopic properties of the Ca-rich gap transient population for the underlying explosion mechanism. Broadly, we find that the range of observed properties can be explained with scenarios involving explosive He burning on the surface of a CO WD. Specifically, the slowly evolving light curves of the Ca-Ia and red Ca-Ib/c objects are difficult to explain using scenarios involving pure shell detonations, and likely require relatively massive explosions that detonate the underlying core. On the other hand, the green Ca-Ib/c objects may be consistent with shell-only explosions with low He burning efficiency. We now extend this discussion to probe the implications of the environments of these transients for the inferred progenitors, i.e., WDs accreting He from a companion. As noted in several previous works, this population of transients is distinguished from other classes by a striking preference for large offsets from their passive host galaxies in predominantly group and cluster environments. These two trends generally point to old stellar populations with long delay times, and preclude channels that have a significant rate at short delay times ($\lesssim 1$ Gyr; Perets et al. 2010; Meng & Han 2015). We note that several objects in our combined sample (iPTF 16hgs, SN 2016hnk, and SN 2019ofm) are found in star-forming environments, suggesting that there is a small but likely non-zero contribution at short delay times as well.

The pathways of stellar evolution to explosive burning of He shells have been explored in several previous works (Nomoto 1982a; Woosley & Weaver 1994; Bildsten et al. 2007; Shen & Bildsten 2009; Brooks et al. 2015; Bauer et al. 2017), with tight B-type subdwarf + WD systems (Geier et al. 2013; Kupfer et al. 2017) and AM Canum Venaticorum (AM-CVn) binaries (Nelemans et al. 2004) being possible well-observed evolutionary stages prior to the detonation. The observed formation rate of stable accreting AM-CVn systems in the Milky Way is $\sim 1.3 \times 10^{-4}$ yr^{-1} (Roelofs et al. 2007; Carter et al. 2013) or $\sim 2\%$ of the SN Ia rate in Milky Way–like galaxies (Li et al. 2011). Bildsten et al. (2007) used this to estimate the rate of He

shell detonations to be 2%–6% of the SN Ia rate in E/S0 galaxies assuming all AM-CVns detonate in a last flash. This rate is ≈ 3–$7 \times$ lower than our lower-limit estimate for the volumetric rate of Ca-rich gap transients, and is thus likely to be inconsistent. However, we cannot rule out the scenario where the green Ca-Ib events of the Ca-rich continuum discussed here originate in these explosions.

Similar detonation conditions can also be achieved in the case of mergers of He WDs with CO WDs (e.g., Pakmor et al. 2013), where a variety of detonation conditions could be achieved depending on how the He layer settles on the surface of the more massive WD (Fryer et al. 2010; Dessart & Hillier 2015). The merger rate of He + CO WD binaries in the field for a Milky Way–like galaxy is $\sim 3 \times 10^{-3}$ yr^{-1} (Brown et al. 2016) or $\approx 10\%$ of the SN Ia rate, suggesting that most He + CO WD binaries end up merging to produce thermonuclear transients or stable long-lived remnants (e.g., R Coronae Borealis stars; Clayton 1996; Schwab 2019). The high rate of these mergers within Milky Way–like galaxies is however in contradiction with the preference for large-offset distributions (long delay times) of the Ca-rich gap transient population (Shen et al. 2019). The measured rate in the halo (Brown et al. 2016) is only $\sim 10\%$ of the rate within the galaxy ($\sim 1\%$ of the SN Ia rate) and hence inconsistent with our estimates for the Ca-rich transients that reside in or outside their host halos.

With population synthesis calculations, Meng & Han (2015) suggested that the relatively high rates and long delay times of the Ca-rich gap transient population could be consistent with double-WD binaries with a CO WD $\lesssim 0.6$ $M_\odot$ and an He WD $\lesssim 0.25$ $M_\odot$, specifically highlighting the low mass as a key aspect of the delay time extension. This is consistent with our suggestion of low-mass WDs being the progenitor population, but the observed halo population of He–CO WD mergers remains too rare to explain the high rate (Brown et al. 2016). The measured rates are high enough such that there is one Ca-rich gap transient for every three SNe Ia in early-type galaxies, suggesting that the progenitors must be nearly as common as the progenitors of SNe Ia.

Together, we find that the observed merger rates of WDs in He-rich accreting systems are too low in the field in the outskirts of galaxies to explain the high rates of Ca-rich gap transients. However, the interaction rate may be enhanced in dense stellar systems like globular clusters (see, e.g., Pfahl et al. 2009; Samsing et al. 2017). Although such stellar systems are not detected exactly at the positions of known Ca-rich gap transients (Lyman et al. 2014, 2016; Lunnan et al. 2017), Shen et al. (2019) suggest these transients could be produced from being kicked out due to dynamical interactions inside dense stellar systems in the outskirts. Yuan et al. (2013) and Shen et al. (2019) argue that the locations and host environments are consistent with the globular cluster scenario; however, we continue to find that the number of Ca-rich gap transients at small offsets is too small compared to the globular cluster offset distribution in Shen et al. (2019). Additionally, the preference for rich cluster environments is even more extreme than that for globular clusters and remains to be explained.

Based on our deep late-time imaging observations of the transient locations, we find in four out of eight cases evidence of faint and diffuse nearby or underlying stellar associations. We estimate the absolute magnitudes of these sources to be ≈ -9 mag to -11 mag at the redshift of the transient. A similar diffuse system was also detected in late-time imaging of

PTF 11kmb (Lunnan et al. 2017). While we caution that the chance coincidence probability of background galaxies at this depth is high, we speculate about the implications of these being associated with the transient itself. Specifically, a population of such faint and ultra-diffuse galaxies have been detected in low surface brightness imaging surveys (Abraham & van Dokkum 2014) in nearby clusters. These systems appear to exhibit an overabundance (by nearly an order of magnitude) of globular clusters as compared to the expected numbers for their luminosity (van Dokkum et al. 2017, 2016, 2018). Although work remains to be done to constrain the formation rate of double-WD binaries in such dense stellar systems, it is an intriguing possibility that the offset locations of Ca-rich gap transients may be due to an overabundance of globular clusters in ultra-diffuse galaxies within nearby galaxy groups and clusters.

While Shen et al. (2019) point out that a relatively large fraction of WDs in globular clusters could be required to explain the estimated rate in Frohmaier et al. (2018), our lower rate estimates may provide a more viable solution to the problem. The locations of these transients in early-type galaxies in predominantly rich cluster environments are indeed suggestive given that up to 30%–70% of stellar light may be in intra-cluster light in these environments (D'Souza et al. 2014; Perets 2014).

7. Summary

In this paper, we present the design and completeness of the CLU experiment of the ZTF, aimed at assembling a spectroscopically complete sample of transients in the local universe within 200 Mpc. With a total sample of 754 spectroscopically classified SNe, we present the first systematic search for Ca-rich gap transients. Using simple and systematic selection criteria, we identify a sample of 22 low-luminosity hydrogen-poor SNe as candidate Ca-rich gap transients from the first 16 months of operations, which are followed up with nebular-phase spectroscopy. We report the detection of eight Ca-rich gap transients in this sample, which we combine with the literature sample of 10 events that pass the same selection criteria. We perform the first systematic study of the spectroscopic and photometric properties of this sample and identify several trends and correlations that have implications for the underlying explosions and progenitor systems. Summarizing these correlations, we find the following:

1. Ca-rich gap transients broadly bifurcate into two classes based on their peak light spectroscopic similarity to SNe Ia (with strong Si II lines; Ca-Ia objects) and SNe Ib/c (without strong Si II lines; Ca-Ib/c objects).
2. Ca-Ib/c objects show a bimodal population in peak light spectral properties based on their spectroscopic behavior blueward of ≈ 5500 Å, wherein some events exhibit red continua and strong line blanketing of blue flux (Ca-Ib/c-red) while other events exhibit flat continua with clear P-Cygni absorption features of metals at short wavelengths (Ca-Ib/c-green). Ca-Ia objects always show line-blanketed spectra at peak.
3. Ca-Ia objects do not show any He lines, red Ca-Ib/c objects show a continuum from weak to strong He lines (velocity ≈ 7000 km s^{-1}), and green Ca-Ib/c objects always exhibit strong He lines at higher velocities of $\approx 10,000$ km s^{-1}.

4. Photometrically, red Ca-Ib/c events with line blanketing signatures exhibit redder colors at peak and slower-evolving light curves ($\Delta m_7 \approx 0.3$ mag) compared to green Ca-Ib/c events ($\Delta m_7 \approx 0.5$ mag), where Δm_7 is the decay of the r-band light curve in 7 days from peak light. Ca-Ia events also exhibit relatively slow photometric evolution compared to green Ca-Ib/c objects ($\Delta m_7 \approx 0.4$ mag).
5. Ca-Ia objects do not show [O I] in the nebular phase, while red Ca-Ib/c objects show stronger [O I] lines in the nebular phase relative to [Ca II] and green Ca-Ib/c objects show weaker [O I] lines (higher [Ca II]/[O I] flux ratios) relative to red Ca-Ib/c objects.
6. We find tentative evidence of a spectroscopic continuum of properties going from Ca-Ia to Ca-Ic to Ca-Ib objects, where Si II lines get weaker, He I lines get stronger, and line blanketing becomes less significant in the spectrum in moving along that sequence. Photometrically, the peak light colors get bluer while the light-curve evolution becomes faster along this sequence.

We find that these spectroscopic properties and the corresponding trends can be broadly explained in scenarios involving the explosive burning of He shells on low-mass WDs ($\lesssim 0.8$ $M_\odot$). The slowly evolving light curves and line-blanketed spectra of the Ca-Ia and red Ca-Ib/c events are consistent with scenarios involving the double detonation of He shells on low-mass WDs, where the efficiency of He burning in the outer ejecta is high. On the other hand, the strong He lines, higher velocities, and faster-evolving light curves of the green Ca-Ib/c events suggest lower ejecta mass explosions likely involving He shell–only detonations with low He burning efficiency or even deflagrations. While theoretical modeling of He shell explosions on low-mass WDs remains limited at this time, this data set together with the inferred correlations from the first systematic search for these explosions will be a useful benchmark for future modeling efforts.

The host environments of the sample are dominated by remote locations in the far outskirts of galaxies similar to what was found in previous studies, while the offset distribution is skewed toward large host offsets compared to that of globular clusters. The apparent host galaxies themselves are always found in rich group and cluster environments, and are likely an important clue to the progenitor channels. Using the systematic selection strategy of the experiment, together with the measured incompleteness of galaxy catalogs from the ZTF BTS, we infer the volumetric rates of these events to be at least $\approx 15\% \pm 5\%$ of the local SN Ia rate. While the explosion scenarios require WDs with He-rich donors, the observed rates of these systems are apparently too low in the field to explain their high volumetric rates. However, we note that the observed environments of these events in the outskirts of early-type galaxies in clusters are strikingly different from the Galactic disk. We speculate that the rich host environments, offset locations, and faint nearby diffuse stellar associations in some events may point to a contribution from dynamical interactions within ultra-diffuse stellar associations in galaxy clusters, which are found to be extremely rich in globular clusters (van Dokkum et al. 2016, 2017).

Our findings have broader implications for the population of thermonuclear SNe in the local universe. While the double-detonation scenario has been long proposed as a viable explosion-triggering mechanism for SNe Ia, the strong line
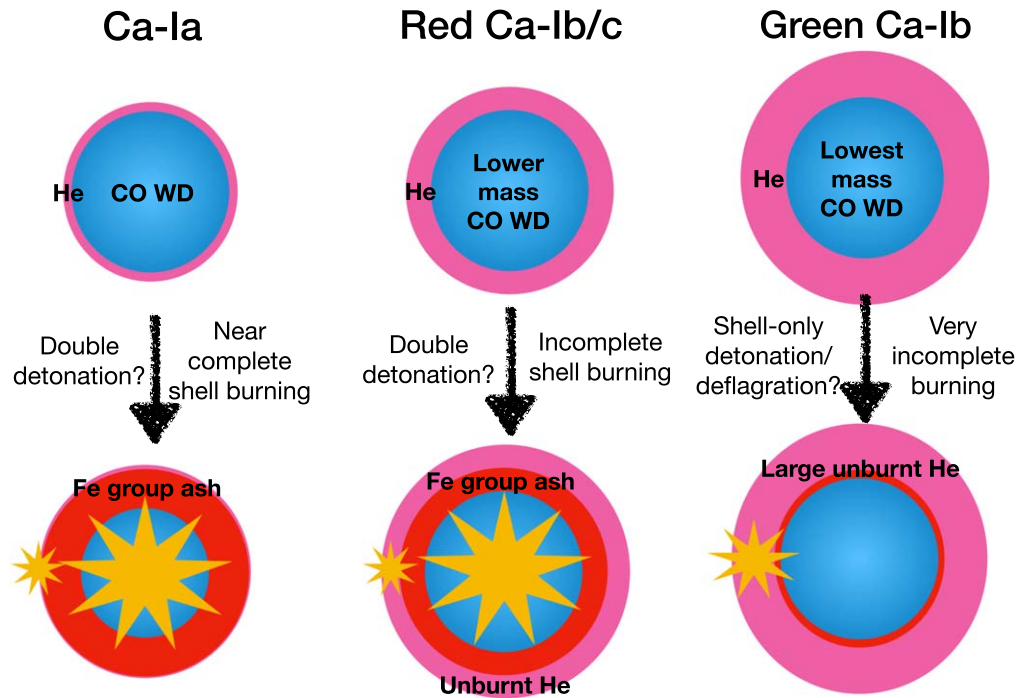
Figure 27. A cartoon schematic of a possible progenitor and explosion mechanism sequence in WD and He shell masses that may explain the diversity of properties of the population of Ca-rich gap transients. Double detonations (involving a detonation in the shell followed by a detonation in the core) with thin He shells and relatively massive WDs produce Ca-Ia objects, while double detonations on lower-mass WDs produce red Ca-Ib/c objects. Pure shell detonations or deflagrations (involving only a detonation or deflagration in the shell) could explain the incomplete burning and bluer spectra of green Ca-Ib objects.

blanketing signatures produced by Fe-group elements in the burning of the He shell have remained inconsistent for the broad population of normal SNe Ia (Hoeflich & Khokhlov 1996; Nugent et al. 1997; Kromer et al. 2010; Woosley & Kasen 2011; Polin et al. 2019a). However, recent discoveries of peculiar SNe such as SN 2016jhr (Jiang et al. 2017) and SN 2018byg (De et al. 2019b) show that thin and thick He shell double detonations may indeed be realized in nature but are intrinsically rare in the population. These transients are much more luminous at peak ($M \lesssim -18$) than the sample discussed here, consistent with the larger core masses ($\gtrsim 0.75\ M_\odot$) inferred for those objects. Ca-Ia objects are then lower-luminosity analogs of this family with relatively lower-mass WDs, while red Ca-Ib/c objects could be manifestations of He shell double detonations on the lowest-mass WDs. While it remains unclear if double detonations are realized for the lowest-mass WDs, green Ca-Ib/c objects could potentially be manifestations of "failed double detonations" of the lowest-mass WDs in the universe that do not burn much of the progenitor He shell.[36] We summarize this possible progenitor sequence within Ca-rich gap transients in Figure 27.

Given the fast-evolving light curves of Ca-rich gap transients, high-cadence and wide-field time-domain surveys will continue to be vital for unveiling large samples of these elusive events. With the combination of the flux-limited BTS (to estimate the redshift incompleteness of nearby galaxy catalogs; Fremling et al. 2019) and the volume-limited CLU experiment described in this work, we have demonstrated that focused experiments that spectroscopically classify a small fraction ($\lesssim 10\%$) of the total transient yield of a wide-field, all-sky survey like ZTF can yield statistically meaningful samples

of transients that shed vital light on the underlying explosions and progenitor populations. As the current effort has focused on a targeted search for these events in current (and incomplete) catalogs of nearby galaxies, the advent of heavily multiplexed spectrographs (e.g., DESI Collaboration et al. 2016; Kollmeier et al. 2017) aiming to complete galaxy catalogs in the local universe will be vital for dedicated experiments to complete our census of transients in the local universe.

---

[36] See also Kasliwal et al. (2010), Drout et al. (2011), and Inserra et al. (2015) for promising candidates for He shell–only detonation transients.

Appendix
Transients in the Control Sample

Here we discuss the photometric and spectroscopic properties of the transients that pass the selection criteria for follow-up but do not exhibit high [Ca II]/[O I] ratios in their nebular-phase spectra. We summarize the photometric and spectroscopic properties of these transients in Table 1. The control sample consists of four SNe Ib, five SNe Ic, one SN Ic-BL, two SNe Ib/c, and three SNe Ia. Figure 28 shows the forced-photometry light curves of these transients, while Figure 29 shows a collage of the spectroscopic data for each object. The complete log of the spectroscopic follow-up for these objects is presented in Table 3, which will be released on WISeREP together with the photometry upon publication. We plot the original reduced spectra for the spectroscopy epochs near peak light for each object. For the nebular-phase spectra, we show the original reduced spectra for events that do not have large host contamination. For other nebular spectra, we attempt to fit a polynomial to the underlying host continuum to subtract the host features and show the subtracted spectrum to highlight the broad nebular emission features of [O I] and [Ca II]. In cases where the host background is not smooth and has features sharper than ≈1000 Å (usually the case for S0/E-type galaxies) such that the nebular emission features are not easily measurable, we attempt more careful host subtraction using superfit (Howell et al. 2005). In these cases, the spectrum figures show the unsubtracted spectra, and the superfit-subtracted spectra are shown in Figure 30.

In addition to the objects discussed here, we note the case of the peculiar SN 2019ehk in the galaxy M100. SN 2019ehk was reported to the TNS by Grzegorzek (2019) and an early spectrum was reported by Dimitriadis et al. (2019), which exhibited a reddened featureless continuum with "flash"-ionized lines (see, e.g., Gal-Yam et al. 2014) of He II λ4686 and Hα. We obtained follow-up spectra of the event near peak light with DBSP, which show a reddened continuum with strong photospheric He absorption features and weaker H features, similar to Type IIb SNe. Specifically, the peak light spectra show signatures of Hβ and Hγ absorption together with a flat-bottomed feature near Hα blended with the nearby He I λ6678 line. The flat-bottomed Hα feature is characteristic of several well-studied SNe IIb like SN 2001ig (Silverman et al. 2009) and SN 2011dh (Marion et al. 2014). Curiously, this object shows strong [Ca II] lines in our early nebular-phase spectrum from SEDM and LRIS, similar to several Ca-rich transients in this sample. However, the clear presence of H in the early flash spectra and at peak light excludes it from our sample. Additionally, the deep Na I D absorption detected in its spectrum suggests significant host reddening by $A_V \gtrsim 3$ mag, making it intrinsically luminous ($M_p \lesssim -17$). This object may be similar to the Type IIb iPTF 15eqv, which exhibits high [Ca II]/[O I] in late-time spectra (Milisavljevic et al. 2017), and we defer the discussion of this object to future work.

A.1. Spectroscopic Classification

We summarize the detection, environment, and properties of each transient in the control sample, and particularly highlight how we exclude it from the group of Ca-rich gap transients. In
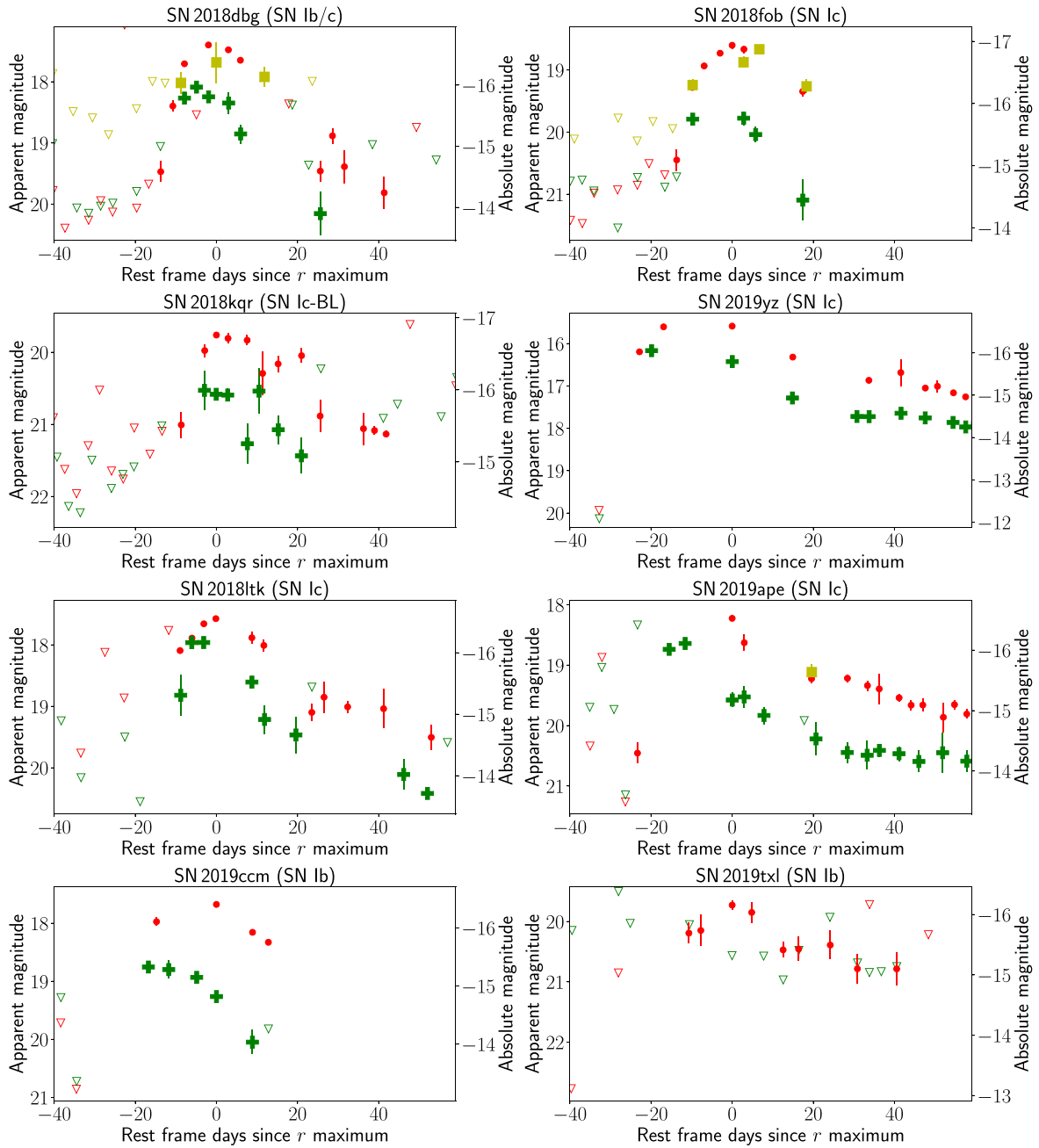
Figure 28. Forced-photometry light curves of each object in the control sample that does not pass the [Ca II]/[O I] threshold defined in the sample. Each panel shows the photometric evolution near peak for the transient indicated in the figure title. We include photometry in *gri* filters from ZTF and phase is defined with respect to time from the *r*-band peak. Red circles denote *r*-band photometry, green plus symbols indicate *g*-band photometry, and yellow squares indicate *i*-band photometry. Hollow inverted triangles denote 5σ upper limits at the location of the transient.

the next section, we use this discussion to compare the properties of these transients to those of the Ca-rich sample.

SN 2019ccm was found on top of the spiral arm of an Sa-type galaxy at $z = 0.015$ and peaked at an absolute magnitude of $M_r \approx -16.4$ mag (without correcting for its host extinction). A spectrum taken at peak light shows characteristic features of an SN Ib at peak on the red side (the blue-side spectrum was not recorded due to a readout issue on the LRIS detector), as well as a deep Na I D feature at the host redshift, suggesting that the low luminosity is partly due to host extinction. An LRIS spectrum taken ≈ 180 days after peak shows [O I] and [Ca II] emission of nearly equal strengths, ruling out a Ca-rich classification. We note that the [Ca II]/[O I] ratio (≈ 1.18) is

likely overestimated because the significant host extinction would only increase the observed ratio.

SN 2019txl was found on the arm of a spiral galaxy at $z = 0.034$ and peaked at an absolute magnitude of $M_r \approx -16.2$ mag. The peak light spectrum shows typical features of an SN Ib at peak, together with clear Na I D absorption at the host redshift, confirming it as a reddened normal SN Ib. A nebular-phase spectrum taken $\approx +330$ days from peak shows clear signatures of [O I] and [Ca II] emission with a [Ca II]/[O I] of ≈ 0.9 (without correcting for host extinction), thus excluding it from the Ca-rich sample.

SN 2019txt was found on the disk of a nearly edge-on disk galaxy at $z = 0.026$ and peaked at an absolute magnitude of
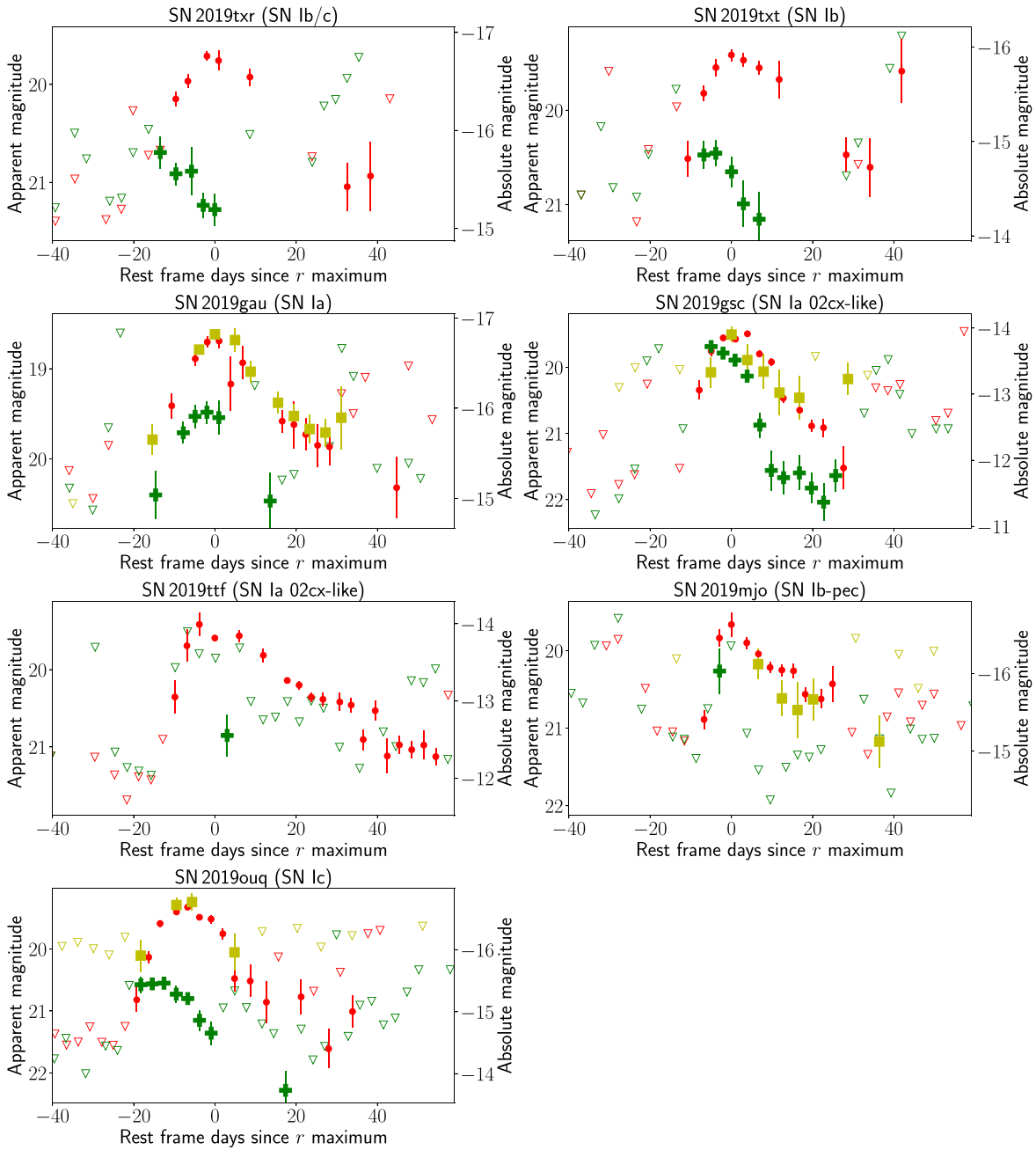
Figure 28. (Continued.)
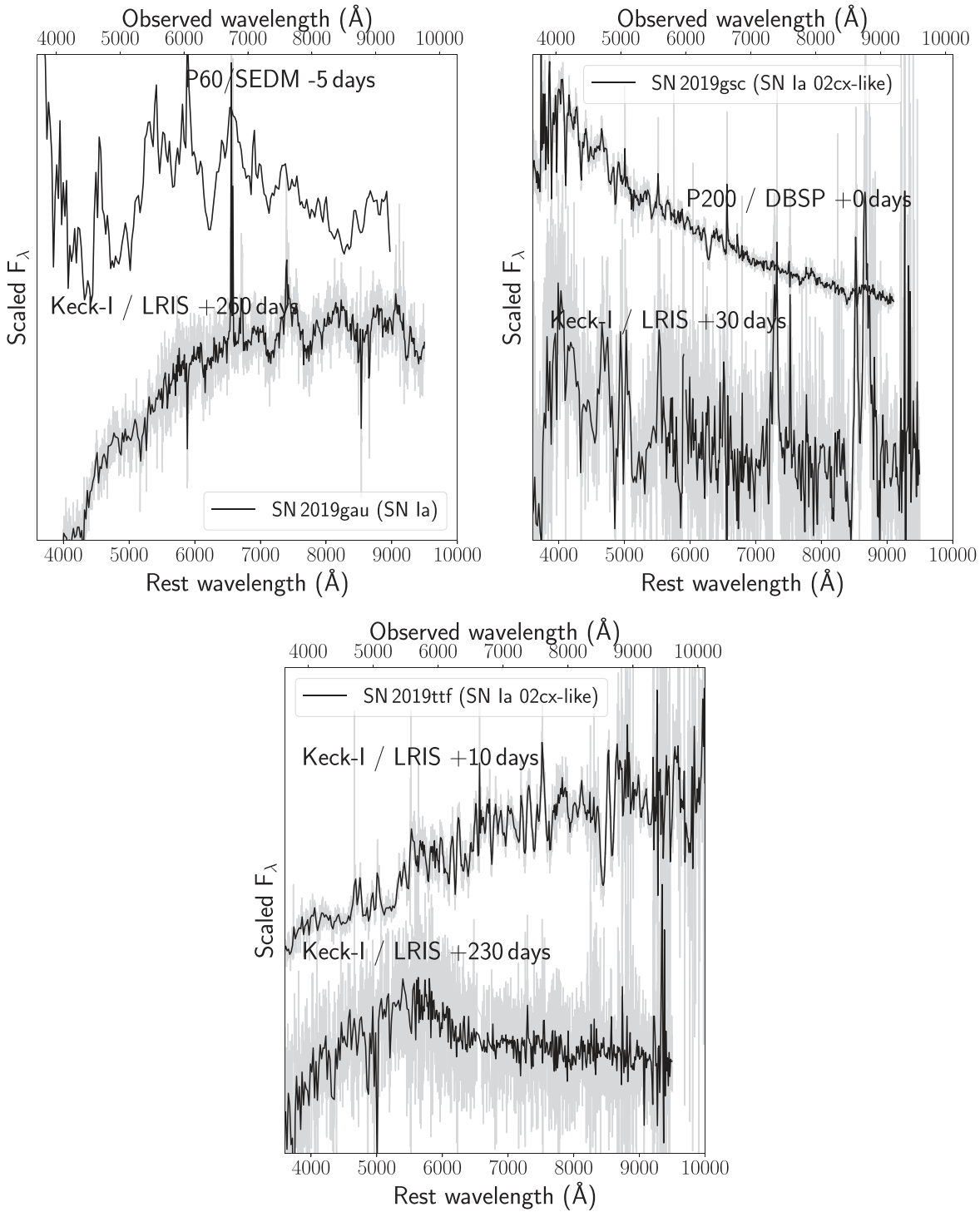
$M_r \approx -15.9$ mag. The peak light spectrum is relatively noisy but still clearly shows features of an SN Ib at peak, as well as prominent Na I D absorption at the host redshift, consistent with a reddened SN Ib. The nebular-phase spectrum at $\approx$220 days from peak light shows clear [O I] and [Ca II] emission with [Ca II]/[O I] of $\approx$1.3 without host extinction correction, thus excluding it from the Ca-rich sample.

SN 2019mjo stands out as a peculiar SN Ib found in the outskirts of an elliptical galaxy at $z \approx 0.041$. Its peak light spectrum is reddened with strong He lines and it exhibits a very slow transition in spectroscopic properties. The source does not turn nebular even in our latest spectrum at $\approx$+180 days from peak light, and hence does not satisfy our criterion for a fast nebular-phase transition. We defer conclusions about the nature

of this event to a forthcoming publication that will present the full data set on this source (K. De et al. 2020, in preparation).

SN 2018dbg was found close to the nucleus of a grand spiral host galaxy at $z \approx 0.015$, peaking at an absolute magnitude of $M_r \approx -16.6$ mag. We were unable to secure a peak light spectrum of SN 2018dbg, but secured a spectrum at $\approx$35 days after peak, where the spectrum was still dominated by strong photospheric-phase lines of O, Ca II, and possibly He I. Using superfit (Howell et al. 2005) to subtract the underlying continuum, we found an excellent match to the spectrum of the Type Ib SN 1990U at $\approx$+41 days after peak, consistent with the photometric phase ($\approx$+30 days). We thus classify it as an SN Ib/c. Since all Ca-rich gap transients start exhibiting strong nebular [Ca II] emission features at this phase, this object does
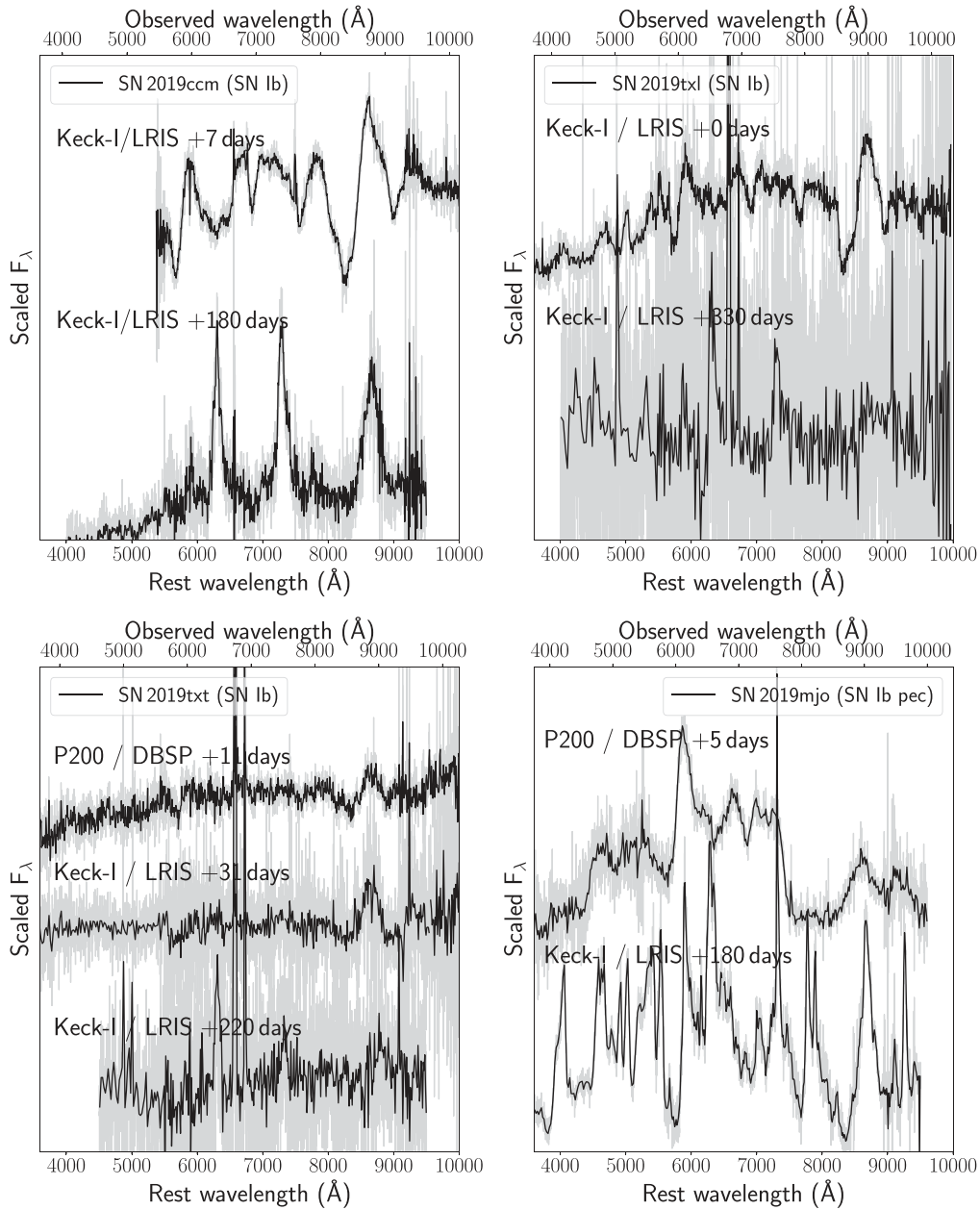
Figure 29. Photospheric- and nebular-phase spectra of objects in the control sample that do not pass either the early nebular-phase transition criterion or the nebular-phase [Ca II]/[O I] threshold defined in the sample (see Appendix). Each panel shows one object with its name and classification indicated in the legend. Gray lines show the unbinned spectra while black lines show the spectra binned to improve the S/N. The instrument used and the phase of each spectrum are shown next to each spectrum.

(The data used to create this figure are available.)

not satisfy our early nebular-phase transition criterion and is excluded from the sample.

SN 2019txr was found close to the nucleus of an irregular spiral galaxy at $z = 0.044$, and peaked at an absolute magnitude of $M_r \approx -16.7$ mag. The peak light spectrum is relatively noisy and we can only identify P-Cygni features of Ca II, O I, and possibly He I; however, we classify it as an SN Ib/c due to the uncertain identification of He I. We cannot identify any Na I D absorption due to the noisy nature of the spectrum. We obtained a nebular-phase spectrum at ≈ 270 days from peak, which we found to be dominated by host light. We visually identified a weak nebular emission peak around the

[O I] transition, but [Ca II] emission was not detected. We show a host-subtracted spectrum of the object matched with `superfit` with the Type Ib SN 2004gq ≈ 300 days after peak. Although the features are very weak, the host-subtracted spectrum shows the existence of a broad emission feature around [O I] and possible [Ca II]. Given the host-dominated spectrum, we were unable to measure [Ca II]/[O I], but used the detection of [O I] and the weak detection of the nearby [Ca II] line to constrain the [Ca II]/[O I] ratio to <1, excluding it from the Ca-rich sample.

SN 2018fob was found on the spiral arm of a disk galaxy at $z = 0.029$, and peaked at an absolute magnitude of
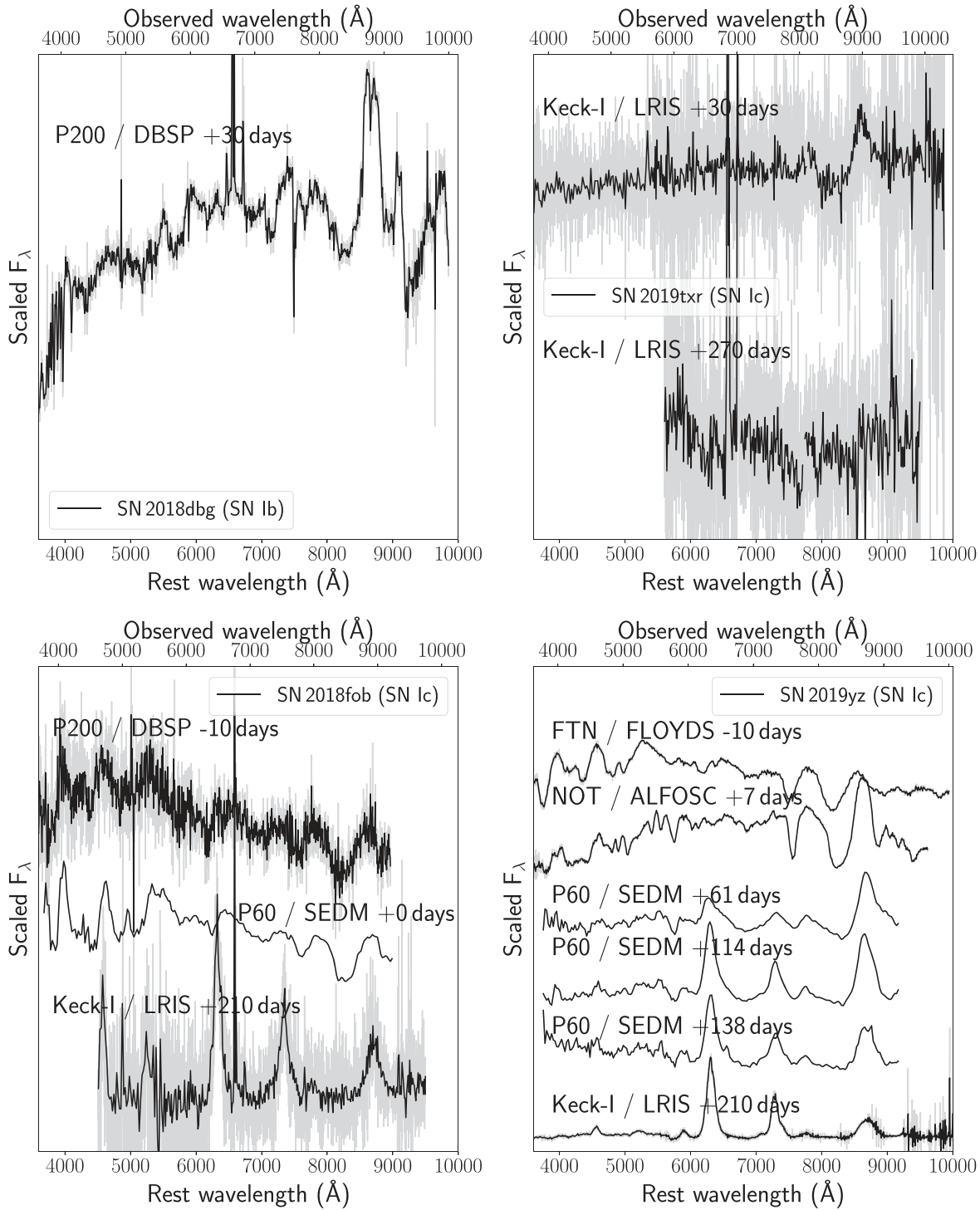
Figure 29. (Continued.)

$M_r \approx -16.9$ mag. The peak light spectra do not show any He signatures, and are consistent with an SN Ic. Na I D absorption is clearly detected at the host redshift, suggesting host extinction. The nebular-phase spectrum at ≈ 210 days shows a strong [O I] line and a weak [Ca II] line with [Ca II]/[O I] ≈ 0.87, thus excluding it from our sample.

SN 2019yz is the lowest-redshift object in this sample, and is consistent with a reddened SN Ic in the disk of UGC 09977 based on the prominent Na I D absorption in its peak light spectrum. The peak spectrum was obtained from the TNS and

was originally obtained by Burke et al. (2019). The light curve peaks at an observed absolute magnitude of $M_r \approx -16.63$ mag. The nebular-phase spectrum at $\approx +210$ days shows strong [O I] emission with [Ca II]/[O I] ≈ 0.6, excluding it from our sample of Ca-rich events.

SN 2019abb was found on top of an irregular blue galaxy at $z = 0.015$, and peaked at an absolute magnitude of $M_r \approx -16.6$ mag. The peak light spectrum shows characteristic features of an SN Ic with no obvious He signatures, as well as clear Na I D absorption at the host redshift suggesting
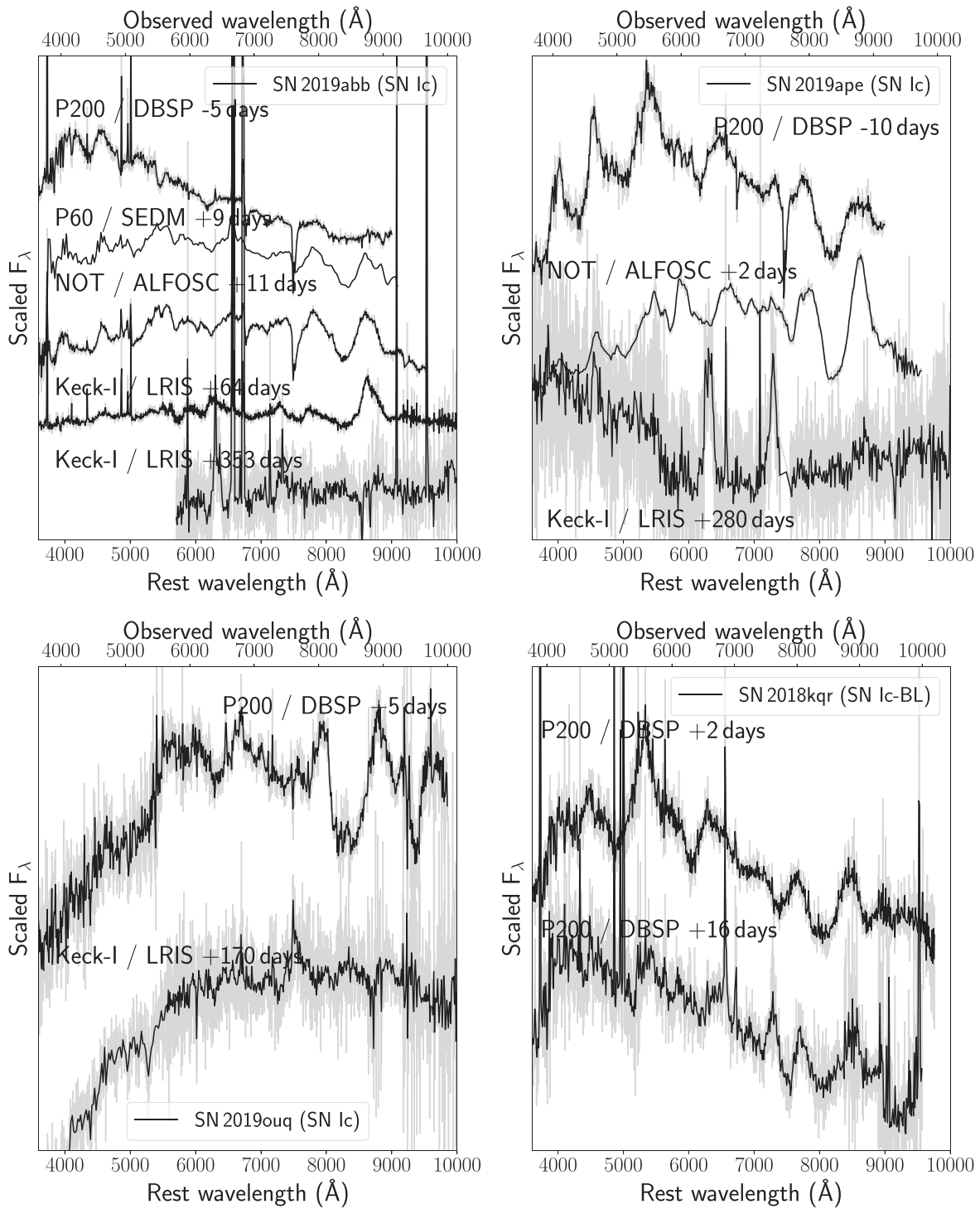
Figure 29. (Continued.)

significant host extinction. A spectrum taken ≈60 days after peak still shows photospheric-phase features suggesting slow spectral evolution. The nebular-phase spectrum obtained at ≈+350 days is dominated by the underlying host, but clearly shows both nebular [O I] and [Ca II] emission lines with [Ca II]/[O I] ≈ 0.8, thus excluding the object from our sample.

SN 2019ape was detected on top of a yellow early-type galaxy at $z = 0.020$, and peaked at an absolute magnitude of $M_r \approx -16.6$ mag. Although the galaxy morphology is early-type, the SDSS and SN spectra show clear Hα emission. The

peak light spectrum is characteristic of an SN Ic with no He signatures. Na I D absorption is also detected in the peak light spectrum, confirming host reddening. The nebular-phase spectrum taken at ≈+280 days shows clear [O I] and [Ca II] emission lines with [Ca II]/[O I] ≈ 0.9 thus excluding it from our sample. A complete analysis of this object will be presented in a forthcoming publication (I. Irani et al. 2020, in preparation).

SN 2019ouq was found in the disk of a nearly edge-on disk galaxy at $z = 0.036$, and peaked at an absolute magnitude of

Figure 29. (Continued.)

$M_r \approx -16.9$ mag. The peak light spectrum exhibits a highly reddened continuum but with clear broad P-Cygni features of O I and Ca II. Using `superfit` to subtract the host emission, we found that the peak spectrum is well matched to the Type Ic SN 1994I about 7 days after peak. The same fit suggests that an extinction of $A_V \approx 1$ mag is required to match the continuum. The nebular spectrum obtained at ≈ 170 days from maximum light is completely dominated by the underlying host galaxy continuum, making it difficult to identify the nebular [O I] and [Ca II] features directly. We thus used `superfit` to subtract the host features and show a host-subtracted spectrum in Figure 30. As shown, the nebular-phase spectrum is consistent with a late-time spectrum of the Type Ic SN 1997ef at ≈ 281 days. The host-subtracted late-time spectrum also shows similarities to the late-time spectra of the SNe Ic SN 2006aj and SN 1994I. In particular, the host-subtracted spectrum exhibits an [O I] line stronger than the [Ca II] line, constraining [Ca II]/[O I] $\lesssim 1$, thus excluding it from the Ca-rich sample.

SN 2018kqr was detected inside a blue irregular galaxy at $z = 0.045$, and peaked at an absolute magnitude of
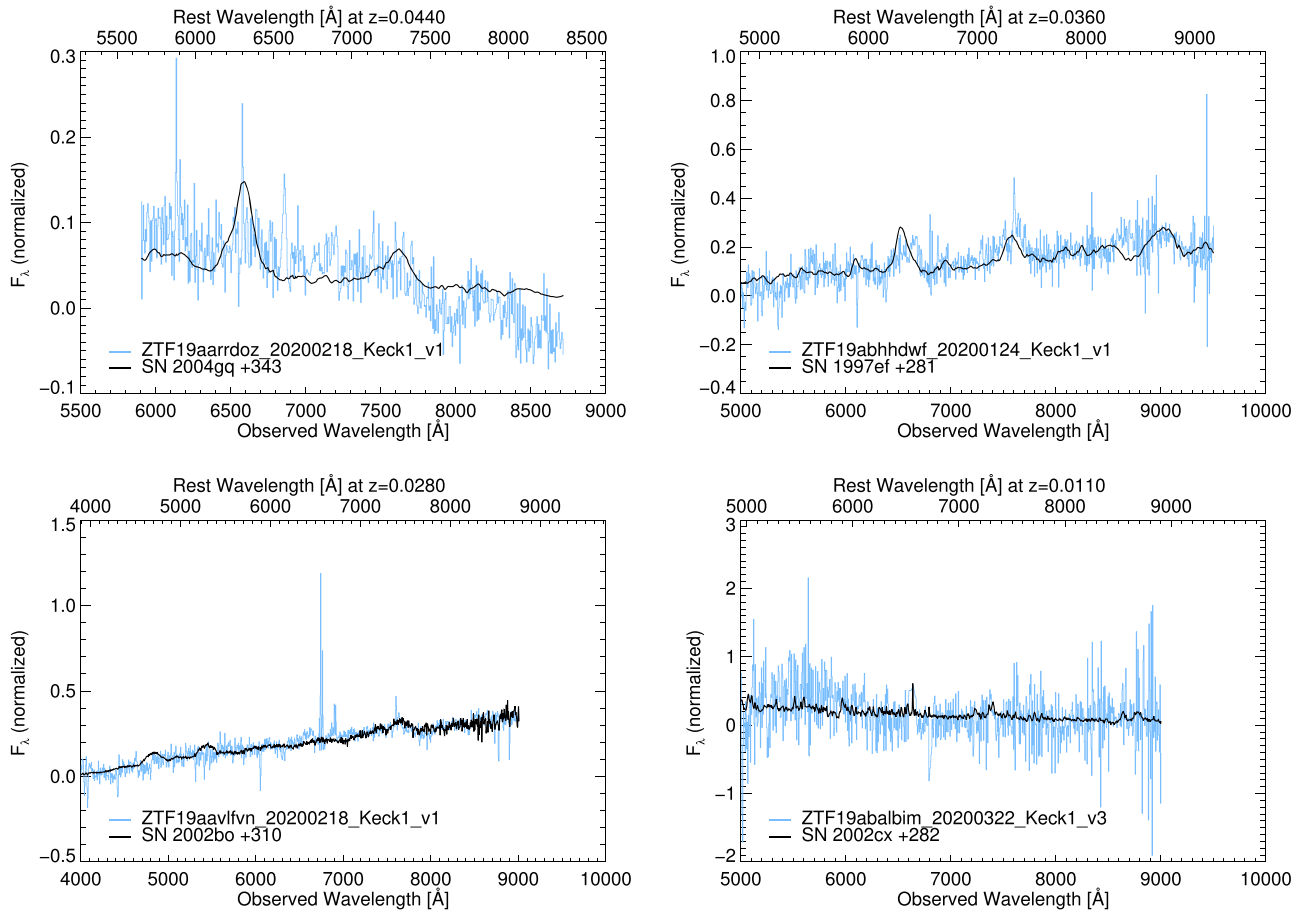
Figure 30. Host-subtracted late-time spectra of events in the sample that are heavily contaminated by host galaxy light and thus require host subtraction using `superfit` (Howell et al. 2005). (Top left) Late-time spectrum of SN 2019txr with host features subtracted using `superfit`. The observed host-subtracted spectrum is shown in blue, while the black line shows the best-match spectrum of the Type Ib SN 2004gq at 297 days after peak. (Top right) Late-time spectrum of SN 2019ouq plotted with the late-time spectrum of Type Ic SN 1997ef at ≈270 days after peak light. (Bottom left) Host-subtracted late-time spectrum of SN 2019gau at ≈270 days, compared against a late-time spectrum of the Type Ia SN 2002bo. However, we do not find a convincing match as several features in the subtracted spectrum are not well matched, and present the fit here for completeness. (Bottom right) Host-subtracted late-time spectrum of SN 2019ttf at ≈210 days compared to the late-time spectrum of SN 2002cx at ≈280 days.

$M_r \approx -16.8$ mag. The peak light spectrum shows broad features consistent with an SN Ic-BL around peak light. Na I D absorption is not clearly detected at the host redshift. We obtained a follow-up spectrum ≈16 days after peak light where the source still exhibits strong photospheric features consistent with an SN Ic. However, we were unable to obtain a follow-up nebular spectrum for this object. Nevertheless, the slow photospheric-phase evolution of this object is consistent with a normal SN Ic, and excludes it from the Ca-rich sample discussed in this work.

SN 2019gau was detected close to the core of a disk galaxy at $z = 0.028$, and peaked at an absolute magnitude of $M_r \approx -16.8$ mag. A low-resolution SEDM spectrum taken near peak shows a strong Si II line and the Ca II NIR triplet in P-Cygni absorption, leading to the SN Ia classification of this event. We obtained a late-time spectrum of the source at ≈260 days from peak, and found it to be dominated by the host galaxy light. We attempted host subtraction using `superfit`, but were unable to find a good match to the host-subtracted features. For completeness, we present the best-fit host-subtracted spectrum in Figure 30 compared to the best match in `superfit` to the late-time spectrum of SN 2002bo. Unlike Ca-Ia objects, which show strong [Ca II] emission and no [O I] emission, this host-subtracted spectrum does not show any

strong [Ca II] emission, leading us to exclude it from the Ca-rich sample.

SN 2019gsc was detected inside an irregular blue galaxy at $z = 0.011$, and peaked at a faint absolute magnitude of $M_r = -13.90$ mag. Its peak light spectrum exhibits low-velocity Si II lines similar to those of 02cx-like SNe Ia (Li et al. 2003), while its faint peak luminosity makes it similar to the lowest-luminosity member SN 2008ha (Foley et al. 2009). Our spectrum taken at ≈+30 days from peak is still photospheric and dominated by several low-velocity P-Cygni features. Additional data on SN 2019gsc has been published in Srivastav et al. (2020) and Tomasella et al. (2020), which show that the source does not turn nebular even up to ≈60 days from peak light, consistent with our data and with what is typically observed in this class (Foley et al. 2016). The absence of an early nebular-phase transition excludes it from the Ca-rich sample.

SN 2019ttf was found on top of an irregular star-forming galaxy at $z = 0.011$, and peaked at a faint absolute magnitude of $M_r = -14.0$ mag. The spectrum taken at ≈+10 days from peak shows low-velocity lines similar to those of the 02cx-like SNe Ia SN 2008ha (Foley et al. 2009) and SN 2005hk (Phillips et al. 2007). Its low peak luminosity is similar to that of SN 2019gsc. We obtained a late-time spectrum of the object at

≈230 days, which is dominated by the underlying host galaxy light. We show a host-subtracted spectrum using `superfit` in Figure 30. The subtracted spectrum is relatively noisy, but we note two detected features of Na I and [Ca II] (near 5800 Å and 7300 Å respectively) that are similar to those of SN 2002cx at a similar phase. As in the case of 02cx-like objects that do not become completely nebular at late times, we found a weak Na I P-Cygni profile, and thus exclude this object from the Ca-rich sample.

A.2. Candidate Selection and False Positives

In Section 2.3, we present our selection criteria for identifying candidate Ca-rich gap transients in order to prioritize nebular-phase follow-up. We now evaluate the merits and disadvantages of our selection scheme in the context of understanding the broader population of Ca-rich transients. We start with a comparison of our selection criteria to those of Kasliwal et al. (2012). Unlike that work, we did not select candidates based on their photometric evolution or spectroscopic velocities. This choice made us sensitive to events with broader light curves such as SN 2019pxu, which appears to be a more luminous and slower-evolving member of this class.

However, we did select events based on their peak luminosity, with a cutoff at $M = -17$ mag. We thus caution that certain spectroscopic subtypes may be underrepresented in this sample—e.g., the Ca-Ia events appear to exhibit systematically higher peak luminosity than the Ca-Ib/c events. Indeed, the only Ca-Ia object in the sample SN 2019ofm is also the faintest SN Ia in the CLU sample (barring the low-velocity 08ha-like events), suggesting that the Ca-Ia events discussed here could represent the tip of the Ca-rich sample in the broader 91bg-like SN Ia population. Resolving this issue would require a similar experiment targeting brighter SNe Ia, which will inevitably include other known populations of faint SNe Ia.

As in Kasliwal et al. (2012), we did not select events based on their spectroscopic type at peak light. However, the low spectroscopic velocities in SN 2018kjy would not have passed the criteria in Kasliwal et al. (2012) since they required "normal" photospheric-phase velocities. Our follow-up campaign revealed that despite its peculiar low spectroscopic velocities at peak, the later evolution of SN 2018kjy establishes its membership in the class of Ca-rich gap transients. In the context of low-velocity events, it is important to highlight the contamination of 02cx-like SNe Ia. Two of the events in the control sample are spectroscopically similar to 02cx-like objects near peak light (similar to SN 2008ha; Foley et al. 2009) with low spectroscopic velocities at peak (like SN 2018kjy). Yet unlike that of SN 2018kjy (and the rest of the Ca-rich class), their spectra do not turn nebular at late phases and exhibit a pseudo-continuum of emission lines.

Next, we discuss the host environments of these events, reiterating that our selection criteria are agnostic to the host type and environment. In comparison to the SNe Ib/c in the control sample (which were primarily found in star-forming late-type galaxies), a striking characteristic of the sample of Ca-Ib/c objects is their preference for early-type galaxies and old environments. SN 2019pxu is the only exception, but is still at a large projected offset of ≈18 kpc from its host, suggesting that spectroscopically classified SNe Ib/c in old environments could be used to select likely Ca-rich gap transients near peak

light. Yet, SN 2019ape serves as an important exception to this trend as an SN Ic in an early-type galaxy, suggesting that this criterion also has its own false positives despite producing a relatively high success rate (six out of seven SNe Ib/c in early-type galaxies in this sample turned out to be Ca-rich events). However, nearly all the low-luminosity SNe Ia in the sample (including two 02cx-like events) are in late-type galaxies—as such, the environment of the only Ca-Ia event in the sample SN 2019ofm is not exceptional.

In terms of the photometric and spectroscopic properties of the transients, the sample presented in this work was selected using the smallest possible selection criteria to identify these faint transients in the local universe. The final confirmation of a Ca-rich gap transient, however, was derived from nebular-phase spectroscopy at late times. As such, it is instructive to examine if the confirmed sample of Ca-rich gap transients can be differentiated based on the peak light spectra and photometric evolution in order to guide future searches for these events. In Figure 15, we show the luminosity–width phase space of the control sample of transients compared to the Ca-rich gap transients analyzed in this work. We make this comparison in order to examine if Ca-rich gap transients can be identified from their peak luminosity and light-curve evolution near peak. As shown, a striking trend is that the control sample of objects exhibit systematically slower-evolving light curves (smaller Δm_7 and longer $t_{f,1/2}$) than nearly the entire sample of Ca-rich gap transients, suggesting typically longer diffusion time and correspondingly larger ejecta masses in the control sample. Yet, the Ca-rich and control objects occupy a common phase space near $\Delta m_7 \approx 0.3$ and M_p between -16 and -17, meaning that the fastest-evolving objects in this sample are always Ca-rich. Thus, we conclude that while the fastest-evolving Ca-rich gap transients $\Delta m_7 > 0.4$ can be identified with peak light photometry and spectroscopy, it is difficult to select a complete sample based on only these properties.

The broader light curves and low [Ca II]/[O I] of the Type Ib/c events in the control sample suggest that these events are likely consistent with being normal core-collapse SNe (Gal-Yam 2017) that are extinguished by foreground dust. Indeed, the detection of prominent Na I D absorption from the host galaxy in nearly all of these events suggests that host extinction likely plays an important role in making these events appear subluminous at peak similar to Ca-rich events. The 02cx-like events (Li et al. 2003) are consistent with very low luminosity members of the SN Iax class similar to the lowest-luminosity member SN 2008ha (Foley et al. 2009). However, we did not have a high-resolution spectrum of the only other Type Ia SN 2019gau at peak to ascertain the role of host extinction. At the same time, we were unable to securely identify nebular emission features in the late-time spectrum of this object, leaving this as an inconclusive low-luminosity SN Ia in the sample.

We examined the spectroscopic properties of the control sample to identify potential spectroscopic clues at peak light for identifying Ca-rich gap transients. Ca-Ib exhibit spectra strikingly similar to those of normal SNe Ib in the sample; however, line-blanketed spectra of the red Ca-Ib objects are uncommon in the control sample. The only objects in the control sample that also exhibit suppressed blue continua are SN 2019txl and SN 2019mjo. The former object also exhibits strong Na I D absorption, suggesting that host extinction likely

suppresses the blue continuum in this otherwise normal core-collapse SN. SN 2019mjo is a peculiar SN Ib whose nature remains unclear, and we do not discuss its properties further here. Nevertheless, peculiar low-velocity objects such as SN 2018kjr and PTF 12bho are not seen in the control sample, suggesting that the combination of low velocity and a highly reddened continuum may be indicative of a Ca-rich object if its peak luminosity can be constrained. Ca-Ia objects with strongly line-blanketed spectra are unique in the broader population of SNe Ia that exhibit blue continua at peak (see the discussion in De et al. 2019b), and thus strong line blanketing with prominent Si II lines could be used to identify likely Ca-Ia candidates at peak. Given that all the above selection procedures were unable to yield a complete sample of Ca-rich gap transients, we conclude that in general nebular-phase spectroscopy of systematically selected samples of low-luminosity transients in the local universe with 8–10 m class telescopes will continue to be important for our census of these elusive transients.

ORCID iDs

Kishalay De https://orcid.org/0000-0002-8989-0542
Mansi M. Kasliwal https://orcid.org/0000-0002-5619-4938
Anastasios Tzanidakis https://orcid.org/0000-0003-0484-3331
U. Christoffer Fremling https://orcid.org/0000-0002-4223-103X
Robert Aloisi https://orcid.org/0000-0003-2822-616X
Igor Andreoni https://orcid.org/0000-0002-8977-1498
Eric C. Bellm https://orcid.org/0000-0001-8018-5348
David O. Cook https://orcid.org/0000-0002-6877-7655
Dmitry Duev https://orcid.org/0000-0001-5060-8733
Alison Dugas https://orcid.org/0000-0001-7344-0208
Sara Frederick https://orcid.org/0000-0001-9676-730X
Avishay Gal-Yam https://orcid.org/0000-0002-3653-5598
Daniel Goldstein https://orcid.org/0000-0003-3461-8661
V. Zach Golkhou https://orcid.org/0000-0001-8205-2506
Matthew J. Graham https://orcid.org/0000-0002-3168-0139
Matthew Hankins https://orcid.org/0000-0001-9315-8437
George Helou https://orcid.org/0000-0003-3367-3415
Anna Y. Q. Ho https://orcid.org/0000-0002-9017-3567
Ido Irani https://orcid.org/0000-0002-7996-8780
Jacob E. Jencson https://orcid.org/0000-0001-5754-4007
David L. Kaplan https://orcid.org/0000-0001-6295-2881
S. R. Kulkarni https://orcid.org/0000-0001-5390-8563
Thomas Kupfer https://orcid.org/0000-0002-6540-1484
Russ R. Laher https://orcid.org/0000-0003-2451-5482
Ragnhild Lunnan https://orcid.org/0000-0001-9454-4639
Frank J. Masci https://orcid.org/0000-0002-8532-9395
Adam A. Miller https://orcid.org/0000-0001-9515-478X
James D. Neill https://orcid.org/0000-0002-0466-1119
Eran O. Ofek https://orcid.org/0000-0002-6786-8774
Daniel A. Perley https://orcid.org/0000-0001-8472-1996
Abigail Polin https://orcid.org/0000-0002-1633-6495
Thomas A. Prince https://orcid.org/0000-0002-8850-3627
Eliot Quataert https://orcid.org/0000-0001-9185-5044
Reed L. Riddle https://orcid.org/0000-0002-0387-370X
Ben Rusholme https://orcid.org/0000-0001-7648-4142
Yashvi Sharma https://orcid.org/0000-0003-4531-1745
David L. Shupe https://orcid.org/0000-0003-4401-0430
Jesper Sollerman https://orcid.org/0000-0003-1546-6615
Leonardo Tartaglia https://orcid.org/0000-0003-3433-1492
Lin Yan https://orcid.org/0000-0003-1710-9339
Yuhan Yao https://orcid.org/0000-0001-6747-8509

References

Abolfathi, B., Aguado, D. S., Aguilar, G., et al. 2018, ApJS, 235, 42
Abraham, R. G., & van Dokkum, P. G. 2014, PASP, 126, 55
Arnett, W. D. 1982, ApJ, 253, 785
Arnett, W. D., Branch, D., & Wheeler, J. C. 1985, Natur, 314, 337
Astropy Collaboration, Robitaille, T. P., Tollerud, E. J., et al. 2013, A&A, 558, A33
Barbary, K., Barclay, T., Biswas, R., et al. 2016, SNCosmo: Python Library for Supernova Cosmology, Astrophysics Source Code Library, ascl:1611.017
Bauer, E. B., Schwab, J., & Bildsten, L. 2017, ApJ, 845, 97
Bell, E. F., McIntosh, D. H., Katz, N., & Weinberg, M. D. 2003, ApJS, 149, 289
Bellm, E. C., Kulkarni, S. R., Barlow, T., et al. 2019b, PASP, 131, 068003
Bellm, E. C., Kulkarni, S. R., Graham, M. J., et al. 2019a, PASP, 131, 018002
Bellm, E. C., & Sesar, B. 2016, pyraf-dbsp: Reduction pipeline for the Palomar Double Beam Spectrograph, Astrophysics Source Code Library, ascl:1602.002
Bertin, E. 2006, in ASP Conf. Ser. 351, Astronomical Data Analysis Software and Systems XV, ed. C. Gabriel et al. (San Francisco, CA: ASP), 112
Bertin, E. 2011, in ASP Conf. Ser. 442, Astronomical Data Analysis Software and Systems XX, ed. I. N. Evans et al. (San Francisco, CA: ASP), 435
Bertin, E., & Arnouts, S. 1996, A&AS, 117, 393
Bertin, E., Mellier, Y., Radovich, M., et al. 2002, in ASP Conf. Ser. 281, Astronomical Data Analysis Software and Systems XI, ed. D. A. Bohlender, D. Durand, & T. H. Handley (San Francisco, CA: ASP), 228
Bildsten, L., Shen, K. J., Weinberg, N. N., & Nelemans, G. 2007, ApJL, 662, L95
Blagorodnova, N., Neill, J. D., Walters, R., et al. 2018, PASP, 130, 035003
Blondin, S., & Tonry, J. L. 2007, ApJ, 666, 1024
Bloom, J. S., Kulkarni, S. R., & Djorgovski, S. G. 2002, AJ, 123, 1111
Bobrick, A., Davies, M. B., & Church, R. P. 2017, MNRAS, 467, 3556
Brooks, J., Bildsten, L., Marchant, P., & Paxton, B. 2015, ApJ, 807, 74
Brown, W. R., Kilic, M., Kenyon, S. J., & Gianninas, A. 2016, ApJ, 824, 46
Burke, J., Arcavi, I., Hiramatsu, D., et al. 2019, TNSCR, 2019-1232, 1
Cano, Z. 2013, MNRAS, 434, 1098
Cao, Y., Kasliwal, M. M., Arcavi, I., et al. 2013, ApJL, 775, L7
Cardelli, J. A., Clayton, G. C., & Mathis, J. S. 1989, ApJ, 345, 245
Carter, P. J., Marsh, T. R., Steeghs, D., et al. 2013, MNRAS, 429, 2143
Chambers, K. C., Huber, M. E., Flewelling, H., et al. 2018, TNSTR, 2018-2068, 1
Chambers, K. C., Magnier, E. A., Metcalfe, N., et al. 2016, arXiv:1612.05560
Chen, P., Dong, S., Stritzinger, M. D., et al. 2020, ApJL, 889, L6
Clayton, G. C. 1996, PASP, 108, 225
Cook, D. O., Kasliwal, M. M., Van Sistine, A., et al. 2019, ApJ, 880, 7
Crts, N. M. W. 2018, TNSTR, 2018-804, 1
Dálya, G., Galgóczi, G., Dobos, L., et al. 2018, MNRAS, 479, 2374
De, K. 2019a, TNSTR, 2019-2208, 1
De, K. 2019b, TNSTR, 2019-2307, 1
De, K., Hankins, M. J., Kasliwal, M. M., et al. 2020, PASP, 132, 025001
De, K., Kasliwal, M. M., Cantwell, T., et al. 2018a, ApJ, 866, 72
De, K., Kasliwal, M. M., Ofek, E. O., et al. 2018b, Sci, 362, 201
De, K., Kasliwal, M. M., Polin, A., et al. 2019b, ApJL, 873, L18
De, K., Tzanidakis, A., Kasliwal, M. M., Fremling, C., & Kulkarni, S. R. 2019a, ATel, 13262, 1
Dekany, R., Smith, R. M., Belicki, J., et al. 2016, Proc. SPIE, 9908, 99085M
DESI Collaboration, Aghamousa, A., Aguilar, J., et al. 2016, arXiv:1611.00036
Dessart, L., & Hillier, D. J. 2015, MNRAS, 447, 1370
Dessart, L., Hillier, D. J., Li, C., & Woosley, S. 2012, MNRAS, 424, 2139
Dey, A., Schlegel, D. J., Lang, D., et al. 2019, AJ, 157, 168
Dimitriadis, G., Siebert, M. R., Kilpatrick, C. D., et al. 2019, TNSCR, 2019-675, 1
Drake, A. J., Djorgovski, S. G., Mahabal, A., et al. 2009, ApJ, 696, 870
Drout, M. R., Soderberg, A. M., Gal-Yam, A., et al. 2011, ApJ, 741, 97
D'Souza, R., Kauffman, G., Wang, J., & Vegetti, S. 2014, MNRAS, 443, 1433
Duev, D. A., Mahabal, A., Masci, F. J., et al. 2019, MNRAS, 489, 3582
Feindt, U., Nordin, J., Rigault, M., et al. 2019, JCAP, 2019, 005
Filippenko, A. V. 1997, ARA&A, 35, 309
Filippenko, A. V., Chornock, R., Swift, B., et al. 2003, IAUC, 8159
Filippenko, A. V., Richmond, M. W., Branch, D., et al. 1992, AJ, 104, 1543
Fink, M., Röpke, F. K., Hillebrandt, W., et al. 2010, A&A, 514, A53

Flörs, A., Spyromilio, J., Taubenberger, S., et al. 2020, MNRAS, 491, 2902
Foley, R. J. 2015, MNRAS, 452, 2463
Foley, R. J., Chornock, R., Filippenko, A. V., et al. 2009, AJ, 138, 376
Foley, R. J., Jha, S. W., Pan, Y.-C., et al. 2016, MNRAS, 461, 433
Fransson, C., & Chevalier, R. A. 1989, ApJ, 343, 323
Fremling, C., Sollerman, J., Kasliwal, M. M., et al. 2018, A&A, 618, A37
Fremling, C., Sollerman, J., Taddia, F., et al. 2016, A&A, 593, A68
Fremling, U. C., Miller, A. A., Sharma, Y., et al. 2019, arXiv:1910.12973
Frohmaier, C., Sullivan, M., Maguire, K., & Nugent, P. 2018, ApJ, 858, 50
Frohmaier, C., Sullivan, M., Nugent, P. E., et al. 2019, MNRAS, 486, 2308
Frohmaier, C., Sullivan, M., Nugent, P. E., Goldstein, D. A., & DeRose, J. 2017, ApJS, 230, 4
Fryer, C. L., Ruiter, A. J., Belczynski, K., et al. 2010, ApJ, 725, 296
Gaia Collaboration, Brown, A. G. A., Vallenari, A., et al. 2018, A&A, 616, A1
Galbany, L., Ashall, C., Höflich, P., et al. 2019, A&A, 630, A76
Gal-Yam, A. 2017, in Handbook of Supernovae, ed. A. Alsabti & P. Murdin (Cham: Springer), 1
Gal-Yam, A., Arcavi, I., Ofek, E. O., et al. 2014, Natur, 509, 471
Geier, S., Marsh, T. R., Wang, B., et al. 2013, A&A, 554, A54
Graham, M. J., Kulkarni, S. R., Bellm, E. C., et al. 2019, PASP, 131, 078001
Grzegorzek, J. 2019, TNSTR, 2019-666, 1
Guillochon, J., Parrent, J., Kelley, L. Z., & Margutti, R. 2017, ApJ, 835, 64
Hachinger, S., Mazzali, P. A., Taubenberger, S., et al. 2012, MNRAS, 422, 70
Harris, W. E. 1996, AJ, 112, 1487
Hinshaw, G., Larson, D., Komatsu, E., et al. 2013, ApJS, 208, 19
Hoeflich, P., & Khokhlov, A. 1996, ApJ, 457, 500
Hogg, D. W., Pahre, M. A., McCarthy, J. K., et al. 1997, MNRAS, 288, 404
Holcomb, C., Guillochon, J., De Colle, F., & Ramirez-Ruiz, E. 2013, ApJ, 771, 14
Howell, D. A. 2001, ApJL, 554, L193
Howell, D. A., Sullivan, M., Perrett, K., et al. 2005, ApJ, 634, 1190
Hunter, J. D. 2007, CSE, 9, 90
Iben, I, Jr., & Tutukov, A. V. 1989, ApJ, 342, 430
Inserra, C., Sim, S. A., Wyrzykowski, L., et al. 2015, ApJL, 799, L2
Jacobson-Galán, W. V., Polin, A., Foley, R. J., et al. 2020, ApJ, 896, 165
Jerkstrand, A. 2017, in Handbook of Supernovae, ed. A. W. Alsabti & P. Murdin (Cham: Springer), 795
Jiang, J.-A., Doi, M., Maeda, K., et al. 2017, Natur, 550, 80
Kasliwal, M. M., Cannella, C., Bagdasaryan, A., et al. 2019, PASP, 131, 038003
Kasliwal, M. M., Kulkarni, S. R., Gal-Yam, A., et al. 2010, ApJL, 723, L98
Kasliwal, M. M., Kulkarni, S. R., & Gal-Yam, A. 2012, ApJ, 755, 161
Kawabata, K. S., Maeda, K., Nomoto, K., et al. 2010, Natur, 465, 326
Kawana, K., Maeda, K., Yoshida, N., & Tanikawa, A. 2020, ApJL, 890, L26
Khatami, D. K., & Kasen, D. N. 2019, ApJ, 878, 56
Kochanek, C. S., Pahre, M. A., Falco, E. E., et al. 2001, ApJ, 560, 566
Kollmeier, J. A., Zasowski, G., Rix, H.-W., et al. 2017, arXiv:1711.03234
Kromer, M., Sim, S. A., Fink, M., et al. 2010, ApJ, 719, 1067
Kulkarni, S. R., Perley, D. A., & Miller, A. A. 2018, ApJ, 860, 22
Kupfer, T., van Roestel, J., Brooks, J., et al. 2017, ApJ, 835, 131
Lang, D., Hogg, D. W., & Schlegel, D. J. 2016, AJ, 151, 36
Leadbeater, R. 2018, TNSCR, 2018-1486, 1
Li, W., Filippenko, A. V., Chornock, R., et al. 2003, PASP, 115, 453
Li, W., Leaman, J., Chornock, R., et al. 2011, MNRAS, 412, 1441
Liu, Y.-Q., Modjaz, M., Bianco, F. B., & Graur, O. 2016, ApJ, 827, 90
Livne, E., & Arnett, D. 1995, ApJ, 452, 62
Livne, E., & Glasner, A. S. 1990, ApJ, 361, 244
Livne, E., & Glasner, A. S. 1991, ApJ, 370, 272
Lucy, L. B. 1991, ApJ, 383, 308
Lunnan, R., Kasliwal, M. M., Cao, Y., et al. 2017, ApJ, 836, 60
Lyman, J. D., Levan, A. J., Church, R. P., Davies, M. B., & Tanvir, N. R. 2014, MNRAS, 444, 2157
Lyman, J. D., Levan, A. J., James, P. A., et al. 2016, MNRAS, 458, 1768
MacLeod, M., Goldstein, J., Ramirez-Ruiz, E., Guillochon, J., & Samsing, J. 2014, ApJ, 794, 9
MacLeod, M., Guillochon, J., Ramirez-Ruiz, E., Kasen, D., & Rosswog, S. 2016, ApJ, 819, 3
Mahabal, A., Rebbapragada, U., Walters, R., et al. 2019, PASP, 131, 038002
Mannucci, F., Maoz, D., Sharon, K., et al. 2008, MNRAS, 383, 1121
Margalit, B., & Metzger, B. D. 2016, MNRAS, 461, 1154
Marinacci, F., Vogelsberger, M., Pakmor, R., et al. 2018, MNRAS, 480, 5113
Marion, G. H., Vinko, J., Kirshner, R. P., et al. 2014, ApJ, 781, 69
Masci, F. J., Laher, R. R., Rusholme, B., et al. 2019, PASP, 131, 018003
McBrien, O. R., Smartt, S. J., Chen, T.-W., et al. 2019, ApJL, 885, L23

McKinney, W. 2010, in Proc. 9th Python in Science Conf., ed. S. van der Walt & J. Millman, 51, http://conference.scipy.org/proceedings/scipy2010/mckinney.html
Meng, X., & Han, Z. 2015, A&A, 573, A57
Mernier, F., de Plaa, J., Pinto, C., et al. 2016, A&A, 595, A126
Metzger, B. D. 2012, MNRAS, 419, 827
Milisavljevic, D., Patnaude, D. J., Raymond, J. C., et al. 2017, ApJ, 846, 50
Moore, K., Townsley, D. M., & Bildsten, L. 2013, ApJ, 776, 97
Moriya, T. J., Mazzali, P. A., Tominaga, N., et al. 2017, MNRAS, 466, 2085
Mulchaey, J. S., Kasliwal, M. M., & Kollmeier, J. A. 2014, ApJL, 780, L34
Naiman, J. P., Pillepich, A., Springel, V., et al. 2018, MNRAS, 477, 1206
Neill, J. D., Sullivan, M., Howell, D. A., et al. 2009, ApJ, 707, 1449
Nelemans, G., Yungelson, L. R., & Portegies Zwart, S. F. 2004, MNRAS, 349, 181
Nelson, D., Springel, V., Pillepich, A., et al. 2019, ComAC, 6, 2
Nomoto, K. 1980, SSRv, 27, 563
Nomoto, K. 1982a, ApJ, 253, 798
Nomoto, K. 1982b, ApJ, 257, 780
Nordin, J., Brinnel, V., Giomi, M., et al. 2019a, TNSTR, 2019-1594, 1
Nordin, J., Brinnel, V., van Santen, J., et al. 2019b, A&A, 631, A147
Nugent, P., Baron, E., Branch, D., Fisher, A., & Hauschildt, P. H. 1997, ApJ, 485, 812
Nugent, P. E., Sullivan, M., Cenko, S. B., et al. 2011, Natur, 480, 344
Oke, J. B., Cohen, J. G., Carr, M., et al. 1995, PASP, 107, 375
Oke, J. B., & Gunn, J. E. 1982, PASP, 94, 586
Pakmor, R., Kromer, M., Taubenberger, S., & Springel, V. 2013, ApJL, 770, L8
Patterson, M. T., Bellm, E. C., Rusholme, B., et al. 2019, PASP, 131, 018001
Perets, H. B. 2014, arXiv:1407.2254
Perets, H. B., Gal-yam, A., Crockett, R. M., et al. 2011, ApJL, 728, L36
Perets, H. B., Gal-Yam, A., Mazzali, P. A., et al. 2010, Natur, 465, 322
Perley, D. A. 2019, PASP, 131, 084503
Pfahl, E., Scannapieco, E., & Bildsten, L. 2009, ApJL, 695, L111
Phillips, M. M. 1993, ApJL, 413, L105
Phillips, M. M., Li, W., Frieman, J. A., et al. 2007, PASP, 119, 360
Piro, A. L., & Nakar, E. 2014, ApJ, 784, 85
Polin, A., Nugent, P., & Kasen, D. 2019a, ApJ, 873, 84
Polin, A., Nugent, P., & Kasen, D. 2019b, arXiv:1910.12434
Prentice, S. J., Maguire, K., Flörs, A., et al. 2020, A&A, 635, A186
Rigault, M., Neill, J. D., Blagorodnova, N., et al. 2019, A&A, 627, A115
Roelofs, G. H. A., Nelemans, G., & Groot, P. J. 2007, MNRAS, 382, 685
Rosswog, S., Ramirez-Ruiz, E., & Hix, W. R. 2008, ApJ, 679, 1385
Samsing, J., MacLeod, M., & Ramirez-Ruiz, E. 2017, ApJ, 846, 36
Schlafly, E. F., & Finkbeiner, D. P. 2011, ApJ, 737, 103
Schwab, J. 2019, ApJ, 885, 27
Sell, P. H., Arur, K., Maccarone, T. J., et al. 2018, MNRAS, 475, L111
Sell, P. H., Maccarone, T. J., Kotak, R., Knigge, C., & Sand, D. J. 2015, MNRAS, 450, 4198
Shen, K. J., & Bildsten, L. 2009, ApJ, 699, 1365
Shen, K. J., Kasen, D., Weinberg, N. N., Bildsten, L., & Scannapieco, E. 2010, ApJ, 715, 767
Shen, K. J., & Moore, K. 2014, ApJ, 797, 46
Shen, K. J., Quataert, E., & Pakmor, R. 2019, ApJ, 887, 180
Silverman, J. M., Foley, R. J., Filippenko, A. V., et al. 2012, MNRAS, 425, 1789
Silverman, J. M., Mazzali, P., Chornock, R., et al. 2009, PASP, 121, 689
Sim, S. A., Fink, M., Kromer, M., et al. 2012, MNRAS, 420, 3003
Sim, S. A., Röpke, F. K., Hillebrandt, W., et al. 2010, ApJL, 714, L52
Srivastav, S., Smartt, S. J., Leloudas, G., et al. 2020, ApJL, 892, L24
Sullivan, M., Kasliwal, M. M., Nugent, P. E., et al. 2011, ApJ, 732, 118
Sullivan, M., Le Borgne, D., Pritchet, C. J., et al. 2006, ApJ, 648, 868
Sun, F., & Gal-Yam, A. 2017, arXiv:1707.02543
Tachibana, Y., & Miller, A. A. 2018, PASP, 130, 128001
Taddia, F., Stritzinger, M. D., Bersten, M., et al. 2018, A&A, 609, A136
Taubenberger, S. 2017, in Handbook of Supernovae, ed. A. W. Alsabti & P. Murdin (Cham: Springer), 317
Tauris, T. M., Langer, N., & Podsiadlowski, P. 2015, MNRAS, 451, 2123
Tomasella, L., Stritzinger, M., Benetti, S., et al. 2020, MNRAS, 496, 1132
Tonry, J., Denneau, L., Heinze, A., et al. 2019a, TNSTR, 2019-1035, 1
Tonry, J., Denneau, L., Heinze, A., et al. 2019b, TNSTR, 2019-1787, 1
Tonry, J. L., Denneau, L., Heinze, A. N., et al. 2018, PASP, 130, 064505
Toonen, S., Perets, H. B., Igoshev, A. P., Michaely, E., & Zenati, Y. 2018, A&A, 619, A53
Townsley, D. M., Moore, K., & Bildsten, L. 2012, ApJ, 755, 4
Valenti, S., Yuan, F., Taubenberger, S., et al. 2014, MNRAS, 437, 1519

van Dokkum, P., Abraham, R., Brodie, J., et al. 2016, ApJL, 828, L6
van Dokkum, P., Abraham, R., Romanowsky, A. J., et al. 2017, ApJL, 844, L11
van Dokkum, P., Cohen, Y., Danieli, S., et al. 2018, ApJL, 856, L30
Virtanen, P., Gommers, R., Oliphant, T. E., et al. 2020, NatMe, 17, 261
Waldman, R., Sauer, D., Livne, E., et al. 2011, ApJ, 738, 21
Wiggins, P. 2018, TNSTR, 2018-1459, 1
Woosley, S. E. 2019, ApJ, 878, 49

Woosley, S. E., & Kasen, D. 2011, ApJ, 734, 38
Woosley, S. E., Taam, R. E., & Weaver, T. A. 1986, ApJ, 301, 601
Woosley, S. E., & Weaver, T. A. 1994, ApJ, 423, 371
Yao, Y., Miller, A. A., Kulkarni, S. R., et al. 2019, ApJ, 886, 152
Yaron, O., & Gal-Yam, A. 2012, PASP, 124, 668
Yuan, F., Kobayashi, C., Schmidt, B. P., et al. 2013, MNRAS, 432, 1680
Zackay, B., Ofek, E. O., & Gal-Yam, A. 2016, ApJ, 830, 27
Zenati, Y., Perets, H. B., & Toonen, S. 2019, MNRAS, 486, 1805